

Growth and Magnetism of 2D Bimetallic Nanostructures

THÈSE N° 4231 (2008)

PRÉSENTÉE LE 5 DÉCEMBRE 2008
À LA FACULTÉ SCIENCES DE BASE
LABORATOIRE DE NANOSTRUCTURES SUPERFICIELLES
PROGRAMME DOCTORAL EN PHYSIQUE

ÉCOLE POLYTECHNIQUE FÉDÉRALE DE LAUSANNE

POUR L'OBTENTION DU GRADE DE DOCTEUR ÈS SCIENCES

PAR

Géraud MOULAS

acceptée sur proposition du jury:

acceptée sur proposition du jury :
Prof. G. Meylan, président du jury
Prof. H. Brune, directeur de thèse
Prof. M. Gijs, rapporteur
Prof. T. Greber, rapporteur
Dr S. Rousset, rapporteur



ÉCOLE POLYTECHNIQUE
FÉDÉRALE DE LAUSANNE

Suisse
2008

Abstract

This thesis addresses the growth and magnetic characterization of 2D bimetallic nanostructures deposited by atomic beam epitaxy (ABE) on Pt(111). These structures possess both tunable high perpendicular magnetic anisotropy (PMA) and magnetic moment. These properties make them appealing as model systems in order to learn how to control the properties of the futures media used in magnetic data storage. Our study combined two *in situ* measurements techniques : variable-temperature scanning tunneling microscopy (VT-STM) as a local probe allows insight on the morphology of nanostructures, while magneto-optic Kerr effect (MOKE) is a spatially integrating technique giving access to the variation of the overall magnetization of a sample.

The first part of this work focuses on the growth of iron on the Pt(111) surface. Growth was investigated on the atomic scale as a function of the substrate temperature in the case of low coverages. We have fitted the mean cluster size as a function of the annealing temperature with mean field rate equations for diffusion-controlled growth. The activation parameters for monomer, dimer and trimer diffusion could be inferred from this procedure. The formation of monatomic Fe wires has also been evidenced on the temperature range 160 K–260 K. The origin of their formation was discussed.

In a second part, we have made use of our knowledge on the growth of cobalt and iron on Pt(111) in order to fabricate "core-shell" Co nanostructures of which density, size and shape were controlled. Therefore, we could realized both compact and ramified structures within the size range 800 – 1800 atoms. The study of the mechanism of magnetization reversal of these model structures has revealed a strong size and shape dependence. This is due to the shape-induced non-uniformity of the local magnetization and the number of pinning centers. The conclusions are that ramified structures with arms longer than 150 Å reverse their magnetization by nucleation and domain-wall motion while compact structures reverse coherently their magnetization.

The third part deals with the magnetic properties of one monolayer thick bimetallic "Co core-shell" nanostructures on Pt(111). The blocking temperature T_B marks the transition between superparamagnetic and blocked states and is inferred from the magnetic anisotropy. Here, we performed magnetic zero-field susceptibility measurements so as to determine T_B in our samples. From our experiments, we show

the possibility to make up a fine tuning of the nanostructure magnetic anisotropy and overall magnetization. In the case of the $\text{Fe}_x\text{Co}_{1-x}$ alloy, T_B adopt a bell-shape with x and exhibit a maximum at $x = 0.5$. The various lateral and vertical interfaces between Co from one side and Fe, Pt or Pd from the other side are at the origin of substantial T_B variation. Those variations are inferred from the symmetry breaking and the strong hybridization between the d orbitals of these elements.

Key words : Scanning Tunneling Microscopy (STM), Magneto-Optic Kerr Effect (MOKE), epitaxial growth, magnetic susceptibility, nanowires, magnetization reversal, perpendicular magnetic anisotropy (PMA), cobalt, iron, Pt(111).

Version abrégée

Cette thèse porte sur la réalisation et la caractérisation magnétique de nanostructures bidimensionnelles bimétalliques déposées par épitaxie par jet atomique sur une surface de Pt(111). Ces structures présentent à la fois une forte anisotropie magnétique hors-plan et un haut moment magnétique dont leur valeur peut être ajustée. Ces propriétés en font des systèmes modèles pour apprendre à contrôler les propriétés des futures media utilisés dans le stockage magnétique d'information. Notre étude a été menée en utilisant conjointement et *in situ* l'information locale apportée par la microscopie à effet tunnel variable en température et les mesures magnétiques déterminées par effet Kerr magnéto-optique.

La première partie de ce travail est consacrée à la croissance du fer sur Pt(111). L'étude a été réalisée à l'échelle atomique en fonction de la température pour de faibles recouvrements. Nous avons comparé un modèle de diffusion atomique sous forme d'équations de taux à l'évolution de la taille moyenne des agrégats de fer avec la température de recuit. Cela nous permet de dégager les principaux paramètres de la diffusion de monomère, dimère et trimère. La formation de nanofils de fer de largeur monoatomique a également été mise en évidence sur une plage de température d'environ 100 K. L'origine de leur formation a été discutée.

Dans une deuxième partie, nous avons utilisé nos connaissances sur la diffusion du Co et du Fe sur le Pt(111) afin de concevoir des nanostructures bidimensionnelles de type "cœur-enveloppe" dont la densité, la taille et la forme ont pu être contrôlées. Ainsi, il a été possible de réaliser aussi bien des structures compactes que ramifiées pour des tailles variant entre 800 atomes et 1800 atomes. Le mécanisme de renversement d'aimantation de ces structures modèles a alors été étudié. Nous avons pu observer une grande dépendance du mécanisme de renversement d'aimantation avec la forme et la taille des îlots. Ceci s'explique car la forme des îlots influence l'homogénéité de l'aimantation locale et le nombre de centres de piégeage magnétiques. Ainsi, des îlots ramifiés possédant des bras plus long que 150 Å semblent renverser leur aimantation par nucléation et déplacement de parois. De même, les îlots plus compacts renversent leur aimantation de façon cohérente sur tout l'îlot.

Finalement, nous avons étudié les propriétés magnétiques d'îlots bimétalliques bidimensionnelles de type "cœur de Co-enveloppe" sur une surface de Pt(111). La température de blocage T_B représente la température de transition entre l'état d'ai-

mantation bloquée et l'état superparamagnétique. Elle est directement reliée à l'anisotropie magnétique. Ici, nous utilisons des mesures de susceptibilité magnétique en champ nul afin de déterminer T_B dans chacun de nos échantillons. À partir de ces mesures, nous montrons qu'il est possible de réaliser un réglage minutieux de l'anisotropie magnétique et de l'aimantation des nanostructures. Dans le cas de l'alliage $\text{Fe}_x\text{Co}_{1-x}$, T_B varie en forme de cloche avec x et présente un maximum à $x = 0.5$. Les diverses interfaces latérales et verticales entre le cobalt d'une part et le fer, le platine et le palladium d'autre part sont à l'origine de profonds changements de T_B . Ces changements sont imputés à la brisure de symétrie et à l'hybridation entre les orbitales d de ces éléments.

Mots clés : Microscopie à effet tunnel (STM), effet Kerr magnéto-optique (MOKE), croissance épitaxiale, susceptibilité magnétique, nanofils, retournement d'aimantation, anisotropie magnétique perpendiculaire (PMA), cobalt, fer, Pt(111).

Contents

Abstract	i
Version Abrégée	iii
Introduction	1
1 VT-STM and MOKE : two complementary methods	7
1.1 Variable Temperature Scanning Tunneling Microscopy	7
1.1.1 Principles	7
1.1.2 STM experimental setup	11
1.2 MOKE	13
1.2.1 Principles	13
1.2.2 Kerr experimental setup	16
1.3 Sample preparation	18
2 Nucleation and growth of Fe on Pt(111)	21
2.1 Introduction to the theory of nucleation	22
2.1.1 State of the art	22
2.1.2 Deducing the energy barriers from experiments	26
2.2 From monomer diffusion to spontaneous wire formation	28
2.2.1 Experimental	28
2.2.2 General overview	31
2.3 Low temperature ripening processes	31
2.3.1 55 K to 130 K : cluster diffusion	31
2.3.2 From 130 K to 160 K : Ostwald ripening	37
2.4 Wire formation, from 160 K to 260 K	39
2.4.1 Wire formation	39
2.4.2 Description of the wires	41

2.4.3	The effect of annealing on growth	44
2.4.4	The effect of the coverage	46
2.4.5	Above 260 K : back to Ostwald ripening	50
2.4.6	Towards an explanation of the wire formation	51
2.5	Conclusion	54
3	Mechanisms of magnetization reversal : from coherent rotation to nucleation and domain wall motion	55
3.1	Length scales	55
3.2	Theoretical models of magnetization reversal : coherent rotation vs. nucleation and domain-wall motion	58
3.2.1	Coherent rotation : the macrospin model	58
3.2.2	Nucleation and domain wall motion	60
3.3	Shape-dependent effect on the mechanism of magnetization reversal .	64
3.4	Mechanism of magnetization reversal in Co nanostructures	67
3.5	Discussion	70
3.6	Other mechanisms?	75
3.7	Conclusions and perspectives	79
4	Magnetism of Co-based nanostructures	81
4.1	State of the art	82
4.1.1	Magnetism of CoX (X = Fe, Pt or Pd) bimetallic structures .	82
4.1.2	Growing core-shell nanostructures	86
4.2	Magnetism of FeCo rim around Pt core : the alloy effect	89
4.3	Magnetism of Fe, Co and Pt rim around Co core : the interface effect	92
4.4	Magnetism of CoPd nanostructures	103
4.4.1	Magnetism of Co islands decorated by Pd	103
4.4.2	Pd statistical deposition on Co/Pt(111)	106
4.5	Conclusion and update	112
	Conclusions and perspectives	115
	Bibliography	119
	Acknowledgment	135
	Curriculum Vitae	137

Introduction

”The principles of physics, as far as I can see, do not speak against the possibility of maneuvering things atom by atom.” (Richard P. Feynman, *”There’s plenty of room at the bottom”*, 29th of December, 1959, Caltech)

Fifty years ago, Feynman anticipated what should be the basis of Nanotechnology [1]. Nowadays, the applications of Nanoscience in everyday life are legion. Printing, catalysis, medicine, telecommunication, glass coating, data storage... These are just few examples of the numerous technological areas where the characteristic lengths have already reached the nanoscale.

Six years after Feynman’s statement, Gordon Moore predicted the popularly known Moore’s Law, stating that the number of transistors on a chip will double about every two years. The technological trend towards the infinitely small was irreversibly launched. Moore’s law did not wait long before to be extended to the industry of data storage. IBM was the first company to introduce a magnetic hard disk drive into a computer already in the late 1950’s : the RAMAC^a project. Nowadays, areal density for hard disk drive storage has increased by more than seven orders of magnitude and is still looking for further improvements.

The challenges brought about by information technology could only be successfully taken up since fundamental science, especially in magnetism, has known a flourishing period of discoveries and improvements.

Breakthroughs in magnetism After the advent of quantum mechanics, magnetism developed to an important inspirational source for physical concepts, methods, phenomena and materials in modern solid state physics. As an example, the Heisenberg model, the Hubbard model, the Kondo effect, the Curie-Weiss law, spin-dependent neutron scattering and spin-polarized photoemission had a deep impact on the field of condensed matter. However, surprisingly, a clear microscopic theory describing a hierarchy of interactions in energy and length scale from ground state properties to spin-dynamics is still missing. Probably for this reason, one could read

^aRAMAC stands for Random Access Method of Accounting and Control. The IBM 305 RAMAC had a data storage capacity of about 20 Mb.

in the 15th edition of the Encyclopaedia Britannica in 1989,

“Few subjects in science are more difficult to understand than magnetism”.

One year before, the 2007 Nobel laureates in Physics Albert Fert (Paris) and Peter Grünberg (Juelich) seeded the entire new research area *spintronics* with their discovery of the giant magnetoresistance (GMR). Other discoveries, developments and innovations with great intellectual and societal impact have been made during the following 20 years. Among these are, for example, the discovery of the x-ray magnetic dichroism (XMD), the synthesis of new material classes such as ultrathin films, mass-selected clusters deposited on substrates and molecular magnets; the development of microscopy and spectroscopy techniques such as spin-polarized scanning tunneling (SP-STM), x-ray photoemission microscopies (XPS), ferromagnetic resonance (FMR) or magneto-optic Kerr effect applied to surface (MOKE, sometimes referred as SMOKE). Theoreticians have followed the same trend with the refinement of calculation methods, relevant in the case of reduced dimensions, as Quantum Monte Carlo (QMC) or dynamical mean field theories, as well as the introduction of Berry phase concepts into magnetism.

Basic research in the magnetism of thin films and surfaces was also undergone. The two-dimensional limit was hit with the study of a one atomic monolayer (ML) high magnetic material on a nonmagnetic substrate. Thereby, unusual effects were discovered, such as the ferromagnetic order, that some materials might develop in the monolayer regime, whereas they are nonmagnetic in their bulk form. A large part of these discoveries could not have been achieved without the same extraordinary evolution in *surface science*, an other scientific area crowned by the 2007 Nobel Prize in Chemistry granted to Gerhard Ertl^a.

Brief History of surface science Surface science is a burgeoning research field. This is mainly due to the novel and fascinating properties that occur when reducing the dimensions of a material. On the one hand, materials with reduced size are strongly dominated by surface phenomena, which can lead to sudden changes in properties compared to what they exhibit on a macroscale. On the other hand, at the atomic scale, classic physics do not stand and only quantum physics is able to describe precisely the origin of the new physical properties.

From a historical point of view, the main breakthrough in surface science came with the creation of the Scanning Tunneling Microscopy (STM) by Gerd K. Binnig and Heinrich Rohrer in 1981^b in Zurich. But a bunch of existing or newly created experimental techniques are now used in order to characterize the electronic, structural, magnetic or chemical properties on surface. Field Ion Microscopy (FIM), Atomic Force Microscopy (AFM), Auger Electron Spectroscopy (AES), Low Energy Electron

^aGerhard Ertl recieved the Nobel Prize for his advancements in surface chemistry, specifically his investigation of the interaction between carbon monoxide molecules and platinum surfaces

^bThe two physicians have been awarded the Nobel Prize in 1986 for their invention.

Diffraction (LEED) are just few examples of the several techniques that contributed to the success of surface science.

Molecular/Atomic Beam Epitaxy (MBE or more recently ABE) is a growth technique that allows surface deposition of only few atoms per second. This technique has caught more attention in the last decades. Following the three primary thin film growth processes ^a, nucleation theories marked an important step in surface science demonstrating how much arrangement of atoms, clusters and islands on an atomic-scale are governed by kinetics. Now, Kinetic Monte Carlo (KMC) and/or Molecular Dynamics (MD) simulations are generally in excellent agreement with the experiments. As it is a permanent goal of microtechnology to produce denser and smaller clusters, surface nanopatterning (also known as "bottom up" approach) has become an important issue in actual research [2–5].

Current progress and remaining challenges in the magnetism of nanostructures Both from a fundamental and technological point of view, understanding magnetism on the atomic-scale appears to be the logic next step to move on to. But this goal can only be reached with an atomic scale control of the morphology of magnetic materials. One possibility to nano-engineer suitable magnetic structures is the self-assembled growth. In self-assembly, components, either separated or linked, spontaneously form under defined conditions ordered structures. These conditions can be the substrate type, the temperature or the deposition flux. Because self-assembled nanostructures of hundreds to thousands atoms are well defined and controllable on the atomic scale, they are ideally suited to study the fundamentals of magnetism at low dimensions. In all the manuscript, we will refer to nanostructure, particle and island in an indistinct manner.

A study of the magnetic properties of Co islands on Pt(111) has revealed that the lower coordinated atoms play a decisive role on the magnetic properties [6]. However, numerous questions in the field of magnetic nanostructures remain open :

- The mechanism of magnetization reversal is known to be strongly affected by the shape and the size of a nanostructure. But a clear understanding of the phenomenon is still missing.

- It seems that the exact composition of an alloy has an important impact on its magnetic properties in bulk. So what can we expect for bidimensional bimetallic magnetic nanostructures ?

The aim of this work is twofold :

- First, novel kinds of nanostructures have to be realized with a bottom up approach. The key parameters for the structure growth have to be identified and they have to be eventually optimized.

- Secondly, techniques to realize new magnetic nanostructures with well defined magnetic properties have to be presented. Further, the parameters that affect the local

^aThese processes, known as Stranski-Krastanov, Volmer-Weber and Frank-Van der Merwe mechanisms, describe thin film growth from a thermodynamical point of view. Growth is explained via a force balance of surface tensions and contact angle.

magnetic properties, have to be extinguished and their impact has to be assessed.

Therefore we have investigated one monolayer high, bimetallic nanostructures grown on Pt(111) by means of a Scanning Tunneling Microscope. In particular, we will focus on core-shell structures composed of $3d$, $4d$ and $5d$ transition metals. Namely, FeCo, PtCo and PdCo nanostructures will be studied. The choice of the materials and the substrate was motivated by the high magnetic properties already observed and predicted in bulk and thin films. We will study the magnetic properties of different core-shell structures in order to determine the influence of shape and size on the mechanism of magnetization reversal. Furthermore, a serie of experiments on various alloys and interfaces will establish an atomic scale understanding of the contribution of individual constituent atoms to the magnetic properties of the overall island.

Outline of the thesis

The manuscript is organized as follows :

Chapter 1 gives a brief introduction to the main techniques used, i.e., STM and MOKE. Further a theoretical approach based on the Bardeen approximation is described, which provides the required qualitative understanding for the interpretation of STM topographs. A description of the Kerr effect is given and a quantitative expression of the same relative to surface studies is drawn. The sample preparation is eventually described.

Chapter 2 presents a quantitative study of the nucleation and growth of Fe on Pt(111). This study provides the necessary tools in order to fabricate tailored bimetallic nanostructures. A quantitative analysis of the STM topographs was made after a deposition of a small amount of Fe at low temperature, subsequently followed by an annealing. The mean island size as a function of the annealing temperature, in the range of 60 K-350 K, is compared to the results obtained by mean field rate equation theory taking into account tetramer diffusion. Thereof, activation parameters for monomer, dimer and trimer diffusion were deduced. The onset of dissociation was determined with the onset of Ostwald ripening and thus allowed us to infer the dissociation energy.

The formation of monatomic Fe wires was observed in the temperature range of 160 K-260 K. Further, we discuss the mechanisms responsible for their formation. It was found that the presence of Fe nanowires is intrinsically associated with surface strain. A mechanism of wire formation based on long-range interactions between adsorbates is discussed.

Finally, the realisation of a one monolayer thick core-shell structure with controlled size, shape and density is demonstrated.

Chapter 3 is devoted to the experimental determination of the mechanism of magnetization reversal using the model system composed of one monolayer thick Co

core-shell nanostructures. First, we describe the necessary tools to understand the mechanism responsible for magnetization reversal. Then, by means of the growth parameters of Co nucleation on Pt(111) and using the same process as presented in Chapter 2, we have grown Co core-shell nanostructures with well-defined shape, size and density. Two different island shapes, corresponding to ramified and compact islands were studied. An analytical study of the zero-field magnetic susceptibility allowed us to develop a description of the magnetization reversal as a function of the shape and the size of the islands. We found that the characteristic length of an island arm of ramified islands is about 150 Å. The results indicate that above this size, the island magnetization is reversed by nucleation and domain-wall motion. Compact islands show an unequivocal tendency for coherent rotation of the magnetization.

Chapter 4 addresses the origin of the magnetic properties of one monolayer thick bimetallic core-shell nanostructures on Pt(111). Namely, FeCo, PtCo and PdCo alloys were studied. These alloys are expected to present a large perpendicular magnetic anisotropy that is especially well suited for our experimental setup and for the industry of data storage. Different kinds of core-shell structures were fabricated and magnetically characterized through the experimental determination of the blocking temperature T_B , separating the blocked and superparamagnetic states. The main results are that in the case of FeCo alloy, the creation of a sharp lateral interface is responsible for a significant increase of T_B , while alloying the two elements induces a 200% increase of T_B in the case of the equiatomic composition. Our experimental results have been compared to fully relativistic ab initio calculations performed by Sven Bornemann *et al.*^a. The calculations are in excellent agreement with our results. The influence of the lateral and the vertical interface between Co and Pd on the magnetic properties were studied with both the core-shell structures and with a system composed by Co islands, statistically decorated with Pd. The results approve a significant difference in the behavior of the two kinds of interfaces. We attribute this to the different hybridizations between the d orbitals of Co and Pd due to the different structural configurations. Our results demonstrate that we are able to tailor magnetic nanostructures with specific magnetical properties on the atomic scale.

^aS. Bornemann⁺, J. Minár⁺, H. Ebert⁺ and, J. B. Staunton^{*}, ⁺ Department of Physical Chemistry, Ludwig-Maximilians-Universität Munich, Germany and ^{*} Department of Physics, University of Warwick, United Kingdom.

VT-STM and MOKE : two complementary methods

1

This chapter presents Variable Temperature Scanning Tunneling Microscopy (VT-STM) and Magneto-Optic Kerr Effect (MOKE). These two techniques have been employed to conduct the *in situ* characterization of the morphology of the Fe clusters (Chapter 2), Co islands (Chapter 3) and the CoX (X=Fe, Pt, Pd) islands (Chapter 4) as well as their magnetic properties (Chapters 3 and 4).

1.1 Variable Temperature Scanning Tunneling Microscopy

Closely following the concept of the topografiner created by Russell Young in 1971, Scanning tunnelling microscopy was invented by Gerd Binnig and Heinrich Rohrer from the research laboratory of IBM Zurich in 1981 [7, 8]. This technique owes its great popularity to its direct atomic scale imaging and manipulation capabilities coupled to the possibility of extracting information on the electronic structure of surfaces on a local scale. In counterpart, this technique provides only local information of the surface and quantitative analysis requires to know the geometry dependent wave-function in the vicinity of the STM tip. In this chapter, we provide a basic introduction to the physics underlying tunnelling microscopy and a brief description of the microscope employed in the experiments described in this thesis.

1.1.1 Principles

Fig. 1.1 outlines the basic principle of operation of an STM. A sharp metal tip is brought into close proximity ($\sim 5 - 10 \text{ \AA}$) to the conducting surface of a sample. The lateral tip position, x and y , as well as the vertical separation z between the tip and

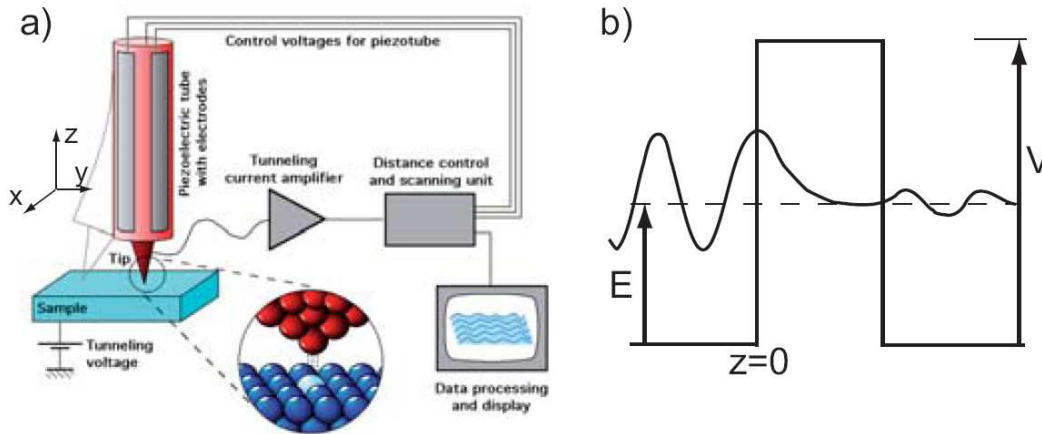


Fig. 1.1 – a) Schematic illustration of the basic principles of a Scanning Tunneling Microscope (STM). The voltages applied to piezoelectric materials allow for a fine horizontal ($V_{x,y}$) and vertical (V_z) positioning of a metallic tip relative to a conductive surface. If the tip is brought close enough to the biased sample (potential V) a tunneling current I is measured (Image from M. Schmid, TU Wien). b) Illustration of the tunneling effect in one dimension.

the surface are controlled with picometer precision by voltage signals applied to piezoelectric transducers. As an overlap between the tip and the sample electron wave function occurs, a bias voltage V applied to the sample (with respect to the ground and the tip) establishes a continuous tunneling current I across the vacuum region separating the two electrodes. The sign of V determines whether tunneling occurs from the tip occupied states to the sample empty states (positive V) or viceversa (Fig. 1.2).

Once the sample and the tip are brought in thermodynamic equilibrium, their Fermi levels equalize. If a voltage V is applied to the sample, its energy levels will be rigidly shifted upward or downward by $\|eV\|$, depending on whether the polarity is negative or positive, respectively. Since states with the highest energy have the longest decay lengths into the vacuum, most of the tunneling current arises from electrons lying near the Fermi level of the negative-biased electrode. The tunnel current I depends exponentially on z , the individual atoms in the surface will give rise to current variations as the tip is scanned across the corrugated surface. In the constant-current mode of operation the current I , which is typically in the 0.3 – 5 nA range, is compared with a preset value I_0 in a feedback loop. The difference between I and I_0 is converted into a correction voltage and sent to the z transducer. In this way the tunneling current is kept constant by approaching or withdrawing the tip from the sample. Recording the feedback signal as a function of the tip position (x,y) over the substrate yields a 3D map of the surface topography. However, $z(x,y)|_{I,V}$ more correctly represents a surface of constant local density of electron states (LDOS) of the sample. Therefore one has to be careful in interpreting it as an image of the position of the atomic nuclei of the surface.

In order to understand the principle of the scanning tunneling microscopy, it is necessary to develop a microscopic theory of the tunneling current in 3D. Two ap-

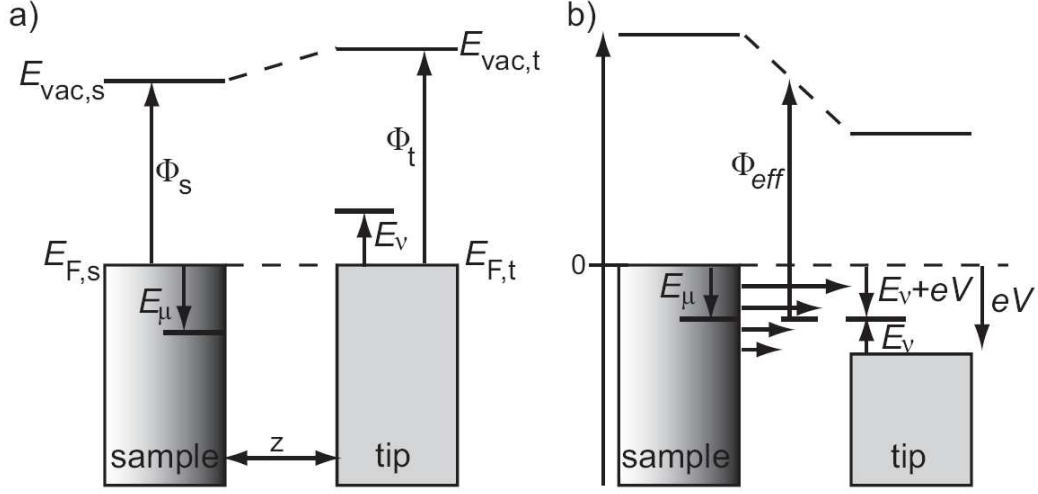


Fig. 1.2 – Energy level diagram of a tunnel junction. a) Without bias voltage applied. b) With an applied voltage V between tip and sample.

proaches are possible. In the scattering method, the Schrödinger equation is solved at the interface tip-sample. The tunneling current is calculated by means of the transmissivity and reflectivity of one electron approaching the tip surface from $+\infty$ and tunneling to the sample. This technique has been implemented by Garcia [9] and Stoll [10]. The second method consists in using the "perturbative-transfer Hamiltonian" formalism introduced by Bardeen and furthermore developed by Tersoff and Hamman [11] and Baratoff [12].

Bardeen considered the case of two parallel plates separated by an insulator [13]. By neglecting the interactions between the two electrodes, the tunnel current can be evaluated from the overlap in the gap region of the wave functions of the sample and the tip, Ψ_μ and Ψ_ν , respectively, considered as separate systems [14] :

$$I(V) = \frac{2\pi e}{\hbar} \sum_{\mu,\nu} |T_{\mu,\nu}|^2 \delta(E_\mu - E_\nu) \times \quad (1.1)$$

$$(f(E_\mu, T)[1 - f(E_\nu + eV, T)] - f(E_\nu + eV, T)[1 - f(E_\mu, T)])$$

where the summation goes over all quantum states μ and ν of the unperturbed sample and tip; the eigenvalues E_μ and E_ν are given with respect to the (common) Fermi level, V is the applied voltage between the electrodes, $f(E, T)$ is the Fermi-Dirac distribution function and T is the temperature. The δ -function indicates that the tunneling electron transfer from one electrode to the other is an elastic process, whereas the Fermi-Dirac functions take into account that tunneling occurs from filled to unfilled states. In the limits of small voltage and temperature, Eq. 1.1 becomes

$$I = \frac{2\pi}{\hbar} e^2 V \sum_{\mu,\nu} |T_{\mu,\nu}|^2 \delta(E_\mu - E_F) \delta(E_\nu - E_F) \quad (1.2)$$

The tunnel matrix element $T_{\mu,\nu}$ represents the overlap in the gap region of the electrode wave functions and is given by the current density operator through a surface S_0 lying entirely within the gap region :

$$T_{\mu,\nu} = -\frac{\hbar^2}{2m_e} \int_{S_0} d\mathbf{S} (\Psi_\nu^* \nabla \Psi_\mu - \Psi_\mu \nabla \Psi_\nu^*) \quad (1.3)$$

The main difficulty in this approach consists in evaluating $T_{\mu,\nu}$. While Bardeen presented his results in 1961 for two planar electrodes, Tersoff and Hamann have proposed specific and more realistic wave functions for calculating the tunnel matrix element. On one hand, the surface wave function Ψ_ν is described by a set of periodic surface plane wave functions decreasing exponentially in the normal direction (z). On the other hand, the tip wave functions are the solutions of the Schrödinger equation for a spherical potential wall (s -wave approximation). Within these approximations and for low bias voltages compared to the electrode work function and low temperature the tunneling current becomes [15] :

$$I(V) \propto \int_0^{eV} dE \rho_t(E - eV) \rho_s(\mathbf{r}_t, E) \quad (1.4)$$

where $\rho_t(E)$ is the density of states associated with the tip atom (i.e., the total density of states for the metal-adatom system minus that for the bare metal) ; $\rho_s(\mathbf{r}, E)$ is the local density of states (LDOS) of the sample and \mathbf{r}_t is the position of the center of the tip. $\rho_s(\mathbf{r}_t, E)$ can be expressed as

$$\rho_s(\mathbf{r}, E) \propto \rho_s(E) \exp(-2z \sqrt{\frac{2m\bar{\Phi}}{\hbar^2}}) \quad (1.5)$$

with the mean barrier height being

$$\bar{\Phi} = \frac{\Phi_t + \Phi_s}{2} + \frac{eV}{2} - E \quad (1.6)$$

and $\rho_s(E)$ being the density of states associated with the sample atom right under the tip.

These approximations lead to two important results : the first is that the tunnel current decays exponentially with increasing distance z between the tip and the sample. This implies that the tip apex atom dominates the tunneling process (for $\bar{\Phi} = 4$ eV, a 1 Å displacement in z implies a ten-fold variation in I), explaining the STM atomic-scale probing capabilities. The second result is that constant-current STM topographs can be simply interpreted as contours of constant $\rho_s(E_F)$ of the surface, since the largest contribution to the integral in Eq. 1.4 comes from the highest-lying energy states of the sample and the tip electronic structure can be considered flat, i.e. ρ_t is taken to be constant. The atomic corrugation imaged by an STM is therefore the modulation of the LDOS surface of the sample. As a consequence, we cannot strictly speaking about "height" and in the following we will refer to apparent height when a description of an STM topograph will occur.

1.1.2 STM experimental setup

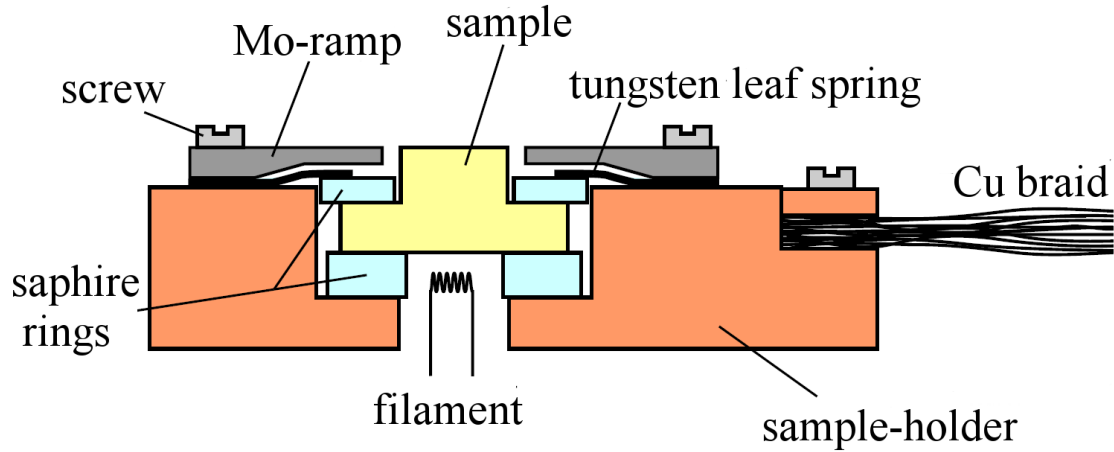


Fig. 1.3 – The sample holder. The temperature control is achieved by simultaneously cooling the sample with liquid helium through the Cu braid, and heating it with the filament under it (from [6]).

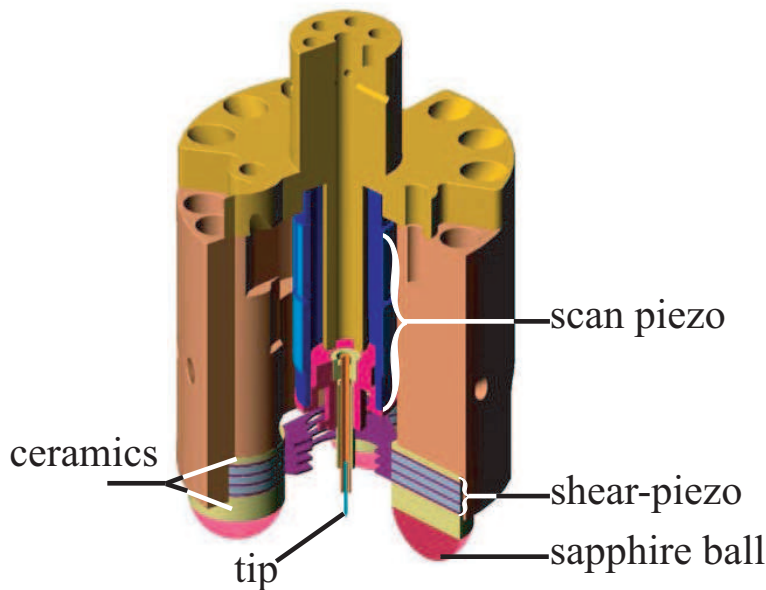


Fig. 1.4 – Vertical cross-section of the home made beetle type STM. The head of the STM is 21 mm wide (diameter) and 35 mm high. (from [6]).

The STM topographs shown in this manuscript have been acquired by means of a Variable-Temperature STM (VT-STM) built at the Institut de Physique des Nanostructures of the EPFL [6, 16–18]. The VT-STM is incorporated into a UHV chamber equipped with standard analysis - Mass Spectrometer (QMS), Auger Spectrometer (AES) - and surface preparation tools - ion sputter gun, variable leak-valves. Several evaporators are mounted : an Omicron triple evaporator, a home built Pt (or Pd)

evaporator and a crucible allowing Cr tip-coating, used for Spin-Polarized experiments. The base pressure in the UHV chamber is kept to $2 - 6 \times 10^{-11}$ mbar by the concerted use of an ion pump, two turbo molecular pumps and a Ti-sublimator.

The sample is hat shaped and can be clamped onto a sample holder leaving its \varnothing 7 mm surface entirely exposed (see Fig. 1.3). Electrical insulation, necessary to apply the bias voltage V , is assured by two thin sapphire rings placed between the sample and the holder. The sample temperature is measured with a NiCr/Ni thermocouple in direct contact with the sample. The sample holder is thermally coupled to the cold finger of a liquid-He flux cryostat. For heating up the sample a filament is mounted closely to the back side of the crystal. The sample can be heated either by radiation or by electron bombardment from the filament. The temperature is controlled with a relative precision of ± 0.01 K and an absolute precision of ± 2 K from 30 K to over 1400 K. The whole manipulator is mounted on a rotatable flange. By turning the manipulator, the sample can be brought in front of all preparation and analysis tools in the chamber. This makes sample transfer unnecessary and permits full temperature control during any phase of an experiment.

During STM (and MOKE) measurements the sample holder is decoupled from the manipulator by lowering the support tube, and rests on a viton-damped copper-stack. For low frequency vibration (≤ 1 Hz) damping the whole UHV chamber is mounted on pneumatic suspension legs. This way, the main source of vibrations is the mechanical connection to the cryostat via the braid. Slight optimization of the overall setup allows one to reach 3 pm peak-to-peak vertical noise during STM topographs. A detailed discussion of the mechanical and electrical noise damping elements is reported in Refs. [6, 17].

The microscope is a home built beetle type STM [19], which is suited to study samples at varying temperatures. A stack of three supporting shear piezos are fixed to a metal head and glued to sapphire balls. The central scan piezo tube is attached to a W tip prepared by electrochemical etching (see Fig. 1.4). This geometry reduces the thermal drift, since thermal contraction and expansion of the scan piezo is, to first approximation, compensated by an equal contraction and expansion of the supporting piezo tubes. Two stages of ceramics surrounding shear-piezos provide a higher thermal isolation between the sample and the head of the STM at room temperature. The STM head is set down on a Mo ring which has three 0.4 mm-high helical ramps all around the sample. The coarse approach of the tip to the sample surface, as well as the lateral displacement, is achieved by inertial motion : asymmetric triangular pulses are applied to the shear-piezos leading to a stick-slip motion over the ramps. Once a tunneling current is detected, the coarse approach is stopped and scanning proceeds via the central piezo.

1.2 MOKE

The first application of the magneto-optic Kerr effect (MOKE) to study surface magnetism took place in 1985 when Bader *et al.* studied magnetism of epitaxial Fe monolayers on Au(100) [20, 21]. Our knowledge of magneto-optic effects is, however, much older. In 1845, Michael Faraday discovered the influence of magnetized media on the transmission of linearly polarized light which leads to an elliptical polarization [22]. A similar effect upon reflection of linearly polarized light was discovered by Reverend John Kerr in 1876 [23]. The present interest in the magneto-optic Kerr effect stems from its use in reading the information on magneto-optic media. This technique, sensitive to the presence of monolayer magnetic structures is also called Surface-MOKE (SMOKE) but it should be kept in mind that MOKE is an integrative technique with a probing depth of the order $100 - 200 \text{ \AA}$.

1.2.1 Principles

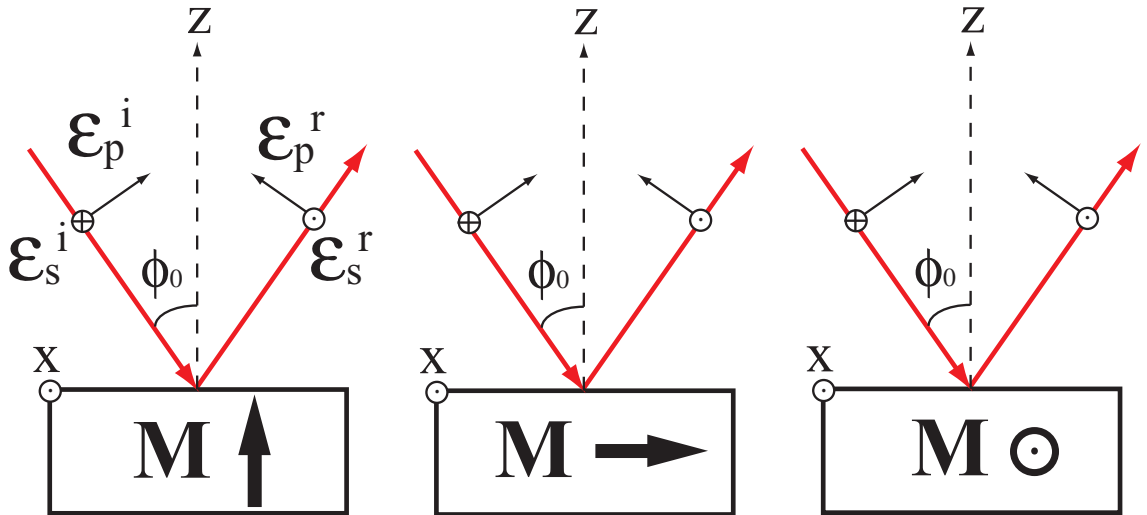


Fig. 1.5 – Typical Kerr configurations : (left) polar, (middle) longitudinal and (right) transverse. A polarized incident light is reflected from a magnetic substrate with an angle ϕ_0 from the surface normal.

Conventionally, both theory and experiment deal with three distinct configurations for the direction of the magnetization \mathbf{M} with respect to the plane of incidence (unit vector $\hat{\mathbf{x}}$ normal to this plane) and plane of separation between layers (unit vector $\hat{\mathbf{z}}$ normal to this plane) : (1) polar $\hat{\mathbf{x}} \perp \mathbf{M} \parallel \hat{\mathbf{z}}$, (2) longitudinal $\hat{\mathbf{x}} \perp \mathbf{M} \perp \hat{\mathbf{z}}$, (3) transverse $\hat{\mathbf{x}} \parallel \mathbf{M} \perp \hat{\mathbf{z}}$ (see Fig. 1.5).

It is also convenient to decompose the incident and reflected light into p- and s- polarized plane waves, for which the polarization is in the plane of incidence or perpendicular to it, respectively.

In the polar and longitudinal configurations, plane-polarized incident light becomes elliptically polarized, having the major axis of polarization rotated with respect

to the original polarization axis. In the transverse configuration, no light is transferred between p and s waves, and the magnetization slightly modifies the amplitudes due to ordinary metallic reflection. In all cases, the magnitudes of the observed effect, i.e., the rotation and ellipticity, or the change in intensity, are proportional to the sample magnetization \mathbf{M} .

Magneto-optic effects arise from the antisymmetric, off-diagonal elements in the dielectric tensor.

$$\epsilon = n^2 \begin{pmatrix} 1 & im_z Q & -im_y Q \\ -im_z Q & 1 & im_x Q \\ im_y Q & -im_x Q & 1 \end{pmatrix} \quad (1.7)$$

where n^2 is independent of the magnetization \mathbf{M} , Q is a magneto-optic coupling strength, also known as the Voigt constant, and $m_i = \mathbf{M}_i/\mathbf{M}$ is the component of the magnetization in direction i ($i = x, y, z$). To the first order, Q is proportional to the magnetization. Moreover, Q is temperature independent but depends on the frequency of the electromagnetic wave. The former property is fundamental to allow determination of magnetic susceptibility vs temperature. Microscopically, a non-zero Kerr effect requires the presence of both spin-orbit (SO) coupling and exchange interactions [24–26].

The total reflectance can be obtained from Maxwell equations assuming plane-waves and conservation of the tangential components of electric and magnetic fields at the interface.

The amplitude of the electric field ε_i of a beam incident from the air and/or vacuum (refractive index $n_{air} \approx n_{vacuum} = 1$) on the surface of a magnetic sample via a polarizer at the angle θ_p of the plane of incidence is given as

$$\varepsilon^i = \varepsilon_0 \cos \theta_p \hat{\mathbf{p}} + \varepsilon_0 \sin \theta_p \hat{\mathbf{s}} \quad (1.8)$$

where $\hat{\mathbf{p}}$ and $\hat{\mathbf{s}}$ are unit vectors. The magnitude of the reflected light can be expressed by the Fresnel matrix \mathfrak{R} as

$$\varepsilon_R = \begin{pmatrix} \varepsilon_p \\ \varepsilon_s \end{pmatrix}^r = \mathfrak{R} \begin{pmatrix} \varepsilon_p \\ \varepsilon_s \end{pmatrix}^i = \begin{pmatrix} r_{pp} & r_{ps} \\ r_{sp} & r_{ss} \end{pmatrix} \begin{pmatrix} \varepsilon_0 \cos \theta_p \\ \varepsilon_0 \sin \theta_p \end{pmatrix} \quad (1.9)$$

where the superscripts r and i indicate reflected and incident light, respectively. The component r_{ps} in \mathfrak{R} couples the s-polarized electric field component of the incident light to the p-polarized electric-field component of the reflected light. In analogy, all r_{ij} with $i, j = p, s$ are defined. The full expression for each component of \mathfrak{R} has been estimated through the ultrathin film limit defined by $\frac{2\pi}{\lambda}|N|d \ll 1$, where λ is the wavelength of the light and d is the thickness of the magnetic layer. In this limit, e.g. magnetic submonolayer nanostructures on Pt(111), where the magnetic overlayer is characterized by N , Q and d , on the non-magnetic substrate with refractive index N_{sub} , the components are [27, 28] :

$$r_{pp} = \frac{\cos \phi_2 - N_{sub} \cos \phi_0}{\cos \phi_2 + N_{sub} \cos \phi_0} + \frac{4\pi idQ \cos \theta_1 (N_{sub}^2 \cos^2 \phi_1 N^2 \cos^2 \phi_2)}{\lambda (\cos \phi_2 + N_{sub} \cos \phi_0)^2} \quad (1.10)$$

$$r_{ss} = \frac{\cos \phi_0 - N_{sub} \cos \phi_2}{\cos \phi_0 + N_{sub} \cos \phi_2} + \frac{4\pi idQ \cos \theta_1 (N^2 \cos^2 \phi_1 N_{sub}^2 \cos^2 \phi_2)}{\lambda (n_1 \cos \phi_0 + N_{sub} \cos \phi_2)^2} \quad (1.11)$$

$$r_{sp} = \frac{4\pi iNdQ \cos \theta_1 (Nm_z \cos \phi_2 + N_{sub} m_y \sin \phi_1)}{\lambda (\cos \phi_0 + N_{sub} \cos \phi_2) (\cos \phi_2 + N_{sub} \cos \phi_0)} \quad (1.12)$$

$$r_{sp} = \frac{4\pi iNdQ \cos \theta_1 (N_{sub} m_y \sin \phi_1 + Nm_z \cos \phi_2)}{\lambda (\cos \phi_0 + N_{sub} \cos \phi_2) (\cos \phi_2 + N_{sub} \cos \phi_0)} \quad (1.13)$$

Here, ϕ_0 , ϕ_1 and ϕ_2 are the incident angles in vacuum, in the ferromagnetic and in the non-magnetic media, respectively. They are calculated by the Snell-Descartes law $N_i \sin \phi_i = N_j \sin \phi_j$ at the boundary between medium i and j . Other reflection coefficients have been derived for bulk [27, 29] as well as multilayer [30–32] configurations.

The Kerr rotation α and the ellipticity η are defined for the s - and p - polarization of the incident wave as :

$$\alpha_s + i\eta_s = \frac{r_{ps}}{r_{ss}} \quad (1.14)$$

$$\alpha_p + i\eta_p = \frac{r_{sp}}{r_{pp}} \quad (1.15)$$

One can see that there is no Kerr rotation ($\alpha + i\eta = 0$) for the case of transverse geometry ($m_y = m_z = 0$, and $m_x = 1$).

The signal received by the detector after the light has passed through an analyzing polarizer set at an angle δ from maximum extinction (unit vector $\hat{\mathbf{a}}$), is

$$I_R = |\varepsilon_R \cdot \hat{\mathbf{a}}|^2 = |\varepsilon_p^r \sin(\theta_p + \delta) + \varepsilon_s^r \cos(\theta_p + \delta)|^2 \quad (1.16)$$

In our case, $\theta_p = 0$ and $\delta \ll 1$, the light is p - polarized before reflexion on the sample and I_R yields

$$I_R = |\varepsilon_0|^2 |r_{pp} \sin \delta + r_{sp} \cos \delta|^2 \approx |\varepsilon_0|^2 |r_{pp} \delta + r_{sp}|^2 \quad (1.17)$$

$$= |\varepsilon_0 r_{pp}|^2 |\delta + \alpha + i\eta|^2 \approx |\varepsilon_0 r_{pp}|^2 (\delta^2 + 2\delta\alpha) \quad (1.18)$$

$$= I_0 \left(1 + \frac{2\alpha}{\delta} \right) \quad (1.19)$$

with $I_0 = |\varepsilon_0 r_{pp}|^2$ being the intensity at zero Kerr rotation. Therefore, a linear relationship is found between I_R and \mathbf{M} for the three geometries, making MOKE a suitable tool for quantitative measurements of magnetization variations.

1.2.2 Kerr experimental setup

	cluster	monolayer is- land	thin film	thick film
Θ (ML ^a)/size (at.)	0.02/< 10	0.2/1000	1/ ^b 1.5×10^{13}	50/ ^b 7.5×10^{14}
Norm. χ_{max}	< 0.1	1	10^{-3}	3×10^{-4}
Relevant energy	Anisotropy		Exchange	

Tab. 1.1 – Typical values for Fe and/or Co on Pt(111). χ_{max} is the maximum value of the zero-field susceptibility normalized to the corresponding value in the case of a monolayer island (see text for details). The estimation takes into account the size-dependence of the total magnetic moment, the anisotropy constant and the Curie temperature [33, 34] and assumes coherent rotation of the cluster and nanostructure magnetization.

Magneto-optic Kerr effect experiments were performed *in situ* in the same UHV chamber used for STM measurements and deposition. The Kerr setup, optimized to have submonolayer sensitivity, is sketched in Fig. 1.6 and comprises a temperature stabilized (± 0.1 K) 780 nm laser diode (5 mW), a collimating optical system, two Glan-Thompson linear polarizers (extinction ratio $\epsilon \approx 10^{-6}$), and a photo-detector. The light passes through the first polarizer, a UHV window (with small birefringence) and then it impinges onto the sample with an incident angle of about 35° with respect to the surface normal. The laser spot diameter on the sample is about 1 mm^2 . The photo-detector, equipped with an optical band-pass filter in order to reduce the effect of variable stray and background light, measures the intensity of the reflected light transmitted through a second UHV window and the second polarizer (analyzer). An electromagnet and a coil inside the UHV chamber produce external magnetic fields at the sample position up to 500 Oe within (transverse Kerr geometry) and perpendicular (polar Kerr geometry) to the film plane. The field sweep and the acquisition of the MOKE signal from the detector are computer controlled. Two operational modes are possible : a) dc-MOKE : the light intensity at the photodiode output is measured as a function of the applied field to generate hysteresis loops or \mathbf{M} versus H curves ; b) ac-MOKE : real and imaginary parts of the complex magnetic susceptibility $\chi(T) = \chi'(T) + i\chi''(T)$ are measured by a lock-in amplifier by comparing respectively, the in-phase and out-of-phase component of the light intensity at the photodiode output to the reference signal applied to the electromagnet or the coil.

The orientation of the first polarizer is set to get *p*-polarized plane wave incident light optimizing the sensibility of polar MOKE. Since the transverse Kerr effect is characterized by a variation of the reflection coefficient relative to this polarization only, it also optimizes the Kerr signal for this configuration. The amplitude of the ac-magnetic field is comprised between 50 and 100 Oe. The modulation frequency is $f = 11$ Hz. This frequency lies between harmonics of the line frequency, is still low

^aML (monolayer) refers to the proportion of adatoms per Pt site.

^bThe size takes into account the laser spot diameter.

^cCritical temperatures are typically the blocking temperature and the Curie temperature. See Chapter 3 for details.

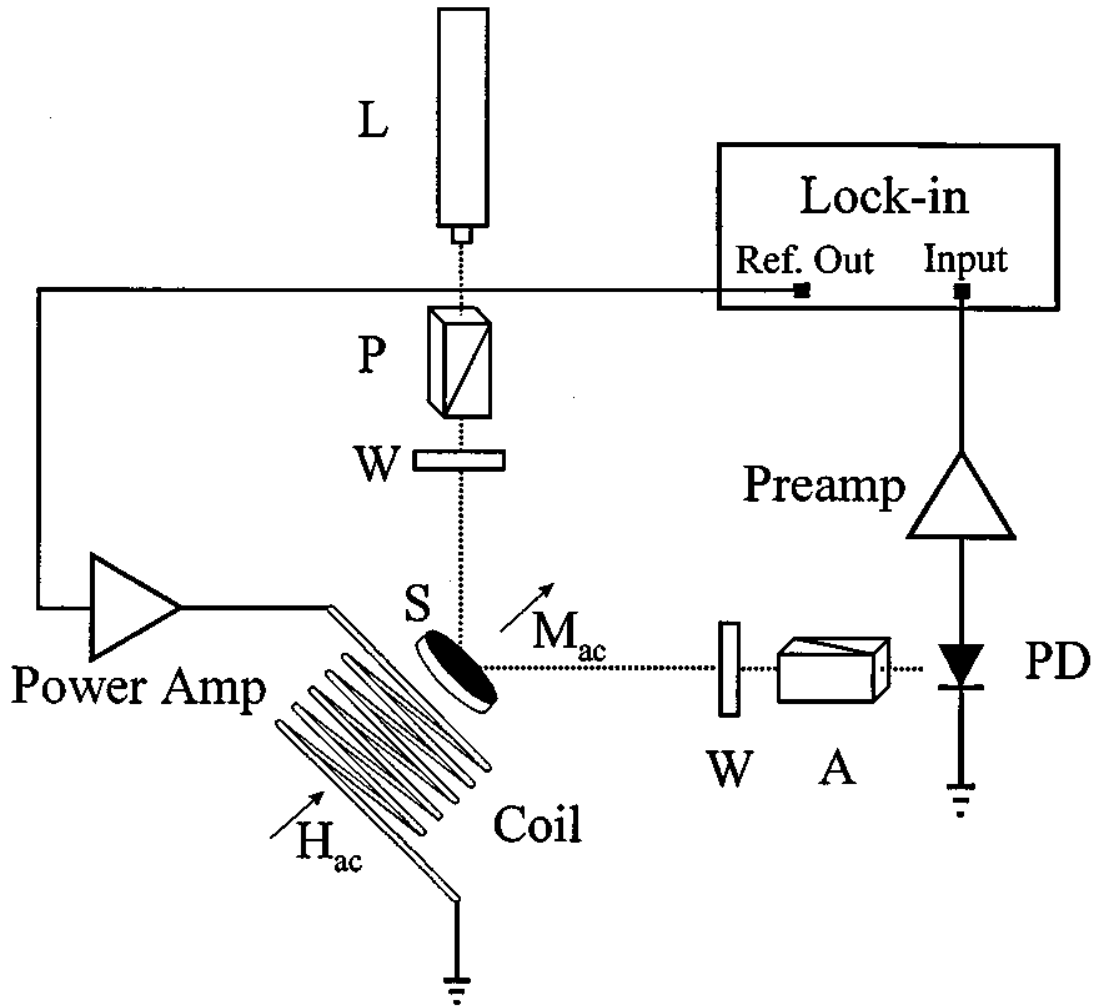


Fig. 1.6 – Light (L) passes through a linear polarizer (P) and UHV window (W) before it falls on the magnetic film sample (S). The magnetization of the film is perturbed by applying an ac field H_{ac} produced by a coreless coil using a current generated from the reference output of a lock-in amplifier. The resulting complex Kerr rotation is detected after the scattered light has passed through a second window, by aligning a second linear polarizer (A) near extinction. The transmitted light intensity falls on a photodiode, and the resulting signal voltage at the reference frequency is detected (from [35]).

enough that the electronics for the photodiode are not bandwidth limited and that measurements are performed in the dynamic scaling region, where frequency does not influence the mechanism of magnetization reversal [36]. Towards low frequencies, the $1/f$ noise limits the resolution, such that 11 Hz is a good compromise. The Kerr signal is measured with the analyzer set to $\delta \approx 1^\circ$ from maximum extinction. The light intensity detected by the photodiode increases with δ but so do two sources of noise : the fluctuations of I_R and δ . The intensity and angular fluctuations are associated with translational and rotational vibrations of the sample as well as drifts in the laser power and are of much higher magnitude than the thermal noise of the

detector [35].

Table 1.1 gives the orders of magnitude of the zero-field magnetic susceptibility $\chi(T)$ for Co and/or Fe on Pt(111) configurations assuming coherent rotation of the magnetization for submonolayer coverage. The value of $\chi(T)$ are inferred from the relevant energy. The magnetism of small structures is driven by the competition between the magnetic anisotropy energy K and the thermal energy. At larger scale, this is exchange energy that is in competition with thermal energy. Therefore, the expression of χ_{max} can be approximated by $\Theta \frac{m^2}{K}$ and $\frac{m^2}{T_C}$ for small and large structures, respectively. Here, m is the magnetic moment of one atom, Θ the coverage and T_C the Curie temperature of the materials (see Chapter 3 for more details). We can therefore deduce an order of magnitude for χ_{max} for all the kinds of structures. It appears that monolayer structures give the highest value of χ_{max} . In our case, we therefore limit our studies to such structures.

1.3 Sample preparation

All the experiments described in this manuscript have been performed on a Pt(111) surface. The sample was cleaned under UHV conditions by sequential cycles of 1300 eV Ar⁺ sputtering under normal incidence at 300 K and subsequent annealing at 800 K to allow sufficient mobility of the Pt atoms to avoid uneven removal of material from the surface [37–39]. The typical sputtering current is about 0.3 μA during 20 minutes. Under these conditions (see top of Fig. 1.7), ≈ 15 ML are removed. After Ar⁺ sputtering, the sample is briefly exposed to 6×10^{-8} mbar oxygen at 800 K to remove carbon impurities by forming CO and CO₂ molecules which desorb. 800 K also corresponds to a O₂-desorption peak (see, e.g., [40–43] and Fig. 1.7 on the bottom). The sample is then flash annealed to 1350 K, followed by a slow cooling (-2 K/s from 1350 K to 1200 K, -4 K/s from 1200 K to 1050 K and then free cooling without any sample heating). The flash annealing activates all diffusion processes and prevents deep residual contaminant to diffuse to the surface while slow cooling is necessary to allow smooth restructuring of the surface. This preparation routine gives typical terrace sizes of about 1500 Å. For the prepared surface, we observed a coverage of less than 0.05% of a monolayer (ML) impurities. Prior to deposition at low temperatures, the sample was flashed to 800 K to desorb any residual gas which may have adsorbed on the surface during cooling. Co and Fe are deposited by Atomic Beam Epitaxy (ABE) from well outgassed high purity rods (99.995%, Alfa Aesar) using a commercial electron beam evaporator (Triple-evaporator Omicron). Pt and Pd are deposited by ABE from a home built evaporator. A filament of the desired species is heated up by Coulomb effect until the sublimation point is reached. It is worth noting that atomically controlled deposition of Pt and Pd is possible under UHV conditions since their melting point is much higher than their sublimation point, which is not the case for Fe and Co. In all cases, the deposition flux was calibrated to perform deposition in the timescale of one minute ($5 \times 10^{-4} - 7 \times 10^{-3}$ ML/s) which is a good compromise between accuracy and exposure to impurities coming from the evaporator. The base pressure during deposition was always in the 10^{-11} mbar range. The magnetic and

1.3. SAMPLE PREPARATION

topographic characterizations were always performed as fast as possible (the MOKE measurements usually started 20 minutes after deposition while, the first STM topographs were taken after 40 minutes after preparation) in order to avoid surface contamination by residual gas (mainly CO, CO₂, O₂, H₂O).

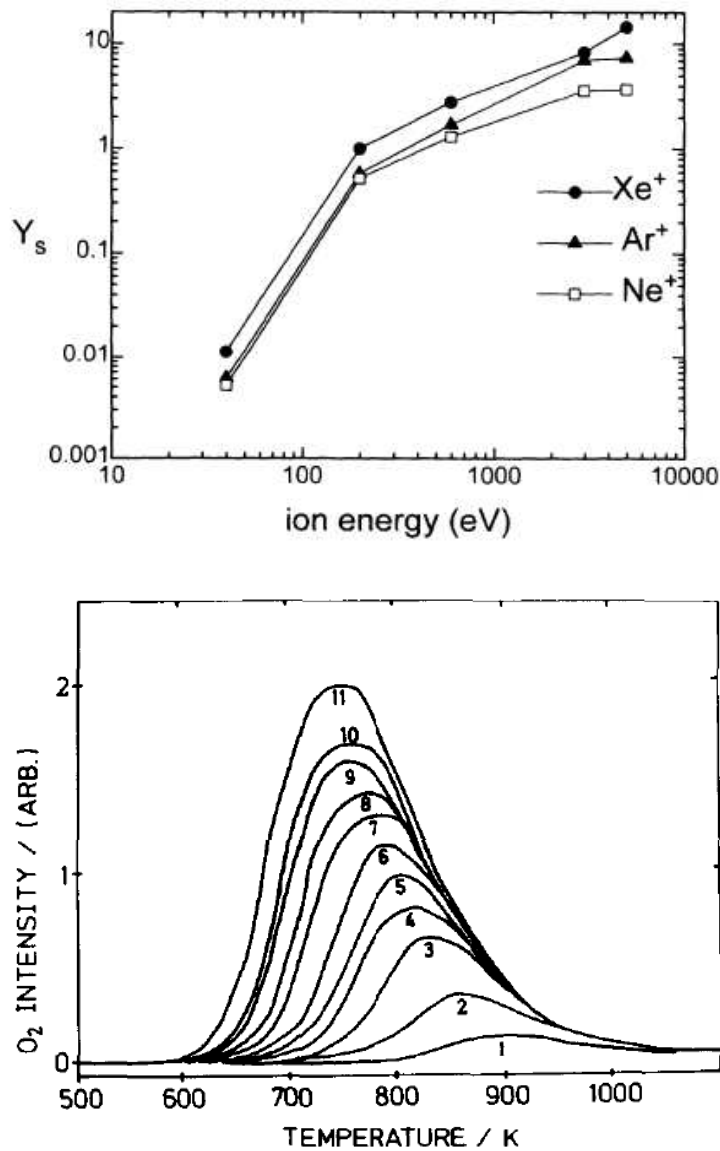


Fig. 1.7 – (top) Sputtering yields Y_s determined by STM for Pt(111) bombardment with Xe⁺, Ar⁺, and Ne⁺ at $T_b = 150$ K and at normal beam incidence (from [38]). (bottom) Thermal desorption spectrum for O₂ after various exposures (normal beam incidence) of an effective O₂/Pt(111) pressure of 1.4×10^{-7} mbar, from (1) 0.62 L to (11) 111 L (1 Langmuir = 1 L = 10^{-6} mbar.s). Our case corresponds to 6–7 with ≈ 20 L at 800 K which corresponds to a peak of O₂ desorption (from [41]).

Nucleation and growth of Fe on Pt(111)

2

Epitaxial growth of Fe on Pt surfaces is the subject of ongoing research [44–46]. Particular emphasis has been put on the creation of the FePt alloys. The magnetic properties of the ordered phases are of interest in magnetic data storage [47–51]. In addition, the catalytic properties of these alloys are highly appreciated [52–54]. Hence, the onset of Fe/Pt alloy formation has been widely studied by means of a palette of surface techniques comprising Auger Electron Spectroscopy (AES), Low Energy Electron Diffraction (LEED), X-ray Photoelectron Spectroscopy (XPS), Low Energy Ion Scattering (LEIS), Thermal Energy He Atom Scattering (TEAS), Infrared Reflection Absorption Spectroscopy (IRAS), Scanning Tunneling Microscopy (STM) [44, 45, 55–57]. As an example, Jerdev *et al.* [55] have shown the onset of alloy formation at 350 K upon deposition of 0.65 ML of Fe on Pt(111).

Albeit important efforts to describe the equilibrium configuration of Fe films on Pt surfaces, until present little was done to understand the kinetics of nucleation and growth of submonolayer quantities of Fe on Pt. This critical point is, yet, the cornerstone for the built-up of tailored nanostructures as we will see in Chap.4. An STM, with its spatial resolution, allows to quantitatively determine structural surface properties, such as size and shape of the nanostructures, dislocations, and intermixing. Spatially average properties such as the island density can also be found. A Variable-Temperature Scanning Tunneling Microscope (VT-STM) exhibiting a high resolution is perfectly suitable to define key parameters of nucleation and growth processes : activation energies are, e.g., directly inferred from structural evolution of Fe nanostructures with the sample temperature.

In this chapter, we report on a study of nucleation and growth of Fe deposited on a Pt(111) surface by Atomic Beam Epitaxy (ABE). First a short introduction to the theory of nucleation is given. In a second step the importance of kinetics in thin film growth is outlined, leading to the development of mean-field nucleation theory.

The comparison of the experimental results with mean-field theory of cluster diffusion allows one to infer activation energies of monomer, dimer and trimer diffusion. The binding energy of Fe adatoms on a cluster edge is inferred from the onset of Ostwald ripening. The ability to grow density controlled islands by means of the scaling law of nucleation is demonstrated. In a second part, the formation of monatomic Fe wires randomly distributed over the terraces is described. The presence of loops of such wires is equally observed. An investigation about the origin of wire formation is presented. A possible nucleation process is eventually given.

2.1 Introduction to the theory of nucleation

2.1.1 State of the art

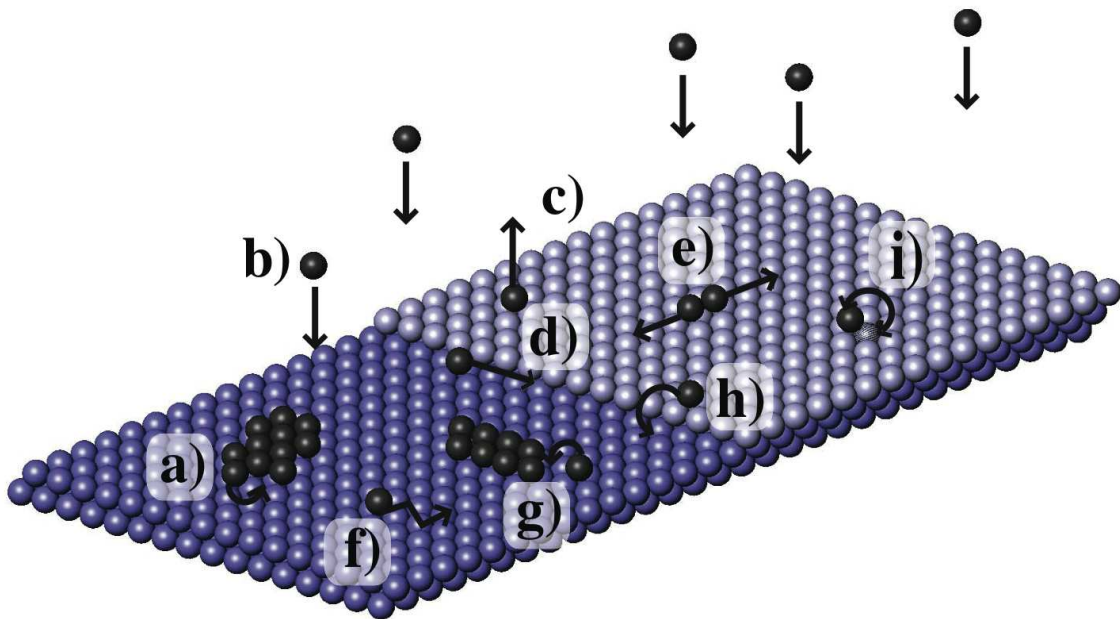


Fig. 2.1 – Typical atomistic processes during epitaxial growth. (a) edge diffusion, (b) deposition (F), (c) re-evaporation, (d) step diffusion, (e) dissociation, (f) terrace diffusion, (g) aggregation, (h) step descent, (i) exchange.

In the following paragraph all important parameters to describe growth on the atomic scale are listed and explained. The main processes that occur during epitaxial growth are illustrated schematically in Fig. 2.1. Atoms were deposited by ABE onto a perfect substrate surface. With a perfect substrate we refer to a clean surface with large terraces that have no screw dislocations. The deposition flux F is expressed typically in monolayers per second ($\text{ML}\cdot\text{s}^{-1}$) where monolayer refers to the number of

atoms per unit cell. Once the atoms are in contact with the surface they are named adatoms. They diffuse with a tracer diffusion coefficient D (in $\text{site}\cdot\text{s}^{-1}$), describing the mean square displacement of one isolated random walker per unit time. Adatoms near the step edge of a terrace can jump from one terrace to the other or diffuse along the step. When an adatom meets another adatom, they form a dimer. An adatom can also attach to an existing island. An adatom, that is attached to an island, can detach from the island edge or diffuse along the island edge. Direct deposition of adatoms on top of an island and the corresponding processes have to be considered as well. At high temperatures, some adatoms can re-evaporate. Each of these processes described above is characterized by an energy barrier E and an attempt frequency ν_0 . This model is illustrated by an adatom diffusing randomly on the surface by hopping between adjacent adsorption sites with a hopping rate ν given by the Boltzmann term :

$$\nu = \nu_0 \exp \frac{-E_m}{k_B T} \quad (2.1)$$

where k_B is the Boltzmann constant, E_m the activation energy for the diffusion process and T the substrate temperature. In case of low temperatures, the dynamic temperature dependent contribution of the activation energy is small compared to the static contribution that is temperature independent. So, for many purposes it suffices to assume E_m to be temperature independent and to assign it with a static barrier. One can interpret ν_0 as the oscillation frequency of the atom in the potential well caused by the surface corrugation, and therefore, as the atom attempt rate to overpass the energy barrier E_m . Nevertheless, this simple model of a harmonic oscillating atom is valid only under the condition $k_B T \ll E_m$. Typically, ν_0 corresponds to the values of the crystal lattice vibrations, also known as phonons (i.e. from 10^{11} to 10^{14} Hz). It has been shown by molecular dynamics (MD) simulations [58, 59] and experimental observations [60, 61] that ν_0 is constant over a large range of temperatures.

Random walk statistics describe the mean square displacement of diffusing species in terms of the number of hops N and the distance covered per hops l . The number of successful hops can be obtained by multiplying the hopping frequency ν by the time allowed for diffusion, t . In the most basic model only nearest-neighbor hops are considered and l corresponds to the spacing between nearest-neighbor adsorption sites. The root mean square displacement goes as $\langle \Delta r^2 \rangle = l^2 \nu t$. The so-called Einstein relation states $\langle \Delta r^2 \rangle = 2dl^2 Dt$ with d referring to the dimensionality of the motion. In case of an fcc(111) surface d has a value 1.5 [62]. It is therefore straightforward to deduce D out of ν :

$$D = \frac{1}{2d} \nu = \frac{1}{3} \nu_0 \exp \frac{-E_m}{k_B T} \quad (2.2)$$

The last 40 years were dedicated to intensive research activities in order to describe the relation between D and the measurable nucleation rate. This description would allow to determine the energy barriers and the attempt frequencies. During these years various theories delivering Arrhenius plots with different accuracies were

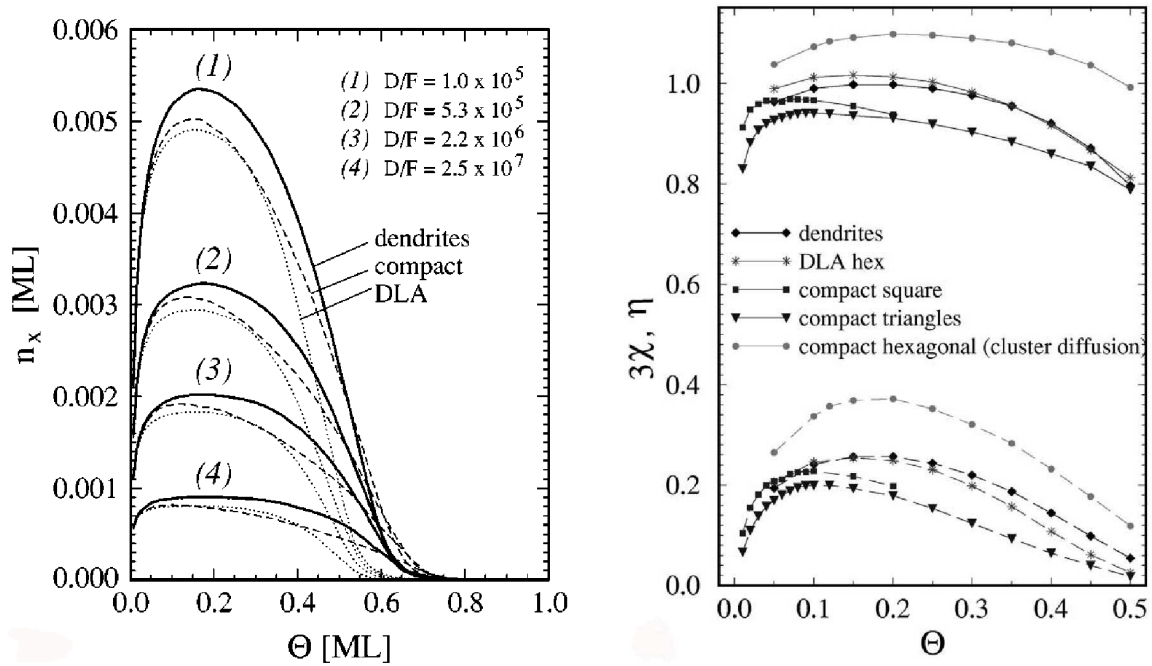


Fig. 2.2 – (left) Island densities for three island shapes that can be realized on a hexagonal lattice. KMC simulations show that coalescence sets in abruptly for dendrites and diffusion-limited aggregation (DLA), whereas compact islands show an extended coalescence regime. (right) The exponent χ and the prefactor η (see full and dashed lines) appearing in the scaling law Eq. 2.3 as a function of coverage for various island shapes. χ was scaled such that deviations from the classical value $\chi = 1/3$ become apparent. The KMC simulations for dendrites, DLA clusters, and two types of compact islands were performed on a hexagonal lattice. We also show KMC results for compact islands on a square lattice [63].

developed (for a review, see, e.g., [64]). In the following we list the different theories with an increasing CPU time consumption. The rate equations (RE) from mean-field nucleation theory [65–67] express the time evolution of the nucleation island densities as a set of coupled ordinary differential equations (ODEs). Kinetic Monte Carlo (KMC) simulations [68] and molecular dynamics (MD) simulations [69] are atomistic models that explicitly take into account the stochastic nature of each microscopic process that may occur during nucleation and growth of thin films. The main advantage of the mean-field nucleation theory is that the differential equations are simple to solve. Their main drawback is that they do not contain any spatial information. Therefore in order to describe phenomena as coalescence and islands size distributions KMC simulations have to be used.

A major result from mean-field nucleation theory is the so-called *scaling law*. It describes the nucleation process of stable islands in the steady state regime^a for the case of complete condensation (no re-evaporation) and two-dimensional (2D) islands :

$$n_x \simeq \eta(\theta, i) \left(\frac{D}{F}\right)^{-\chi} \exp\left[\frac{E_i}{(i+2)k_B T}\right] \quad (2.3)$$

where the scaling exponent $\chi = i/(i+2)$, i denotes the critical cluster size, and E_i its binding energy. A critical cluster becomes a stable one upon incorporation of one extra atom. A stable cluster means that it grows more rapidly than decays in the course of the deposition procedure. In case of a critical cluster size of 1 (monomer), the expression is reduced to $n_x = \eta \left(\frac{D}{F}\right)^{-1/3}$. It has been shown that this equation is applicable for temperatures where $D/F > 10^5$ and as long as the assumption $i = 1$ and complete condensation hold true. In this model, the dimensionless prefactor η slightly varies with coverage following $\eta \propto \theta^{\frac{1}{(i+2)}}$ around a plateau at 0.25 [70]. KMC simulations have shown that a correction due to the coverage, the shape of the clusters and the value of D/F has to be added to η and χ in order to fully describe the experiments with the scaling law (see Fig. 2.2 (right)) [62]. The authors of this study have equally pointed out that the island density, at least the one for compact or semi-compact, isotropic islands, is not very sensitive to island shape. Another level of sophistication in modelling is to combine KMC with DFT-calculations. This is known as molecular dynamics. It has been used to show that repulsive medium-range, substrate-mediated [71, 72] as well as long-range interactions [73] can inhibit island nucleation or even cause the formation of monatomic 1D wires. Hence the question arises, whether the energy barriers estimated by mean-field theory for diffusion are overestimated in such cases [74]. Some recent extensions of mean-field theory for nucleation and growth on either strained surfaces [75] or in presence of repulsive adsorbate interactions [76] might give a hint toward an answer.

^athis regime corresponds to the pure growth regime where adding material does not change the island density.

2.1.2 Deducing the energy barriers from experiments

In this section are outlined the different kinds of nucleation and growth experiments which allow determining the energy barriers of the different processes by means of an STM. A description of the rate equation model used in this chapter to fit the data is given.

State of the art

One can distinguish four successive regimes in the growth of islands by ABE. These regimes are visible in Fig. 2.2 (left) which represents the density of stable islands as a function of the coverage calculated by KMC for different kinds of clusters and different D/F (from [63]) ratios. The first regime, typically for coverages below $0.01 ML$, is the so-called *pure nucleation* regime. Within this regime, an additional deposition of atoms predominantly results in the formation of new nuclei. Increasing the coverage further leads to the *transition from nucleation to growth* regime. The next regime called *pure growth* or *steady state* or saturation regime, refers to the coverage interval when the island density has saturated (typically between $0.10 ML$ and $0.30 ML$). In Fig. 2.2 (left), this regime is featured by a plateau of the density of stable islands whatever the ratio D/F and the cluster shape are. The last regime corresponds to the *coalescence* of islands.

Initially, the energy barriers as well as the attempt frequencies were determined by means of Arrhenius plots at the saturation coverage. An Arrhenius plot reports the logarithm of one quantity here the island density n_x as a function of the inverse temperature $1/T$. The diffusion parameters can be extracted by fitting the data using the appropriate theory in its range of application. Fit by means of scaling law gives very satisfactory results of the activation energy of monomer diffusion.

In the system Ag/Pt(111), the average cluster size was represented as a function of the annealing temperature for a coverage of $0.10 ML$ [62]. The Ag atoms were first deposited at $50 K$. At this temperature, the diffusion process are frozen leading to statistical growth. This procedure gives insight into activation temperatures of diffusion or dissociation processes, and thus allows estimations of energy barriers. The authors could therefore determine the $i = 1$ regime and the activation energy corresponding to monomer diffusion.

Bott *et al.* proposed another method to extract quantitative information on diffusion from nucleation for a homoepitaxy Pt(111) system [77]. The method called *nucleation curve method* consists in measuring the onset temperature of nucleation arising from the onset of diffusion from an Arrhenius plot with much smaller amounts (*pure nucleation* regime). This method provides results that are in excellent agreement with nucleation theory.

The complementarity between nucleation curve method and saturation islands density method from one part and annealing of monomers and subsequent coarsening, also referenced as ripening experiments, from the other part was already proved. As an example, Ph. Bulushek et al. has performed both saturation island density

method and ripening experiments in the system Co/Pt(111) and extracted similar energy barriers with both methods [78] and with KMC simulations. To perform the ripening experiments, Bulushek and coworkers have deposited small amount of Co at low temperature and monitor the mean island size by means of an STM after each annealing step. The temperatures are typically between 40K and 350K.

Nucleation and growth results of Fe on Pt(111) are presented within the framework of such ripening experiments under the assumption of a value for the attempt frequency. This method benefits from the advantages of low coverage while it provides information beyond the nucleation regime as, e.g., it shows the difference between dimer diffusion and dimer dissociation.

Modelling ripening experiments by means of rate equations

In this chapter, nucleation parameters such as energy barrier and attempt frequency for diffusion are induced from a fit of our data with a rate equation model.

A code written by H. Brune and Ph. Bulushek was slightly modified so as to take into account tetramer diffusion. A rate equation describes the time evolution of mean-field quantities such as the densities n_s (per surface site) of clusters of size s . For the rate equations below, the following assumptions were made : first complete condensation is assumed meaning that no reevaporation of the surface atoms occur. Secondly it is supposed that all clusters larger than four atoms are stable and thus, accounted for in n_x . Therefore, the density for each cluster size after deposition can be written as :

$$\frac{dn_1}{dt} = - \sum_{j=1}^4 (\sigma_1 D_j + \sigma_j D_1) n_1 n_j - \sigma_x D_1 n_1 n_x \quad (2.4)$$

$$\frac{dn_i}{dt} = \sum_{h,k(h+k=i)} \sigma_h D_k n_h n_k - \sum_{j=1}^4 (\sigma_i D_j + \sigma_j D_i) n_i n_j - \sigma_x D_i n_i n_x \quad (2.5)$$

$$\frac{dn_x}{dt} = \sum_{h,k(h+k>4)} \sigma_h D_k n_h n_k \quad (2.6)$$

$$(2.7)$$

where σ_s corresponds to the capture efficiency of a cluster of size s [67] and D_s is its tracer diffusion defined in Eq. 2.2. The density of a cluster of size i increases when a diffusing cluster of size k ($k < i$) is captured by a cluster of size h ($h + k = i$), which is represented by the term $\sigma_h D_k n_h n_k$. In contrary, n_i decreases when a cluster of size i is captured by a cluster of size j (note that j may be equal to i) and the other way around, which is represented by the term $(\sigma_i D_j + \sigma_j D_i) n_i n_j$.

The mean island size is given by the quotient $\Theta / (n_1 + n_2 + n_3 + n_4 + n_x)$.

At very low temperature, i.e., at temperature when classical diffusion processes are frozen, the model should include *easy attachment* and/or *transient mo-*

bility [62, 63, 78, 79]. *Easy attachment* takes place when the energy barrier of monomer diffusion in the vicinity of another cluster is lower than one on the terrace, whereas *transient mobility* is temperature independent and can be present far from another cluster. *Transient mobility* was already observed by Wang and Ehrlich [79] by means of Field Ion Microscopy (FIM) for Ir/Ir(111). In our RE, one can easily adapt *easy attachment* as an upper limit of the mean island size by considering direct impingement of incoming atoms up to a distance of two sites from another adatom.

2.2 From monomer diffusion to spontaneous wire formation

2.2.1 Experimental

We have deposited low coverages (typically 0.01 ML) of Fe monomers by ABE on a Pt(111) surface with the deposition rate $F = 1.0 \pm 1.0 \times 10^{-3} \text{ ML.s}^{-1}$ at temperature of 40 K, 47 K and 60 K. At these temperatures, thermally activated diffusion is frozen and deposition leads to statistical growth as it was confirmed by experiments. All experiments presented in this section were carried out over a span of a few weeks in order to ensure the reproducibility of the experimental conditions. The base pressure was 3×10^{-11} mbar. During all deposition and measurement the pressure never exceeded 6×10^{-11} mbar. The Pt(111) surface was cleaned following the classical *sputtering - O₂ - flash* process described in the previous chapter that guaranties a clean surface with typical terrace width of 2000 Å.

After deposition, the sample was heated up to the temperature T_{ann} and was annealed during ten minutes. After each annealing the sample was cooled to a temperature typically 20 K below T_{ann} . This process ensures to freeze the nucleation process immediately after annealing and during all the characterization. STM topographs were recorded in order to determine the density and mean size of the islands. The scans last generally 2 hours.

Determination of the mean island densities The mean island size $\langle s \rangle$ is the ratio of the coverage θ over the island density $\sum_i n_i$. Care was taken to determine the mean island size for reasonable error bars. Here, θ refers to the nominal coverage. The Fe flux was previously calibrated by STM at room temperature for a coverage around 0.5 ML. An uncertainty of 10% on the evaluation of θ is estimated. The following factors have an impact on the uncertainty in the determination of the island density.

-thermal drift : Temperature gradients occur in the STM head, typically on the contact between the piezoelectric "foot" and the ramps for coarse approach. Such a gradient contributes a drift \vec{v}_d to the scanning speed \vec{v}_s . This drift can falsify the observed island density up to 20% of its value. Moreover, the area of the surface scanned S_s varies depending on the direction of the scan. The effect is essentially

2.2. FROM MONOMER DIFFUSION TO SPONTANEOUS WIRE FORMATION

visible in the vertical direction since the vertical scan is 1024 times ^a slower than the horizontal scan. The influence of the temperature drift can be expressed as $v_s(y) + v_d(y)$ in one direction and $v_s(y) - v_d(y)$ in the opposite direction. The influence on the area of the scanned surface is analogous : $S_s + S_{dy}$ and $S_s - S_{dy}$. As a consequence, in order to get rid of this artefact, we have simply recorded STM topographs from top to bottom and than from bottom to top. The island density values of one and its opposite direction were averaged.

- low number of images per annealing temperatures : at low temperatures, a large thermal drift and vertical noise make it very tough to record STM topographs with a high resolution. Hence, less than ten STM topographs could generally be recorded with a total number of clusters of about 400 – 1000. Fig. 2.3 shows an example of how the island density distribution varies. Pure statistical considerations predict that in case of similar image sizes over all the measurements, the standard deviation of the island density distribution should be a factor $1/\sqrt{n}$ of the mean island density, where n is the average number of islands per image couple. For example, at an annealing temperature of $T_{annealing} = 120$ K, the standard deviation of the island density distribution is 18% which is comparable to the 13% yielded by $1/\sqrt{n}$.

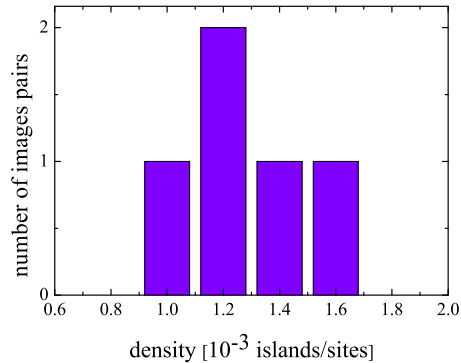


Fig. 2.3 – *Distribution of the island density per couple of images scanned from top to bottom and the other way around. Standard deviation represents less than 20 % of the average density value.*

From all the above mentioned contributions to the uncertainty in the mean island size, an error bar of 30% of the value is estimated. By repeating experiments over a large range of annealing temperatures, a complete ripening profile was produced.

^aas the traditional number of pixels in one line and one row in the STM topographs is 512 and the scans are up and down.

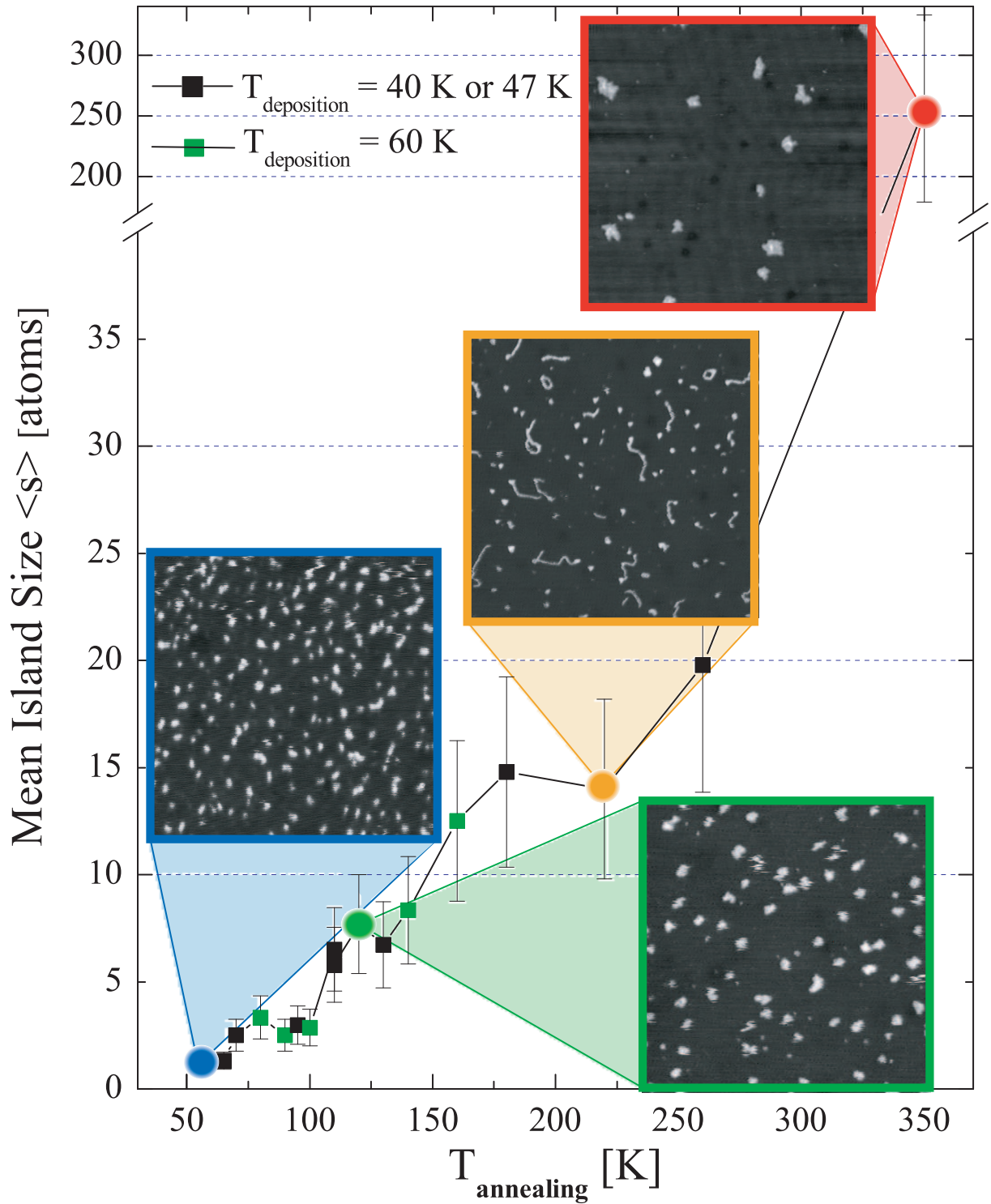


Fig. 2.4 – Mean island size versus annealing temperature. In insets, STM topographs of Fe on Pt(111) deposited below 60 K then annealed to 65 K (blue frame, $500 \times 500 \text{ \AA}^2$, $\Theta_{\text{Fe}} = 0.005 \text{ ML}$), 120 K (green frame, $500 \times 500 \text{ \AA}^2$, $\Theta_{\text{Fe}} = 0.01 \text{ ML}$), 220 K (orange frame, $1000 \times 1000 \text{ \AA}^2$, $\Theta_{\text{Fe}} = 0.008 \text{ ML}$) and 350 K (red frame, $1000 \times 1000 \text{ \AA}^2$, $\Theta_{\text{Fe}} = 0.017 \text{ ML}$).

2.2.2 General overview

Fig. 2.4 shows the mean island size as a function of annealing temperature. The plot shows the mean island size to increase monotonically with the annealing temperature. It reveals four different kinds of ripening processes. From 55 K to 130 K , we observe a stepwise increase with the first level starting at 55 K with a mean size $\langle s \rangle = 1.2 \pm 0.3$ atoms. The second level starts at 70 K with a mean island size $\langle s \rangle = 2.7 \pm 0.2$ atoms^a, while the third has an onset at 110 K with $\langle s \rangle = 6.7 \pm 1.0$ atoms. The threshold of each transition curve temperature stands for the activation energy for the monomer, dimer and trimer diffusion. In the temperature interval from 130 K to 160 K , the coarsening is well described by the exponential growth curve of the 2D Ostwald ripening, where the large clusters grow at the expense of the smaller ones. From 160 K to 260 K , the behavior of the mean size does not follow the typical curve for 2D Ostwald ripening. We observe coexistence of wires and small ($s \leq 10$) clusters in this temperature range. At 350 K , only compact clusters were observed. At this temperature the mean island size is much larger, $\langle s \rangle = 250 \pm 70$ atoms.

2.3 Low temperature ripening processes

2.3.1 55 K to 130 K : cluster diffusion

As an overview of the processes occurring between 55 K and 130 K , three STM topographs in Fig. 2.5 illustrate the stepwise variation of the mean island size with annealing temperature. As outlined before, the mean island size directly reflects cluster mobility and is, hence, expected to follow the mean-field rate equation model over a wide range of temperature. Fig. 2.5(a) refers to the plateau between 55 K and 70 K . Clusters appear as bright spot with relative height of 0.7 ± 0.3 Å. The attained resolution does not allow a distinction between monomers and dimers. The broad distribution of the relative height can be explained by the large vertical noise ($\Delta_{z,pp} = 0.25$ Å), which broadens the height distribution. The high cluster density inhibits the determination of the averaged surrounding substrate level. As a consequence the relative height is underestimated. Since the nominal coverage is well known, one obtains a mean island size of 1.25 ± 0.3 atoms which is in good agreement with 1.1 atoms predicted by RE and KMC simulations. KMC simulations were performed by Bulushek [78] in the case of monomer and dimer diffusion. RE and KMC show very similar results until trimer diffusion is activated. We have equally performed RE simulations without taking account of *easy attachment* in order to quantify this effect. Therefore, in this case, the mean island size at 55 K is estimated to be 1.04 atoms. A comparison between RE without *easy attachment* and KMC calculations (taking into account this effect) is given in Fig. 2.6 (top) at $T_{annealing} = 50$ K and 75 K. At $T_{annealing} = 75$ K, monomer diffusion is activated. The proportion of

^aHere, the error bars refers to the standard deviation of the mean island size distribution on each step. The error bars for individual sample being 30% as explained earlier.

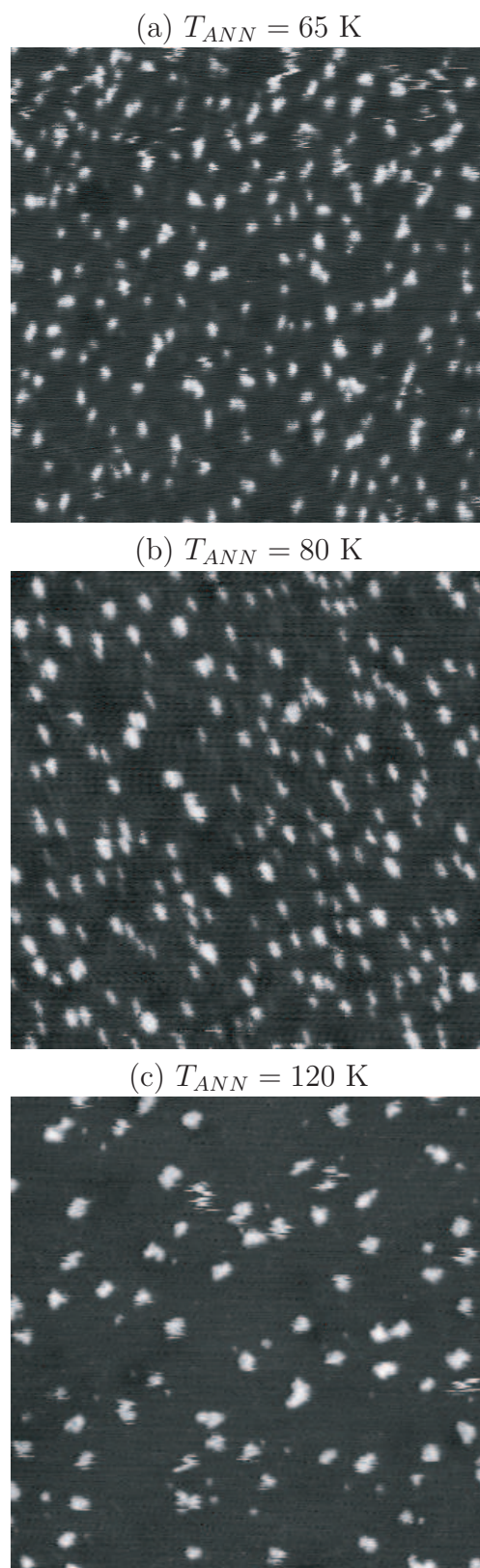


Fig. 2.5 – $500 \times 500 \text{ \AA}^2$ STM topographs of 0.005 ML (top) or 0.01 ML (central and bottom) of Fe on Pt(111) deposited at 40 K, then annealed to 65 K, 80 K and 120 K, from top to bottom. The density evolution enables to infer the hierarchy of activation energies of the atomic displacements.

2.3. LOW TEMPERATURE RIPENING PROCESSES

different cluster size from monomer to x-mer with $x > 4$ is given in Fig. 2.6 (bottom). RE and KMC are in very good agreement at 75 K and in relatively good agreement at 50 K. For the latter, thermally activated diffusion processes are frozen. Hence, statistical growth governs the size distribution. At a temperature of 50 K, monomers represent 91.6% of the total number clusters, dimers are 7.6% and 0.8% of the clusters are of larger size following the prediction of KMC simulations. RE predicts 96.5% of monomers, 3.3% of dimers and 0.1% of clusters of larger size. The difference between the results of the two methods comes from the fact that KMC simulations take into account *easy attachment* of an adatom in the vicinity of a cluster which has its prominent effect at low temperatures. It is worth noting that after activation of monomer diffusion on terraces activation, the effect of *easy attachment* can be neglected.

Fig. 2.5(b) shows an STM topograph of a sample annealed to 80 K. The Fe cluster have a relative height distribution between 1 and 1.5 Å which does not allow to distinguish between the different cluster sizes. The mean island size is estimated from STM topographs to be 3.3 ± 1.0 atoms. Over the temperature range 70 K to 110 K, the mean island size remains within the error bar constant around the averaged value $\langle s \rangle = 2.7 \pm 0.2$ atoms. The experimental values are in perfect agreement with RE after activation of monomer diffusion, yielding 2.7 atoms. By performing experiments with coverages going from 0.005 ML to 0.01 ML, we could show that the mean island size was independent of the coverage. This behavior is characteristic for annealing effect deposition under statistical growth conditions.

Fe structures after subsequent annealing to 120 K are compact clusters represented in Fig. 2.5(c) with mean island size $\langle s \rangle = 7.7 \pm 2.1$ atoms. The averaged cluster size between 110 K and 130 K is $\langle s \rangle = 6.7 \pm 1.0$ atoms. RE predicts that this value corresponds to the activation of dimer and trimer diffusion. Within experimental error bars, tetramer diffusion has also to be considered.

Fig. 2.7 represents the mean island size versus the annealing temperature. The curves are RE fits to the experimental values with different energy barriers and an attempt frequency of $\nu_0 = 5 \times 10^{13}$ Hz for monomers, dimers, trimers and tetramers (represented with red dots). The plateaus of the mean island size are very well reproduced by the mean-field model until a temperature of 110 K. The model including (dark yellow curve) and the model excluding (green curve) tetramer diffusion and considering mono-, di- and trimer diffusion both fit to the last plateau within the error margins. In the case considering (and not considering) tetramer diffusion, the best fit is with the following energy barriers :

- monomer :

$$E_{m1} = 190 \pm 10 \text{ meV} \quad (E_{m1} = 190 \pm 10 \text{ meV without tetramer diffusion})$$

- dimer, trimer and tetramer :

$$E_{m2} = E_{m3} = E_{m4} = 295 \pm 10 \text{ meV} \quad (E_{m2} = E_{m3} = 290 \pm 10 \text{ meV})$$

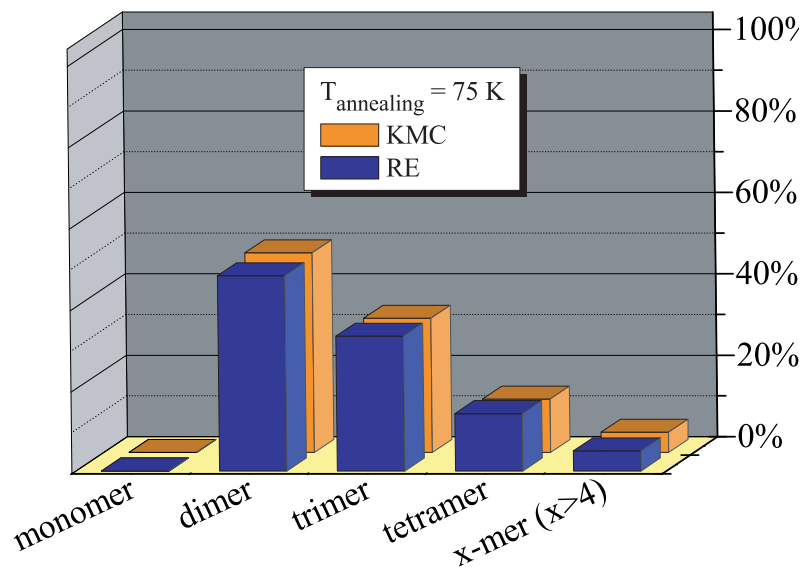
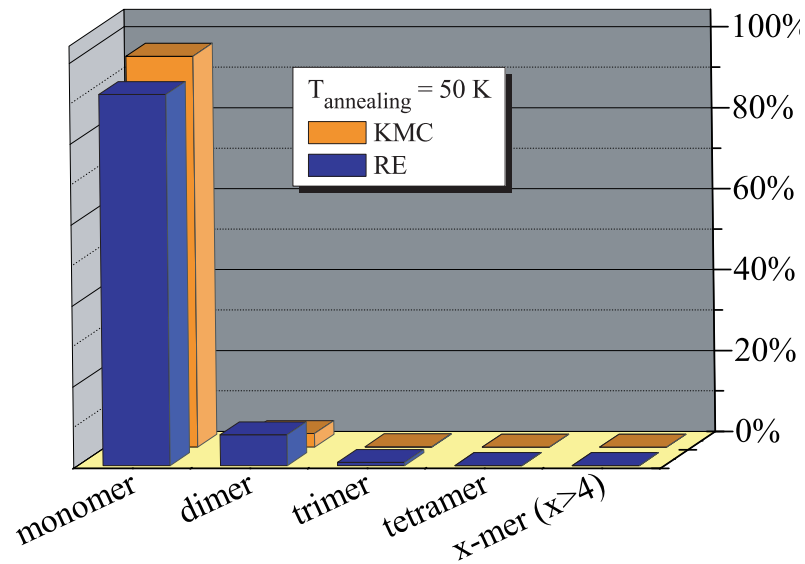


Fig. 2.6 – Island size distribution calculated using RE (blue) and KMC (orange) after deposition at 40 K then 10 minute annealed to 50 K (top) and 75 K (bottom) which activates monomer diffusion. KMC and RE are in good agreement. The difference at 50 K comes from the easy attachment process which is not taken into account in RE.

2.3. LOW TEMPERATURE RIPENING PROCESSES

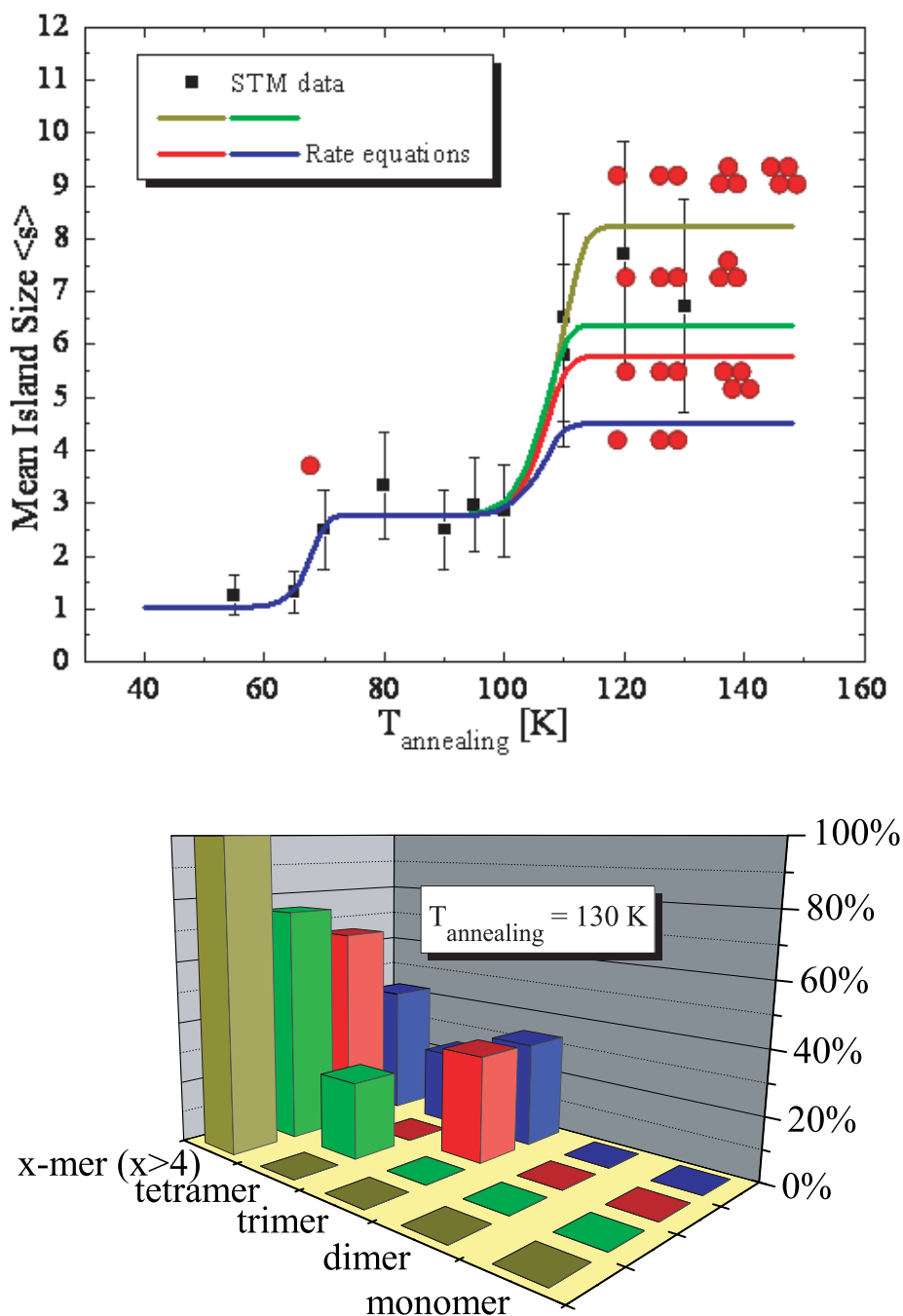


Fig. 2.7 – (top) Mean island size versus annealing temperature (zoom on low temperatures of Fig. 2.4). Every staircase in the curve indicates the onset of the monomer (68 K), dimer and tri(tetra)-mer (107 K) diffusion. Full lines represent the RE simulations with monomer, dimer (blue curve) and trimer (green curve), tetramer (red curve) or trimer and tetramer (dark yellow curve) diffusion. (bottom) Island size distribution calculated using RE after deposition at 40 K then ten minute annealed to 130 K. The color code in both figures is the same.

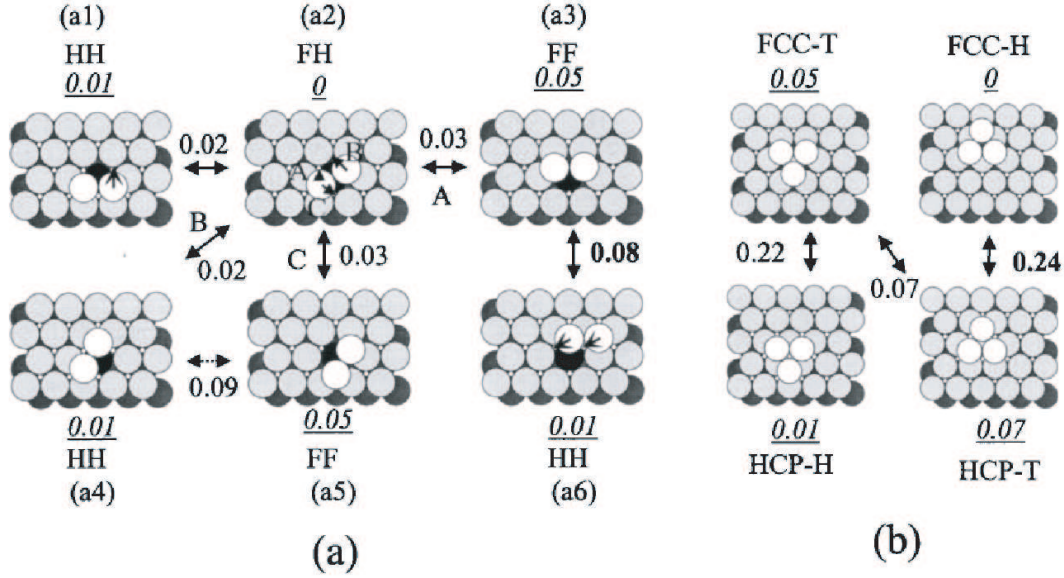


Fig. 2.8 – Examples of diffusion processes for (a) dimers and (b) trimers on fcc (111) surfaces. The energies indicated in this figure, that are related to the most stable configuration of each cluster, were obtained by DFT-LDA calculation for a $Al_n/Al(111)$ system. The bold numbers correspond to the free diffusion energies, and the italic numbers with underlines are the structural energies. The energy unit is eV [80].

The choice of a common attempt frequency for all cluster size was motivated by experimental [61] and theoretical [81] works on Pt(111) self-diffusion. In both cases, the attempt frequencies were observed not to vary with the different cluster sizes due to strong similarities in the diffusion mechanisms. Our result is comparable with 1×10^{14} Hz, found experimentally for a Co/Pt(111) system [78]. In Sec. 2.5.3, we will see that our fitted attempt frequencies and activation energies for monomer diffusion are in perfect agreement with the density of Fe islands in the steady state regime using the scaling law.

Our value for the monomer diffusion barrier is very close to the one of 200 ± 10 meV, found for Co/Pt(111). For Pt(111) the energy barrier for self-diffusion of a monomer is 260 ± 10 meV [61].

The most striking results concern the energy barriers for dimer, trimer and tetramer diffusion. The value of the mean island size plateau is higher after activation of a diffusion process. Here, the highest value for the mean island size is obtained after activation of mono-, di-, tri- and tetramer diffusion. In the case where tetramer diffusion is activated but not trimer diffusion, the mean island size is lower than in the opposite case since a large abundance of stable trimers is present among all clusters (see Fig. 2.7). According to our fit, the energy barriers of dimers and trimers (and possibly tetramers) do not differ a lot. This result contrasts with previous theoretical [80] and experimental [61, 82] determinations of the energy barriers of dimers and trimers in self-diffusion on fcc (111) surfaces such as Pt(111), Ir(111)

or Al(111). These works yield significantly higher activation energy for trimer than dimer diffusion. Until present, no such studies were performed for Fe on Pt(111). Fig. 2.8 shows some examples of dimer and trimer diffusion (from [80]). Chang *et al.* predicted that dimer and trimer self-diffusion on fcc (111) surfaces occur via a concerted motion rather than individual atomic jumps. However, both types of processes have been reported experimentally on an fcc (111) surface [82]. A contribution from the surface tensile stress on the diffusion process has also been pointed out by Bulou and Massobrio in a recent study of exchange diffusion in the case Pt/Pt(111) and Co/Pt(111) [83].

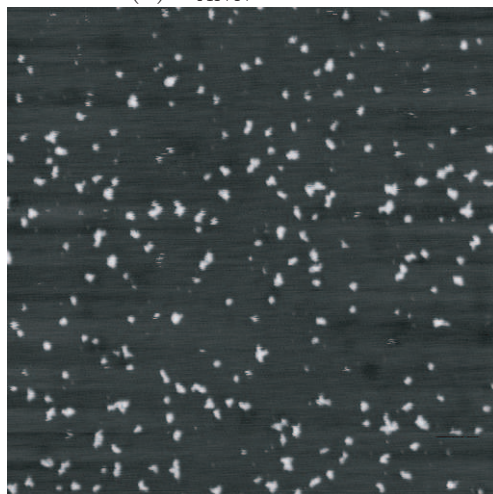
Time evolution of diffusion processes during annealing The size distribution calculated as a function of annealing time, indicates that at a temperature of 120 K, 96 % of all diffusion processes take place within the first minute of the overall annealing time. In contrary, at a temperature of 65 K, monomers remain stable on the overall timescale of deposition and during the 10-minute annealing. We have estimated by means of RE calculations, that after holding the sample during 3 hours and a half at 65 K, the mean island size to be 2.7 atoms. This result emphasizes the importance to freeze the sample after every annealing.

2.3.2 From 130 K to 160 K : Ostwald ripening

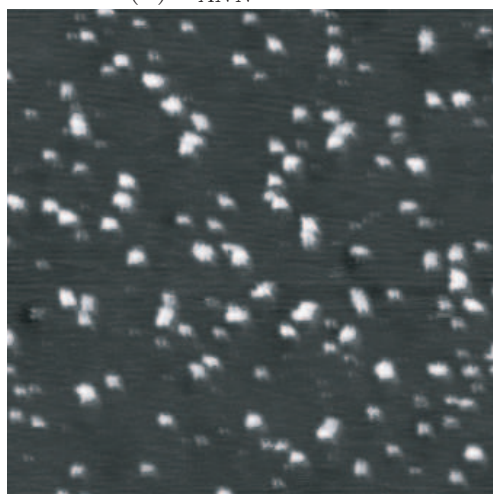
In the case of the samples that were annealed to temperatures between 130 K and 160 K, the coarsening mechanism has transformed from statistical growth, a pure monomer and cluster diffusion regime, to *Ostwald ripening* [62]. In this regime, larger clusters grow at the expense of neighboring smaller ones. Fig. 2.9 shows the respective STM topographs in the case $T = 130, 140, 160$ K. From these images, an estimate of the mean island sizes can be inferred : $6.8 \pm 2.0, 7.9 \pm 2.4, 12.6 \pm 3.8$ atoms for $T = 130, 140, 160$ K, respectively. In the pure diffusion regime, the mean island size increases step-wise with the annealing temperature. Here, the mean cluster size increases progressively with the annealing temperature. This behavior is characteristic for Ostwald ripening.

Estimation of the binding energy Ostwald ripening of Fe clusters involves dissociation of Fe atoms from small Fe clusters on the Pt(111) substrate with a binding energy E_b and the subsequent Fe diffusion on the Pt(111) surface towards a growing cluster with an activation energy E_m . The combination of these two processes gives rise to an activation energy for cluster ripening $E = E_b + E_{m1}$ and the respective coarsening rate $\nu'_0 \exp\left(\frac{-E}{k_B T}\right)$. For the following calculation we assume equal attempt frequencies for dissociation and diffusion. Taking the onset temperature of Ostwald ripening and the corresponding annealing times, we estimate the activation energy for Ostwald ripening to be $E = 425$ meV. With $E_{m1} = 185 \pm 10$ meV, the binding energy of the atoms of the smallest stable clusters, i.e. tetramers or pentamers, is calculated to be $E_b = 240 \pm 10$ meV. This estimation implies that the smallest clusters remain

(a) $T_{ANN} = 130$ K



(b) $T_{ANN} = 140$ K



(c) $T_{ANN} = 160$ K

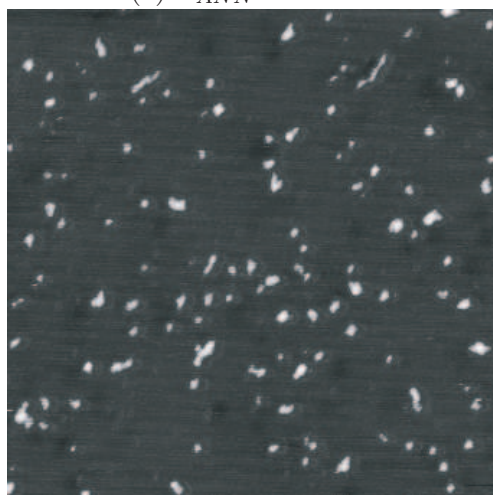


Fig. 2.9 – $1000 \times 1000 \text{ \AA}^2$ STM topographs of 0.0084 ML Fe on Pt(111) deposited at 40 K , then annealed to 130 K , 140 K and 160 K , from top to bottom. The cluster density decreases continuously with the annealing temperature due to a more rapid dissociation of smaller clusters (Ostwald ripening).

stable within the first minute of annealing to ~ 140 K. At ~ 160 K, the lifetime of a dimer is only about one second.

Remark concerning the presence of impurities In the following we will take a closer look at the shallow black depressions and the narrow white protrusions observed in almost all STM images in this manuscript. A systematic analysis of these structures was made on all samples. The white dots are 0.3 ± 0.1 Å high protrusions and the shallow holes are 0.20 ± 0.05 Å deep. With the same tunneling parameters, the standard deviation of the apparent dot height reduces to 0.05 Å. Their density is respectively about $5 \times 10^{-4} \pm 0.5 \times 10^{-4}$ dots/site and $3.5 \times 10^{-4} \pm 0.5 \times 10^{-4}$ holes/site on all samples. No noticeable variation of the densities was observed within all experiments. Therefore, we deduce that white dots and black holes are not composed of Fe, i.e. no Fe insertion in the Pt surface occurred. We associate the white dots to Oxygen impurities [84] and the shallow holes to Carbon subsurface atoms. It is worth noting that no spatial correlation was observed between the impurities and the Fe clusters and, hence, to the first order, we can exclude any influence of the impurities on the Fe diffusion processes.

2.4 Wire formation, from 160 K to 260 K

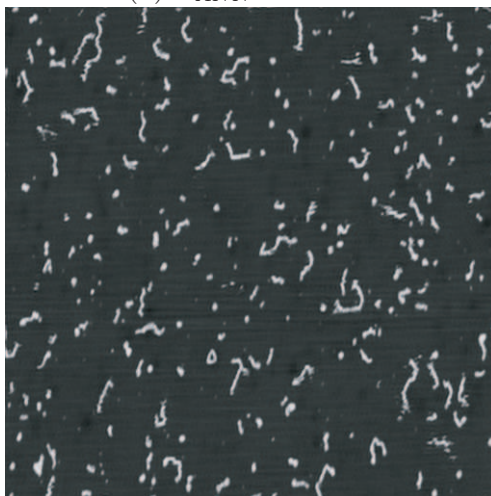
In this section, we report on the formation of nanowires in the temperature range $160 \text{ K} \leq T_{ann} \leq 260 \text{ K}$. Wire formation is first described qualitatively. Then, a more quantitative description of the wires is presented. The influence of annealing on growth as well as the role played by the coverage on the presence of the wires is reported. Eventually, the presence of wires is not detected at the highest annealing temperature of 350 K, suggesting that wire formation is governed by kinetics. We conclude with a discussion on a probable mechanism explaining their formation.

2.4.1 Wire formation

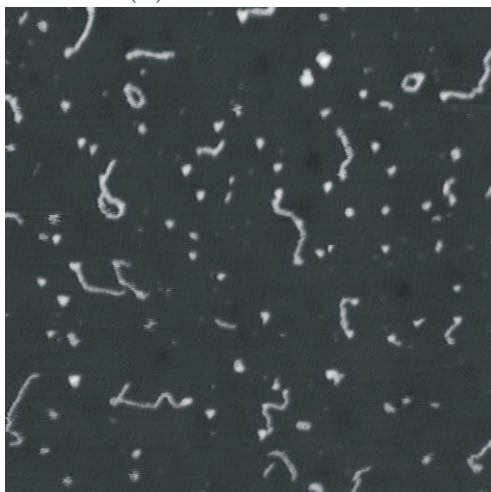
Previous observations of wire formation

Wires are generally observed as step decorations. [85–89]. Elongated clusters on anisotropic surfaces such as the (1×2) reconstructed and unreconstructed fcc(110) surfaces [90–92] represent an other kind of nanowires. An alternative to the self-assembly of atomic wires is to artificially built them by STM manipulation [93–95]. Conductivity measurements are also reported on suspended linear gold monatomic wires before rupture [96–100].

(a) $T_{ANN} = 180$ K



(b) $T_{ANN} = 220$ K



(c) $T_{ANN} = 260$ K

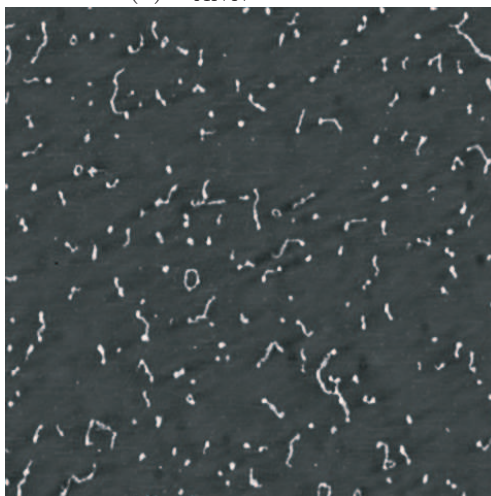


Fig. 2.10 – $2000 \times 2000 \text{ \AA}^2$ STM topographs of 0.0084 ML Fe on Pt(111) deposited at 40 K , then annealed to 180 K , 220 K (here, the image size is $1000 \times 1000 \text{ \AA}^2$) and 260 K , from top to bottom. Small clusters coexist with Fe wires and loops.

Wire formation in the present experiment

The three topographs in Fig. 2.10 show Fe on Pt(111) at annealing temperatures between 160 K and 260 K. On all topographs in this temperature range, we notice the presence of both wires and small clusters on the surface. A distinction between compact and elongated small clusters could not be achieved. Therefore, the total number of islands was used in the estimation of the mean island size without distinction between wire and "supposed" compact clusters. The mean island size is found to be 14.8 ± 4.4 , 14 ± 4.2 and 19.8 ± 5.9 atoms for $T_{annealing} = 180$ K, 220 K and 260 K, respectively. The cluster surface distribution as well as the perimeter distribution show similar features for all samples. Therefore, it has been possible to fit the cluster surface distribution in all samples by a single test function $y = Ae^{\alpha x}$, where $\alpha = (2.1 \pm 0.6) \times 10^{-3}$, y is the cluster abundance and x the cluster surface. A is the normalization constant.

2.4.2 Description of the wires

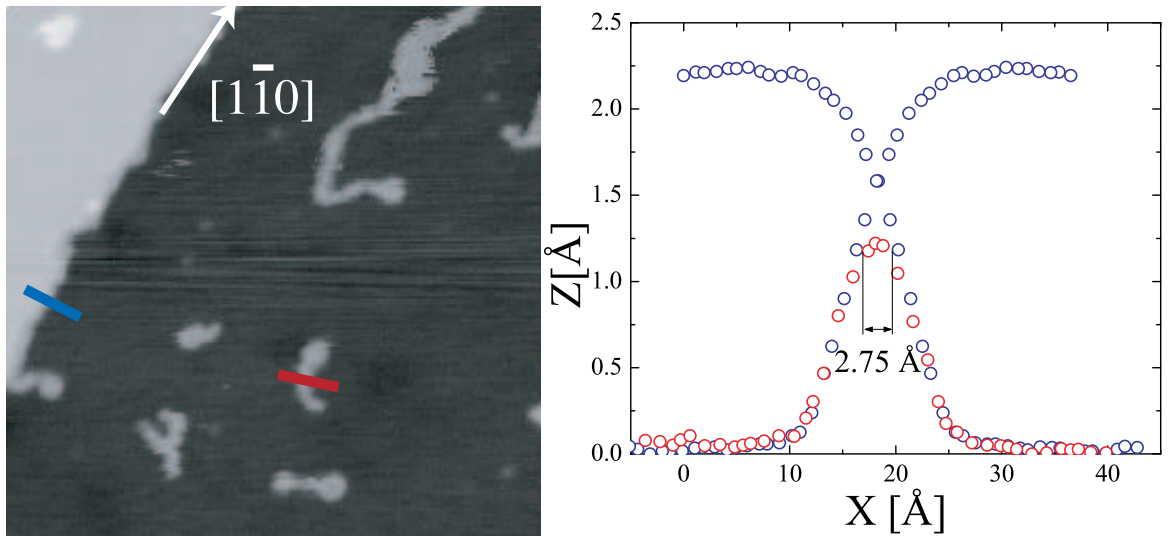


Fig. 2.11 – (left) $350 \times 350 \text{ \AA}^2$, STM topograph of 0.01 ML Fe on Pt(111) deposited at 40 K and annealed to 220 K. (right) Linecuts along the blue (step edge) and red (wire cross-section) lines. From a direct comparison between red and blue curves an estimate of 2.75 \AA for the wirewidth can be inferred.

In the following, some features of the Fe nanowires are described and discussed in the light of previous works on nanowires.

Method A closer look on the Fe nanowires allows one to draw conclusions on their structure. Under tunnel resistance around $10^8 - 10^{10} \Omega$, the nanowires appear as bright lines, with an apparent height of $1.2 \pm 0.1 \text{ \AA}$ (Fig. 2.11). This value agrees with the apparent height of Fe monomers on Pt(111) measured by Crommie et al.

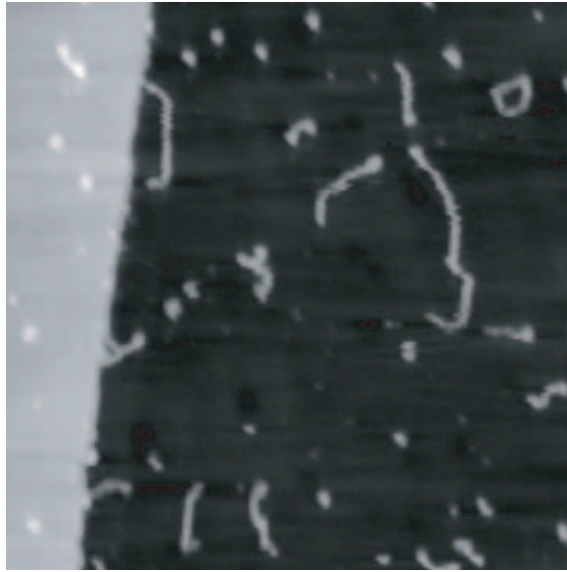


Fig. 2.12 – $700 \times 700 \text{ \AA}^2$, STM topograph of 0.01 ML Fe on Pt(111) deposited at 40 K and annealed to 220 K. Wires in contact with the step edge initiate growth at 60° with respect to it.

[101]. Compact clusters appear slightly higher around $1.4 \pm 0.1 \text{ \AA}$ and a Pt step-edge is imaged $2.30 \pm 0.05 \text{ \AA}$ high in agreement with the larger distance of 2.26 \AA .

Estimation of the wire width The wire width is estimated by means of a wire cross-section and a step-edge height profile. The step-edge height profile represents the convolution function between a heaviside function of a step-edge and the so-called *tip width*. Therefore, it is possible to estimate the wire width by subtracting from the height profile of the wire cross-section the part corresponding to the *tip width*. In Fig. 2.11 (right), a linecut of the step-edge and one of the cross-section of a wire along [112] are represented in blue and red lines, respectively. The mirror of the step-edge height profile is equally represented in blue. The wire width is evaluated as the distance on which step-edge and wire cross-section do not share a similar height profile. In Fig. 2.11 (right), we take advantage of the symmetric shape of the height profile of the wire cross-section to use both the step-edge height profile and its mirror to determine the wire width. In this figure, the wire width is estimated around $2.75 \pm 0.30 \text{ \AA}$. The process has been repeated on several wires and similar height profiles of wire cross-section was always found (see also Fig. 2.13). Therefore we conclude that wires are monatomic 1D wires.

Step-edge and wire Wires in contact with the Pt step-edge grow preferentially at 60° with respect to the step-edge. Fig. 2.12 shows three wires in contact with the step-edge that illustrate this particular growth. This result differs from the already well-established growth of Fe wires along the step-edge of a Pt(997) surface [45]. Generally, atoms are bound to steps stronger than on terrace. However, depending on the interaction among the adsorbates, preferential step adsorption might lead

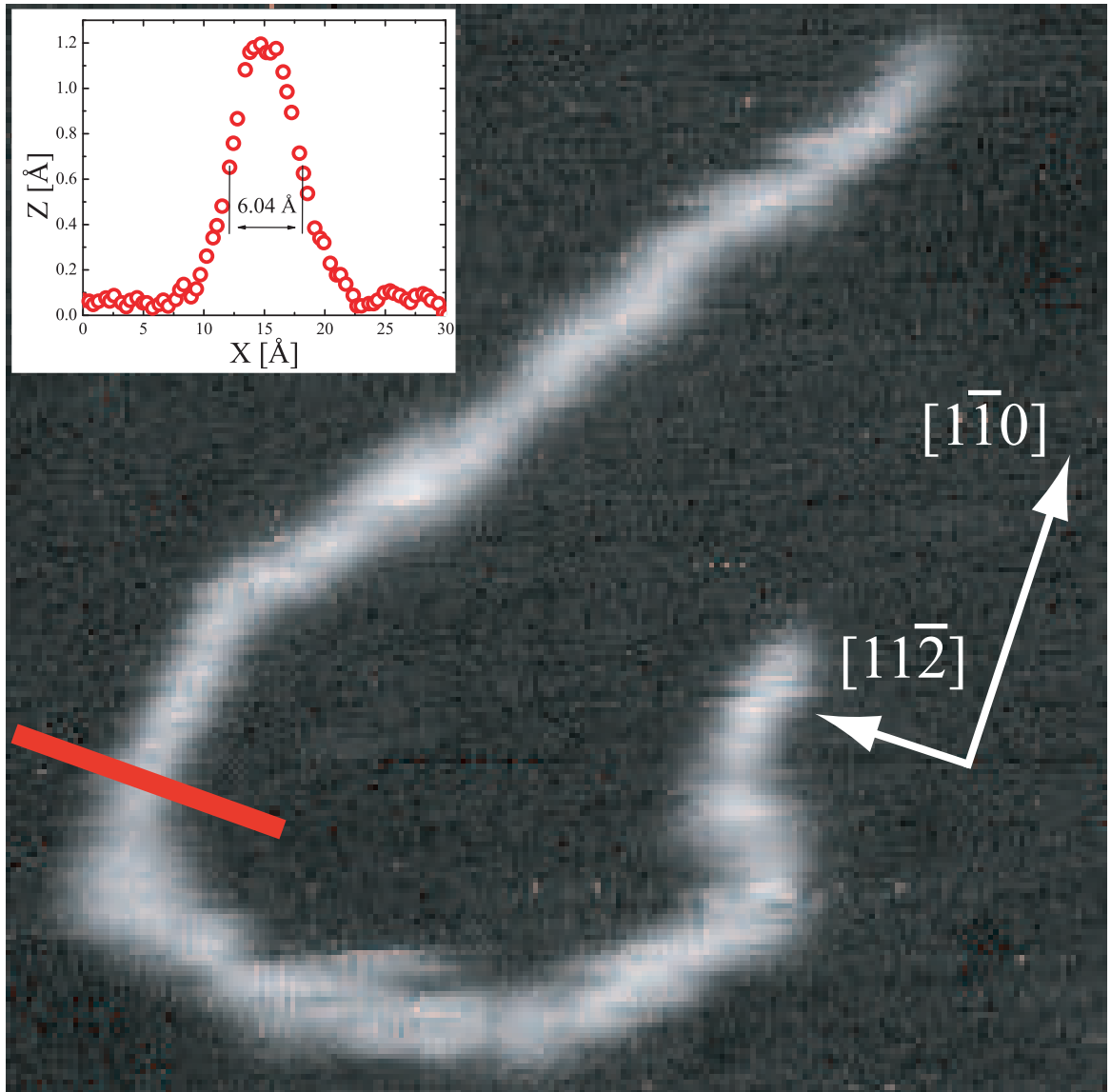


Fig. 2.13 – $125 \times 125 \text{ \AA}^2$, STM topographs of an Fe wire ($I_t = 0.2 \text{ nA}$, $V_t = -1.5 \text{ V}$). The $[1\bar{1}0]$ direction is deduced from the step direction of steps segments without kinks (not represented) after deposition of 0.01 ML Fe on Pt(111). The wire follows the crystallographic directions of the underlying Pt substrate. A linecut along the wire cross-section (red line) is shown in the inset.

to a rearrangement of the adatoms in favor of terrace sites in case repulsive interactions prevail over the extra binding energy provided by the steps [102]. Lundgren *et al.* claim that stress-driven nucleation processes might lead to wire or dendrite formation perpendicular to the step-edge [103]. Reconstruction lines along the dendrites in the Co/Pt(111) system are the signature of stress release through the formation of dislocations. Here, the absence of reconstruction lines along Fe wires supports the idea that the growth of wires in contact with the step-edge is governed by strong repulsive interactions among the Fe adatoms.

Microscopic description Fig. 2.13 is a $125 \times 125 \text{ \AA}^2$ high resolution image of an Fe nanowire on Pt(111) taken at a temperature of 220 K applying a tunnel current of $I_t = 0.2 \text{ nA}$ and a bias voltage of -1.5 V ($R_{gap} = 7.5 \times 10^9 \Omega$). The wire is $252 \pm 7 \text{ \AA}$ long corresponding to 91 ± 2.5 atoms assuming the pseudomorphical arrangement of Fe atoms on the Pt substrate [44, 57]. The wire follows the $[1\bar{1}0]$ crystallographic directions of the underlying Pt substrate with a kink in the direction every 3–7 atoms. The $[1\bar{1}0]$ directions refer to step-edge directions. Brighter and darker zones of the wires are the direct expression of local variations of the electronic structure. Brighter zones are sensibly remarked on the kinks and the ends of wires. Several research groups have reported on these "higher" zones at the ends of metallic monatomic wires [93–95]. They suggest the existence of one-dimensional delocalized electronic states. This implies that individual atoms in the wire cannot be resolved with the STM. Local impurities might also explain bumps along the wires [104].

The apparent height profile, shown in the inset, represents another example of monatomic wire width. The deconvolution method described for Fig. 2.11 could not be used here as no step-edge is present in Fig. 2.13. However, the wire cross-section reproduces very nicely the height profile shown in Fig. 2.11. In particular, the flat part on top is slightly smaller than 3 \AA while the FWHM is smaller than 8 \AA . The apparent height of the wire is around 1.2 \AA .

Wire mobility? At first sight, one could interpret the wire shape as the onset of a loop formation. Wire mobility has indeed already been reported on channelled surfaces such as Pt(110)-(1 \times 2) [105, 106]. However, concerted motion of monatomic wires was never reported on isotropic surfaces. This observation agrees with the following result : during our experiments we never observed wire mobility. Hence we will rule out the possibility of loop formation induced by wire mobility.

2.4.3 The effect of annealing on growth

A comparative analysis has been performed of the relative influence of the deposition and the annealing temperatures in order to identify the atomic processes involved in wire formation. This analysis is shown in Fig. 2.14. We present two samples each with a coverage of 0.01 ML of Fe on Pt(111). On the first sample, Fe atoms were deposited at 40 K where monomers are stable, then annealed at 220 K (**A**). On the second sample, Fe atoms were directly deposited at 220 K (**B**). In both cases, the sample was kept at 220 K during 10 minutes. This annealing duration ensures a total completion of the nucleation process. Fe wires were observed on both samples. A distinction was made between visible wires and smaller clusters, when the resolution was not sufficient to differentiate a compact cluster from a wire. The limit between these two populations is represented by a cluster surrounded by a red circle in the STM topographs. The boundary between the two populations was set for both samples, to a critical perimeter around $p_{cr} = 100 \text{ \AA}$. The wire density as well as the total cluster density was estimated over hundreds of clusters. One obtains for the total density $(4.2 \pm 1.0) \times 10^{-4}$ clusters/site and 5.5×10^{-4} clusters/site for **A** and

2.4. WIRE FORMATION, FROM 160 K TO 260 K

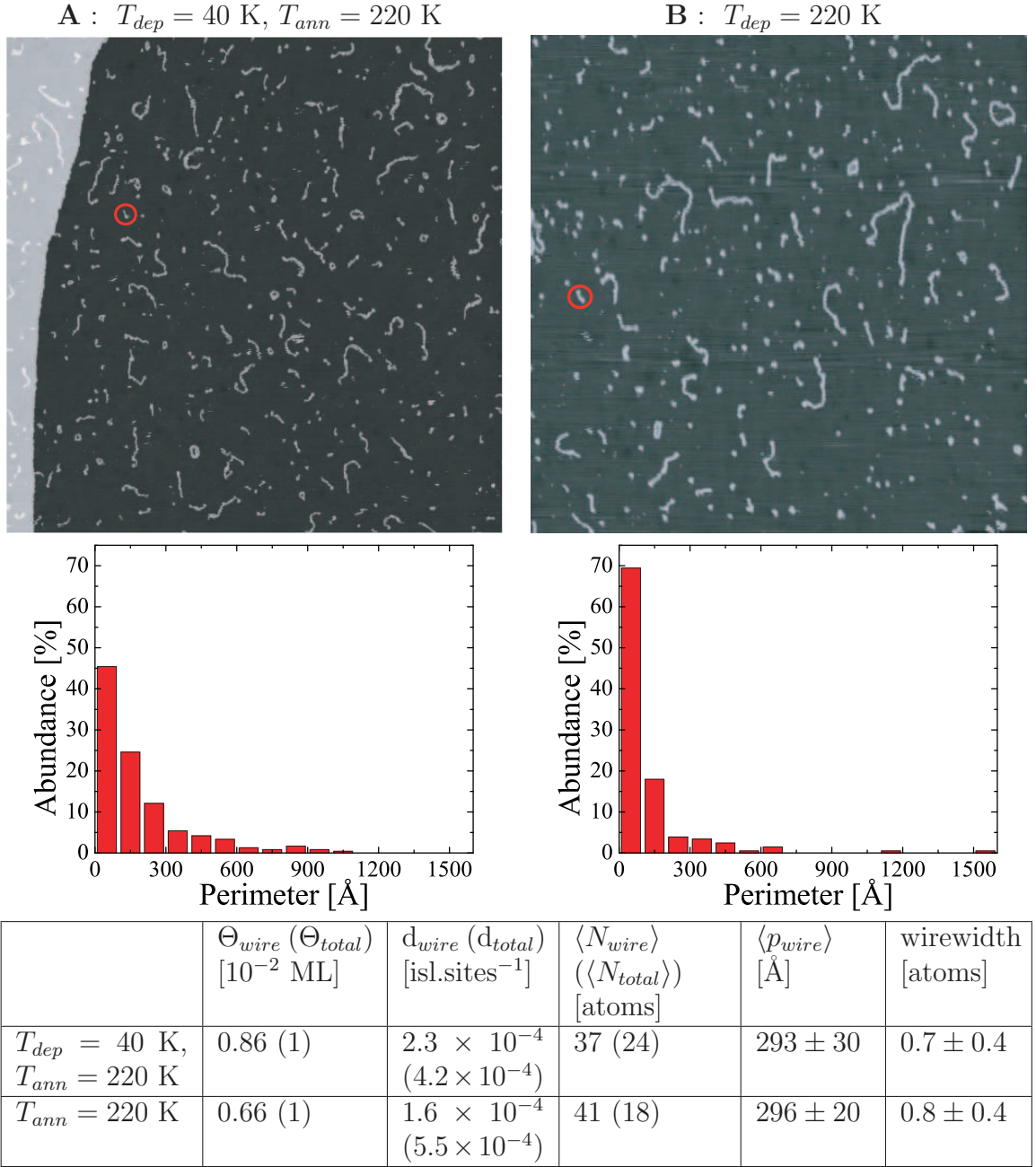


Fig. 2.14 – Comparison between two growth procedures **A** and **B** differing in the deposition temperature. (top) (left) $2500 \times 2500 \text{ \AA}^2$ and (right) $1800 \times 1950 \text{ \AA}^2$ STM topographs after the growth procedures **A** and **B**. The red circles show a critical size (around a perimeter of 100 \AA) between "visible" wires and smaller clusters. In both cases, Fe wires have a broad perimeter size distribution (center of the image). (bottom) Table of the relevant parameters. The wirewidth was estimated as the ratio of the mean wire length divided by the mean number of constituting atoms $\langle N_{wire} \rangle$, the mean wire length being half the perimeter.

B, respectively. This corresponds to a mean island size $\langle N_A \rangle = 24 \pm 7$ atoms and

$\langle N_B \rangle = 18 \pm 5.5$ atoms and is in good agreement with the previous series of results shown in Fig. 2.10.

On both samples, the average wire perimeter is around 295 Å with a broader distribution for **B**. The average size of the small clusters is estimated around 8 ± 1 atoms on both samples. In contrast, the ratio of "supposed" compact clusters and wires differs between **A** and **B**. Only 29% of Fe clusters are nanowires for **B** compared to 54% for **A**. This result has to be considered with care, since the data show large error bars due to the small number of islands used in the analysis (around 300 islands). The tendency to form more smaller clusters when the deposition temperature is high can be understood as follows. In sample **A**, wires are formed from existing clusters grown during the annealing procedure. The mean island size of these cluster is above 10 atoms. In sample **B**, wire formation occurs without pre-formation of clusters leading to the formation of smaller structures than in **A**.

Determination of the wirewidth from the analysis The density and the perimeter distribution of the wires were determined. The average length of the wires was estimated by defining it as half of the average perimeter. Assuming a pseudomorphical growth of the Fe wires on Pt, one finds the average wirewidth to be around 0.8 ± 0.4 Å. As expected these measurements slightly underestimate the wirewidth due to the tip convolution effect that induces an overestimation of the wire perimeter. The wire width is in excellent agreement with monatomic Fe wires. Other hypotheses on the wirelength assuming 2 atom width or 3 atom width could clearly be ruled out by the data analysis.

2.4.4 The effect of the coverage

In the following, the effect of the coverage on wire formation is discussed. Experimental results on two different systems illustrated the strong influence of coverage on the presence of the wires. The realization of Fe islands with controllable size and density is proved.

State of the art

Surface stress release Single crystal surfaces are under tensile stress due to missing bonds of the surface atoms. Surface stress is known to be strongly affected by deposition [107, 108] (and references therein). Moreover, at deposition temperatures which are far below the Pt melting point (2041 K), surface stress can be considered temperature-independent. A clean Pt(111) surface is under tensile stress [109]. Since bulk Fe and Pt have a large lattice mismatch of -10.6% , Fe adatoms release surface stress upon reaching a critical coverage.

What about surface diffusion? The effect of Pt relaxation on surface diffusion and nucleation has already been studied experimentally in the Ag/Pt(111) system [110]. It was shown that in general isotropic two-dimensional strain as well as

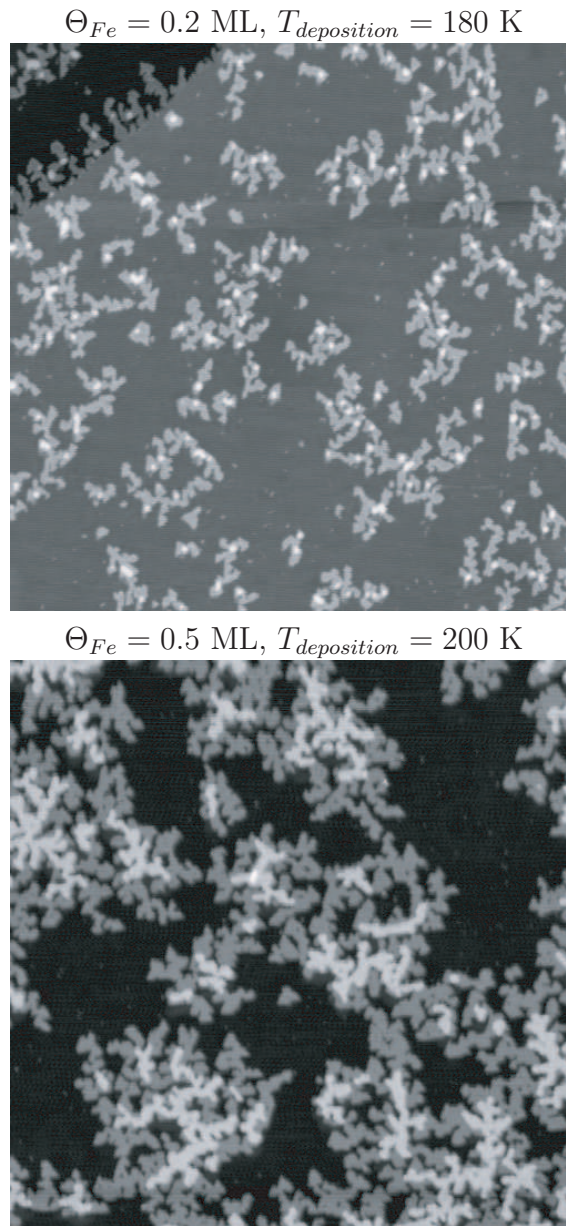


Fig. 2.15 – $1500 \times 1500 \text{ \AA}^2$ STM topographs of 0.2 ML of Fe deposited at 180K and 0.5 ML of Fe deposited at 200K. The growth of ramified islands of the first and the second Fe layer is observed. The presence of wires was barely detected.

its relief via dislocations have a drastic effect on surface diffusion and nucleation in heteroepitaxy. As already mentioned, a theoretical study of the exchange diffusion in the case Pt/Pt(111) and Co/Pt(111) [83] lays the emphasis on the strong influence of the surface tensile stress on the different kinds of diffusion processes via exchange between adatoms and atoms of the substrate. Experimental works on Co/Pt(111) [103, 111] confirm the key role played by surface relaxation on the nucleation of elongated structures. A discussion about this system is given in the section

devoted to the explanation of wire formation.

Fe films with $0.2 \text{ ML} \leq \Theta_{Fe} \leq 0.5 \text{ ML}$

Fe growth on Pt(111) and vicinal Pt(997) was previously studied by Repetto [112] and Lee [113]. Their works focused on Fe coverage higher than 0.7 ML but the morphology of 0.25 ML of Fe on Pt(111) growth at $T = 150 \text{ K}$ was also presented [114]. In all cases the presence of wires was never detected. To complete their study, we restricted ourself to coverages lower than 0.7 ML.

Fig. 2.15 shows topographs of samples with two different coverages, $\Theta_{Fe} = 0.20 \pm 0.02 \text{ ML}$ and $\Theta_{Fe} = 0.50 \pm 0.03 \text{ ML}$, deposited at 180 K and 200 K, respectively. For these two samples, Fe on top of the first Fe layer represents $\Theta_{Fe} = 0.010 \pm 0.005 \text{ ML}$ and $\Theta_{Fe} = 0.10 \pm 0.02 \text{ ML}$, respectively. Fe appears as ramified structures with elongated branches at low coverage. Fe on top of the first layer tends to form equally ramified structures. Such ramified structures were already observed on the system Fe/Pt(111) at $T = 150 \text{ K}$ with $\Theta_{Fe} = 0.25 \text{ ML}$ [114]. Ramified shapes are associated with low edge mobility and/or preferential adsorption at edge-sites [63] and therefore are generally present at low temperature. The presence of wires was barely detected even at the lowest coverage of 0.2 ML. This suggests that wires disappear at a critical coverage and, therefore, connects the formation of the Fe nanowires to surface stress.

Fe islands with $0.12 \text{ ML} \leq \Theta_{Fe} \leq 0.29 \text{ ML}$

In the following we report on the creation of Fe islands with controllable size and density. The total Fe coverage was between 0.12 ML and 0.29 ML. Furthermore, we report on the presence of wires in these samples as a function of the total coverage.

Two-step deposition : the way of making compact islands with controllable density The creation of Fe islands with controllable size and density was made by means of a two-step deposition (Fig. 2.16). A first deposition of $0.06 \pm 0.01 \text{ ML}$ of Fe at 150 K fixed the density of stable nuclei. The expected density value, determined using scaling law for stable dimer and the estimated energy barrier and attempt frequency for monomer diffusion is $1.4 \times 10^{-4} \text{ island/site}$ at 150 K. At 250 K, the mean free path of the Fe adatoms is higher than at 150 K. Therefore, subsequent deposition of Fe at 250 K predominantly increases the size of the existing islands. The second deposition at 250 K varies so as to adjust the desired coverage. Annealing tends to slightly decrease the island density, but the deposition of more materials slightly increases the island density. Experimentally, the density was measured on all samples to $(2.3 \pm 0.5) \times 10^{-4} \text{ island/site}$. This result is in excellent agreement with the expected density value estimated by means of the scaling law. This confirms the value used for the attempt frequency. It is worth noting that edge mobility also increases with temperature, therefore producing more compact islands after deposition at 250 K than at 180 K or 200 K.

2.4. WIRE FORMATION, FROM 160 K TO 260 K

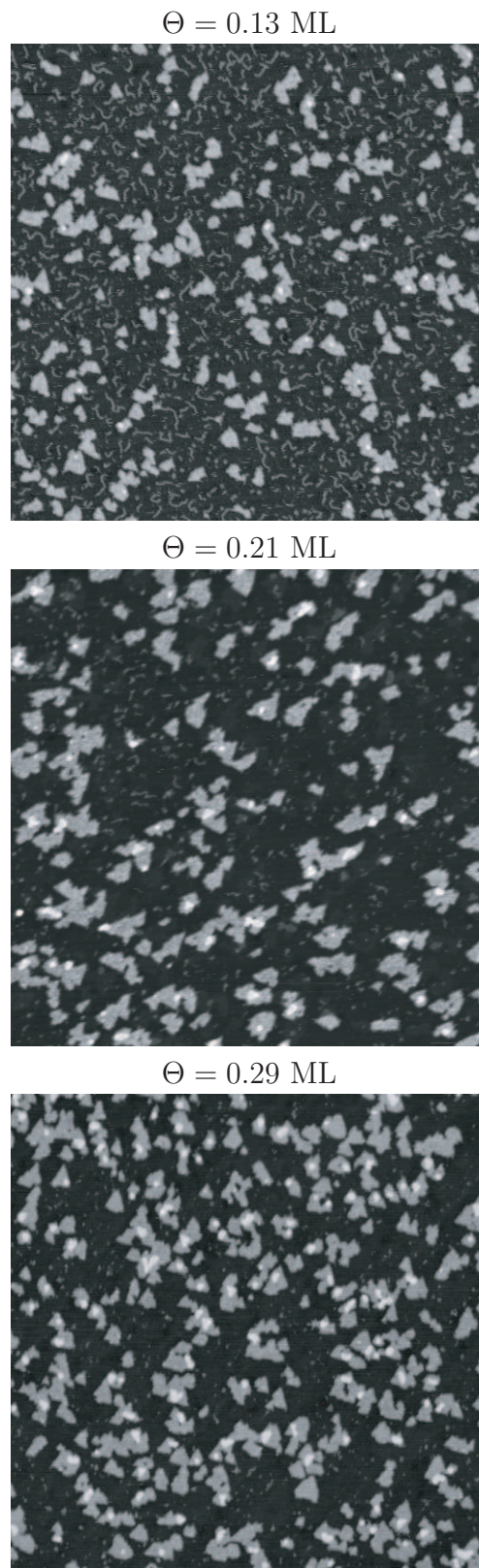


Fig. 2.16 – $2000 \times 2000 \text{ \AA}^2$ STM topographs of Fe islands grown on Pt(111) by a two-step growth procedure : 0.06 ML at $T_{dep} = 150 \text{ K}$, subsequent addition of further Fe at 250 K. The total coverage is 0.13 ML, 0.21 ML and 0.29 ML, from top to bottom. Wires are present at low coverage and disappear progressively.

Coverage dependent presence of the wires The presence of wires was observed in most of the two-step growth experiments presented in Fig. 2.16. These experiments showed that wire size and concentration strongly diminish around 0.14 ML and finally disappear at a coverage of 0.25 ML. The presence of wires has been seen not to influence the island density. This suggests that wires do not play a role in the growth of Fe islands on Pt(111).

Comparison between the two systems

One and two-step deposition of varying Fe coverage on Pt(111) have been studied by VT-STM at temperatures favoring the presence of Fe nanowires. In both cases, insertion and exchange of Fe with the surface atoms were not detected. This is in agreement with previous studies of Fe on Pt(111) [44, 114]. It implies that surface stress is released through the creation of bonds between adatoms and surface atoms. The onset of nucleation of the second layer on top of the islands of the first Fe layer is visible in both one- and two-step deposition. Around 0.01 ML of Fe is located on top of the first Fe layer when $\Theta = 0.20$ ML in both cases. The continuous growth of the second Fe layer with the total coverage contrasts with the abrupt variation of wire density. Therefore, we suggest that the two quantities are not correlated. We have observed a critical coverage around $\Theta_{Fe} = 0.25$ ML for the presence of wires in the two-step growth. The critical coverage in the one-step growth is lower than $\Theta_{Fe} = 0.20$ ML. We attribute this difference in critical coverage to a complicated relation between strain relief and island size and shape [115, 116]. These observations strongly suggest that the presence of wires is highly surface stress-dependent.

2.4.5 Above 260 K : back to Ostwald ripening

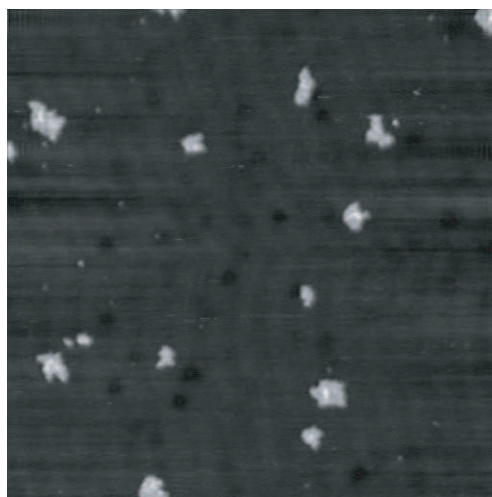


Fig. 2.17 – $1000 \times 1000 \text{ \AA}^2$ STM topograph of 0.0017 ML Fe grown at $T_{annealing} = 350 \text{ K}$.

In Fig. 2.17 a STM topograph is shown after ten minutes of annealing to 350 K.

We observe large, compact Fe clusters with $\langle s \rangle = 250 \pm 75$ atoms. No wires were observed over the whole surface. Since this experiment represents the highest annealing temperature studied, it was not possible to characterize sufficiently the growth regime following wire formation. Nevertheless, the large value of the mean island size strongly suggests Ostwald ripening.

Insertion and exchange? The absence of both insertion and exchange of the deposited atoms with the surface atoms are necessary conditions for Ostwald ripening. In the following, we discuss about the possibility of mixing between Fe adatoms and Pt atoms of the surface. Jerdev *et al.* have reported on the onset of Fe-Pt alloy formation around an Fe coverage of 0.65 ML at 350 K [55]. Other works on Fe/Pt(111) and vicinal Pt(997) report even higher alloying temperatures [45, 56] even though Fe and Pt exhibit a tendency for mixing, having a high segregation energy Fe/Pt : +0.37 eV/atom [117]. Lee *et al.* suggested that the alloying process is more efficient for Fe attached to Pt step-edge with respect to Fe on terrace sites or at the edges of Fe islands [45]. In our experiments, the insertion and/or exchange of Fe atoms with the Pt surface atoms could not be detected. Moreover, our samples regularly exhibit terraces wider than 1500 Å without tendency for increased island growth in the vicinity of step-edge. All together, this strongly supports that Fe and Pt do not mix at 350 K when the Fe coverage is about 0.01 ML.

2.4.6 Towards an explanation of the wire formation

The case of dendrite formation on Co/Pt(111)

The presence of nano-sized wires on Pt(111) has already been reported in the past on Co/Pt(111) [103, 111, 118]. Here, the nano-sized wires refer to the Co induced dendrites in conjunction with the local Co induced Pt double line reconstruction 2.18. In an atomic-scale study [103], Lundgren *et al.* proved that Pt double line reconstruction was due to incorporation of Co atoms in the topmost Pt layer. The double line reconstructions were associated to partial dislocations between the first and the second layer. Lundgren *et al.* demonstrated that the formation of the dendrites that accompanies the Pt reconstruction lifted the double line reconstruction. Furthermore, by combining the use of Low Energy Ion Spectroscopy and STM, the authors showed that the dendrites consist mainly of Pt. The measurements indicated that Co is incorporated and growing underneath the topmost Pt layer in the dendrite.

This case is interesting since it deals with the same substrate and with an element very similar in properties as Fe. The lattice mismatch between bulk Fe and Pt (-10.6%) is, indeed, very similar to the one between bulk Co and Pt (-9.4%). Nevertheless, a dislocation induced dendrite formation must be excluded in case of Fe wire formation on Pt(111) for the following reasons :

- Dislocations are straight lines upon relatively long distances, e.g. larger than 2000 Å as it is observed in Fig. 2.18, whereas our Fe wires are usually smaller than 200 Å and can be seen as curved lines.

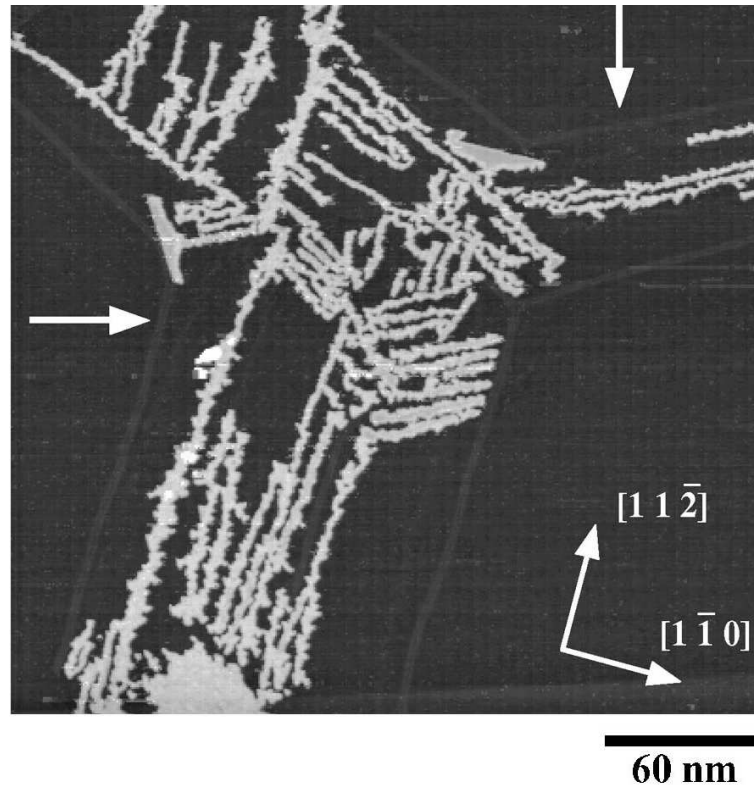


Fig. 2.18 – $3000 \times 3000 \text{ \AA}^2$ STM topographs of 0.1 ML Co deposited on Pt(111) at 400 K showing the Co induced double line reconstructions (marked by arrows) and dendrites (bright areas) on the Pt(111) surface [103].

- Co induced dendrites are few atom wide whereas our Fe wires are monatomic.
- No Fe incorporation and no reconstruction lines were observed on STM images.

For all these reasons, we exclude Pt wire formation induced by Fe incorporation in the Pt(111) surface.

Possible mechanisms

From the previous results, one can already attribute wire formation to two non-exclusive mechanisms. First the enhancement of edge-mobility towards wire ends. Secondly the wire formation driven by long-range adsorbate-adsorbate interactions. Such mechanisms were proposed by Koh and Ehrlich [119] to explain the formation of one-dimensional (1D) Ir and Pd wires on the anisotropic W(110) surface around $T = 360 \text{ K}$ (see Fig. 2.19 (a) and (b)). The authors performed Field Ion Microscopy to track single atoms approaching and finally incorporating into existing wires. On Fig. 2.19 (b) the trajectory of an Ir atom before to incorporate the wire end is presented. The displacements of the Ir atom are driven by highly anisotropic, long-ranged interactions between Ir atoms. In the case of Pd, the authors claim that edge mobility towards wire ends was equally observed. Fig. 2.19 (c) shows calculations for Co atoms arranged in a close-packed wire on Cu(111) [73]. The diffusion of an adatom

2.4. WIRE FORMATION, FROM 160 K TO 260 K

along the wire has an energy barrier of 35-40 meV, comparable to the diffusion of an adatom on the free terrace. A perpendicular approach of the wire by an atom costs 110 meV, while an attachment to its end has a barrier of only 80 meV.

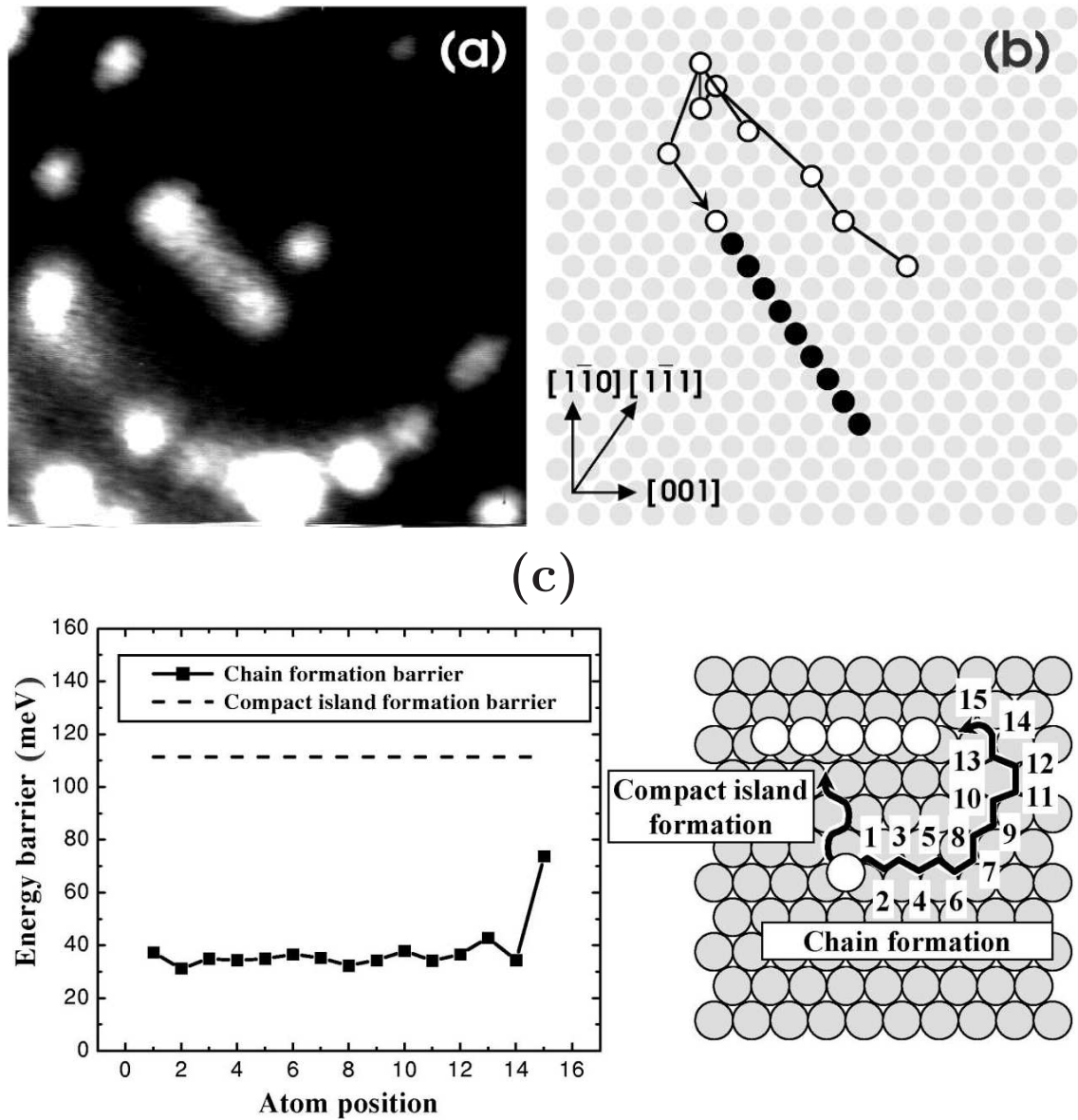


Fig. 2.19 – (a) FIM image of a monatomic Ir-wire with one Ir atom close by. (b) The trajectory (350 K, 5 s) shows that the Ir atom attaches to the wire end and avoids approaching the wire from the side $[11\bar{9}]$. (c) Atomistic calculations, based on the pair interaction potential calculated with *ab-initio*-methods, show that Co wires on Cu(111) have an attachment barrier of 110 meV for Co atoms coming from the side, whereas attachment to the end has only a slightly higher barrier than terrace diffusion along the wire [73].

2.5 Conclusion

Nucleation and growth of Fe clusters on Pt(111) at low coverage has been studied by means of nucleation curves and STM analysis. A model is proposed in order to describe the nucleation behavior. The results were compared to existing nucleation models. It was shown that the nucleation process is strongly temperature-dependent. Until 130 K, nucleation is driven by pure diffusion processes. A fit of the experimental results with RE model allows one to determine the activation energies for the diffusion of monomers ($E_{m1} = 190 \pm 10$ meV, $\nu_0 = 5 \times 10^{13}$ Hz), dimers, trimers and possibly tetramers ($E_{m2} = E_{m3} = E_{m4} = 290 \pm 10$ meV, $\nu'_0 = 5 \times 10^{13}$ Hz). Between 130 K and 160 K, a continuous increase of the average cluster size strongly supports the onset of Ostwald ripening. Between 160 K and 260 K, the population of Fe clusters can be divided into compact clusters and 1D monatomic wires. Surface stress play a role in the presence of wires on the Pt(111) surface. A probable mechanism for their formation is explained by the interplay of long-range interactions between adsorbates leading to Fe migration toward the wire end. At a temperature of 350 K, the nanowire density collapses to the benefit of some more thermodynamically favorable compact clusters. The formation of 1D monatomic wires on the isotropic Pt(111) substrate opens the door to a wide range of new experiments in order to gain deeper knowledge on surface diffusion processes and access to a better understanding of one dimensional structures. As an example of a possible application, the realization of self-assembled Fe quantum corrals [120] should allow give insight on the microscopic origin of the magnetic anisotropy energy of two coordinated atoms.

We demonstrated experimentally that it is possible to tailor the size and density of compact islands by means of a two-step deposition. It was observed that Fe wires do not influence the density of large stable clusters.

Mechanisms of magnetization reversal : from coherent rotation to nucleation and domain wall motion

3

The mechanism of magnetization reversal that occurs during a magnetization curve of a bulk ferromagnet is generally ascribed to domain-wall motion after nucleation in the early stage of magnetization and to a coherent tilt of the magnetization near the saturation [121]. In 2D nanostructures, the mechanism of thermally activated magnetization reversal is still a non-trivial issue due to the difficulty to characterize the transition state of the island either experimentally or theoretically.

The aim of this chapter is to provide the necessary tools to understand the key parameters of magnetization reversal of one monolayer thick Co nanostructures on Pt(111). A description of the mechanisms associated with coherent rotation and with nucleation of domains and domain-wall motion is given. Then, the peculiar properties associated with complex shapes of the nanostructures are discussed, revealing the strong shape dependence of the mechanism of magnetization reversal.

The rest of the chapter is dedicated to a study of the system of one monolayer thick Co nanoparticles on Pt(111) by means of the complementary use of VT-STM and MOKE. Different models are compared, including models for the Curie temperature and the distribution of anisotropy. Altogether, our results highlight the strong size and shape dependence of the magnetization reversal process.

3.1 Length scales

The intrinsic magnetic properties such as the spontaneous magnetization M_s , the first uniaxial anisotropy constant K_1 and the exchange stiffness A are determined by

atomic-scale effects. However, up to a certain extent, most variations become rather unimportant on length scales larger than about 10 Å, and to a good approximation we can consider these quantities as continuous.

The different contributions to the rotation of the magnetization are summarized by the energy functional :

$$E = \int \left(A \left[\nabla \left(\frac{\mathbf{M}}{M_s} \right) \right]^2 - K_1 \frac{(\mathbf{n} \cdot \mathbf{M})^2}{M_s^2} - \mu_0 \mathbf{M} \cdot \mathbf{H} - \frac{\mu_0}{2} \mathbf{M} \cdot \mathbf{H}_d(\mathbf{M}) \right) dV \quad (3.1)$$

where $\mathbf{M}(r)$ is the local magnetization, $\mathbf{n}(r)$ is the unit vector of the local anisotropy direction, \mathbf{H} is the external or Zeeman field and

$$\mathbf{H}_d(r) = \frac{1}{4\pi} \int \frac{3(r - r')(r - r') \cdot \mathbf{M}(r') - |r - r'|^2 \mathbf{M}(r')}{|r - r'|^5} dV' \quad (3.2)$$

is the free magnetostatic self-interaction field, sometimes referred to as shape anisotropy. Equation 3.1 is also known as the micromagnetic *free* energy, indicating that A , K_1 , \mathbf{n} and M_s are temperature-dependent equilibrium quantities which can, in principle, be determined from an atomic scale partition function. It is important to note that $\mathbf{H}_d(r)$ is uniform only for samples shaped as infinite flat surfaces with uniform magnetization. For any other type of shape $\mathbf{H}_d(r)$ is not uniform for whatever high value of the applied field. The non-uniformity is especially strong in the case of thin and flat structures. Such shapes exhibit a local magnitude which can be considerably higher than the overall average value. This is especially the case close to the edges.

The ∇ term in Eq. 3.1 means that the exchange is treated on a continuum level. This approximation ignores the small exchange anisotropic contributions with respect to the bond and magnetization direction \mathbf{M}/M_s . The exchange energy A depends on the island thickness. Typical values are between 1-20 meV/atom [122]. As an example, $A = 5 \times 10^{-12}$ J/m = 8 meV/atom was measured for an 8-ML thick film [123]. We assume that the value could be smaller for 1 ML [124, 125].

For thin films, especially in the case of one monolayer thick films, the first uniaxial anisotropy constant K_1 refers to the superposition of the crystalline and the magnetoelastic anisotropy. A rigorous view of the surface anisotropy was given by Bruno [126] and Van der Laan [127]. They predicted that the anisotropy of the angular momentum is proportional to the magnetocrystalline anisotropy constants. Experimentally, a strong dependence of K_1 with the local dimensionality was equally observed by Rusponi *et al.* [128] on nanoislands of Co on Pt(111) down to the atomic scale [34].

It has been shown that the magnetoelastic contribution is non-linear with the z -axis of a thin plane [129–133]. It is both experimentally and conceptually difficult to separate the magnetoelastic contribution from the surface anisotropy. Therefore, K_1 will refer to an effective anisotropy constant K .

3.1. LENGTH SCALES

The minimization of the energy functional in Eq. 3.1 in respect to the magnetization vector allows one to determine the equilibrium magnetization state which corresponds either to a single-domain or a multi-domain. On the contrary, the variation of the magnetization vector as a function of the magnetic field reflects the non-equilibrium magnetization reversal processes caused by energy barriers. These processes are known as *coherent rotation*, *nucleation and Domain-Wall motion* and *incoherent reversal by curling or vortex formation*.

The competition between two (or more) interaction energies gives rise to characteristic magnetic lengths, namely

the domain-wall width

$$\delta = \sqrt{A/K} \quad (3.3)$$

and the exchange length

$$l_{ex} = \sqrt{\frac{A}{\frac{\mu_0}{2} M_s^2}}. \quad (3.4)$$

These lengths are precise indicators of the magnetization state and the mechanism of magnetization reversal in the nanomagnet.

Domain wall width

δ determines the thickness of the domain-wall. It represents the separation between the magnetic domains of different magnetization directions and the spatial response of the magnetization to local perturbations [134]. The thickness of a domain-wall is the result of the interplay between the exchange energy, which favors smooth walls, and anisotropy energy, which favors narrow transition regions and is then expected to be proportional to δ . The minimization of the total energy of a 180° Bloch wall yields to the typical value of domain wall energy per unit surface of wall $\gamma = 4\sqrt{AK}$. Two competitive energies are responsible for the creation of a domain-wall. On one hand, the magnetostatic energy favors a flux closure by creation of domains, on the other hand, the domain-wall energy wants to be minimized. A critical single-domain radius can be inferred. This radius is strongly geometry-dependent [135, 136]. In nanostructures it is frequent to consider only δ as the critical single-domain radius.

Exchange length

The exchange length reflects the competition between the exchange, which favors parallel magnetic moments, and the magnetostatic term, which favors flux closure. It determines, for example, the transition from coherent rotation to curling. From bulk values of A and M_s , one can predict that the transition occurs for dimensions of the order of 100 Å for common materials like Fe and Co. This value must be considered carefully as other aspects such as geometry, dimensionality and local inhomogeneities play an important role. Another prediction based on a scaling analysis made by

Skomski sustains that a perpendicular magnetized one monolayer thick Co film could reach critical length as high as 4000 Å [136]. The authors emphasize the difficulty to prove this value experimentally. Since the nanostructures that will be considered in this and the following chapter have typical dimensions inferior or equal to 100 Å, this mode will be ignored.

3.2 Theoretical models of magnetization reversal : coherent rotation vs. nucleation and domain-wall motion

In this section, I briefly describe the main features of the mechanism of magnetization reversal by *coherent rotation* and *nucleation and domain-wall motion*. I will focus on the determination of zero-field susceptibility curves for both mechanisms in the case of nanometer-size magnetic particles.

3.2.1 Coherent rotation : the macrospin model

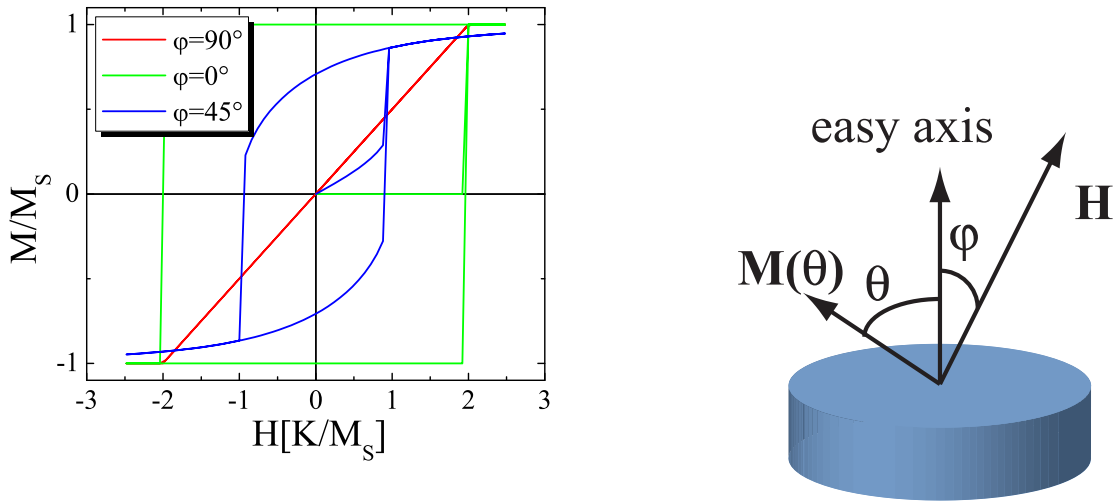


Fig. 3.1 – (left) Magnetization curves when only coherent rotation is responsible for the magnetization reversal. The angle refers to the direction of the applied field with respect to the easy axis direction as indicated on the right. M refers to the projection of the magnetization $\mathbf{M}(\theta)$ on the applied field direction. (parameters : $T = 10^{-3}$ K, $\nu_0 = 10^{10}$ s $^{-1}$, field rate : 0.8 T.min $^{-1}$). (right) Representation of the macrospin $\mathbf{M}(\theta)$ in the coherent rotation process when the easy axis of magnetization lies perpendicular to the sample plane.

Coherent rotation is also known as *uniform rotation* or *Stoner Wohlfarth model*.

3.2. THEORETICAL MODELS OF MAGNETIZATION REVERSAL : COHERENT ROTATION VS. NUCLEATION AND DOMAIN-WALL MOTION

This mechanism of magnetization reversal is associated to a synchronized rotation of all magnetic moments over the entire magnetic structure. Typically, this model is used to describe the magnetic properties of an ensemble of small magnetic particles. Thus, the magnetic moments of each particle are assimilated to a unique "macrospin" rotating with an angle θ with respect to the easy axis of magnetization. This requires that the dimensions of the magnetic structure are inferior to the critical single-domain radius. Since this radius is strongly geometry-dependent [137, 138], one will prefer to refer to a multiple of the domain-wall width. In the case of materials with a high K_u such as those used in our experiments, the critical domain formation length is around 100-300 Å [139].

The energy of single-domain particle with uniaxial anisotropy yields :

$$E = K_v \cos^2(\theta) - \mathbf{H} \cdot \mathbf{M}_v \cos(\theta + \phi) \quad (3.5)$$

where $K_v = KV$ takes into account the magnetic anisotropy energy(MAE) and the magnetostatic energy of the particle of volume V , $\mathbf{H} \cdot \mathbf{M}_v \cos(\theta + \phi)$ is the Zeeman energy with \mathbf{M}_v being the macrospin vector and \mathbf{H} the external field (see Fig. 3.1) and $\theta + \phi$ is the angle between \mathbf{H} and \mathbf{M}_v . Local minima corresponding to the *up* and *down* orientations of \mathbf{M}_v are separated by energy barriers E_{b_i} (i refers to the local minimum). Independently on the details of the landscape shape of the energy barrier, the thermal activated magnetization reversal rate follows the Arrhenius law $\nu = \nu_0 \exp(-E_{b_i}/k_B T)$, with $\nu_0 = 10^{-10} \text{ s}^{-1}$ [140]. The barrier is readily overcome if $T > T_B = E_b/(k_B \ln(\nu_0/\omega))$, where ω is related to the observation time $t = \pi/\omega$. In zero-field susceptibility measurements, ω is the sweep frequency of the external magnetic field. T_B is the blocking temperature, defined by the temperature where the ensemble reaches half of its thermodynamic equilibrium susceptibility χ_{eq} . For $T > T_B$, the particles are superparamagnetic, and $\chi(T) = \chi_{eq}(T)$. This is true as long as the Curie temperature T_C is not reached. T_C is defined as the temperature at which thermal excitations break the parallel alignment of the magnetic moments inside the particles. For $T < T_B$, the particles are blocked in a fixed magnetization state (*up* or *down*), and hence $\chi(T) = 0$. For $T \approx T_B$, the system is determined by the kinetics of barrier crossing which depend on the actual shape of the energy barrier.

The rather simple form of the expression for coherent rotation allows one to derive an analytical solution for the magnetization curves $M(H)$ ($M(H)$ is the projection of \mathbf{M} in the direction of the applied field, see Fig. 3.1). In the case of a field applied along the easy axis, the expected temperature-dependence of the coercivity is

$$H_C(T) = H_C(T = 0 \text{ K}) \left(1 - \sqrt{\frac{k_B T}{K_v} \ln \frac{\tau}{\tau_0}} \right) \quad (3.6)$$

where τ is the time duration of the overall measurement.

Moreover, this model allows the determination of an exact solution for the in-phase (real) and out-of-phase (imaginary) part of the zero-field susceptibility ($\chi = \chi_1 + i\chi_2$) :

$$\chi_1(\omega, T) = \chi_{eq}(T) \frac{1}{1 + \omega^2 \tau^2} \quad (3.7)$$

$$\chi_2(\omega, T) = \chi_{eq}(T) \frac{\omega \tau}{1 + \omega^2 \tau^2} \quad (3.8)$$

$$(3.9)$$

where $\tau = 1/\nu_0 \exp(K_v/k_B T)$ [128], K_v being the energy barrier. χ_{eq} is the zero-field susceptibility at thermodynamic equilibrium given by [141, 142]

$$\chi_{eq}(T) = M^2 \left[\frac{\exp(K_v/k_B T)}{\sqrt{\pi K_v k_B T} \operatorname{Erfi}(\sqrt{K_v/k_B T})} - \frac{1}{2K_v} \right] \quad (3.10)$$

where $\operatorname{Erfi}(x) = (2/\sqrt{\pi}) \int_0^x e^{t^2} dt$ is the imaginary error function.

This equation takes into account the fluctuations of the magnetization around the energy minima. The blocking temperature T_B is defined by $\omega \tau(T_B) = 1$. In practice, T_B will refer to the temperature corresponding to the peak of the $\chi_2(T)$ curves. The transition width in our experiment is given by $\Delta T_B = k_B T_B^2 / K_v \approx T_B / 30$. The kinetics of barrier crossing (activation region) is reflected in a peak both in the $\chi_1(T)$ and in the $\chi_2(T)$ curves. Fig. 3.2 shows the infinite anisotropy limit, leading to a two-state system (Ising model), and the vanishing anisotropy limit, characterized by an occupation of all orientations of \mathbf{M} (Langevin model). With increasing temperature, χ_{eq} goes from one limit to the other and therefore its decay is slightly steeper than the $1/T$ behavior characterizing the two limiting cases $\chi_{Ising} = \frac{\mu_0 M_v^2}{k_B T}$ and $\chi_{Langevin} = \chi_{Ising} / 3$. Therefore, the Ising model is a good approximation for $\chi_{eq}(T)$ if $T_B < T < 2T_B$ whereas the Langevin model can only be used for very high temperatures [142].

The macrospin model remains idealistic for the majority of nanostructures. The inhomogeneity of the magnetostatic field, especially on the edge of the nanostructures induces misalignment of the magnetic moments. The single-domain state is then called by the name given to its magnetic configuration, *e.g.* flower, leaf, S-shape, C-shape [143]. A non uniform distribution of anisotropy may also induce some differences to the macrospin model [144].

3.2.2 Nucleation and domain wall motion

The concept of magnetic domains was proposed for the first time by Weiss in 1907. In 1935 the magnetostatic energy was added to this concept by Landau and Lifshitz [146]. Later a number of other models were developed [147–151]. In 1990, domains were finally observed experimentally by Pommier during the reversal process on ultra thin Co film on Au(111) with perpendicular anisotropy [152] and independently by Allenspach using the new SEMPA technique [145] (Fig. 3.3). In the last ten years, the development of micromagnetic simulations and new experimental techniques, *e.g.* micro-SQUID [153] or SP-STM [154] or improvement of known techniques as Photo Emission Electron Microscopy [155] has given new insights towards a microscopic

3.2. THEORETICAL MODELS OF MAGNETIZATION REVERSAL : COHERENT ROTATION VS. NUCLEATION AND DOMAIN-WALL MOTION

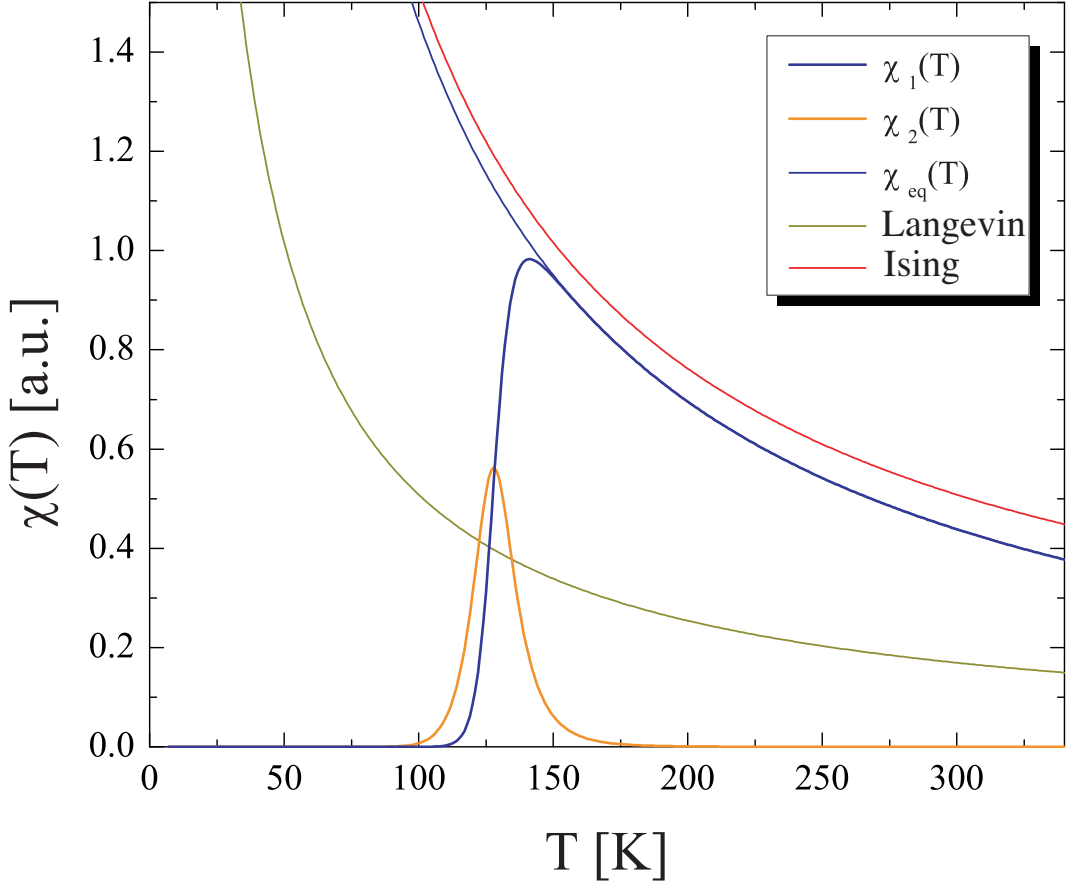


Fig. 3.2 – Zero-field magnetic susceptibility $\chi(T)$ for an ensemble of monodisperse, uniaxial particles. Different models are compared for $K_v = 200$ meV, $M = 1500$ atoms $\times 2.1 \mu_B = 182$ meV $\cdot T^{-1}$, triangular field sweep with $\omega = 0.3$ Hz. The real $\chi_1(T)$, imaginary $\chi_2(T)$ and equilibrium $\chi_{eq}(T)$ zero-field susceptibility (thick blue, orange and thin dark blue curves, respectively) corresponds to the analytical model of coherent rotation. The Ising model (two states : up and down) and the Langevin model (continuum of states, no anisotropy) are represented (thin olive and red curves, respectively) are shown for comparison.

understanding of the mechanism of magnetization reversal. Nevertheless, one of the main technological goals remains to identify and control the magnetization reversal process. The reproducibility of the reversal process ensures a constant coercive field and thus allows one to reduce the hysteresis loss during a "writing" process. A general introduction on magnetic domains is beyond the scope of this section and should be found elsewhere [135, 153, 156, 157]. The aim of this section is to briefly introduce the key parameters in the magnetization reversal process including magnetic domains.

From a thermodynamic point of view, domain-walls are the consequence of the competition between anisotropy, exchange and magnetostatic energy. However, they may equally occur during magnetization reversal through complex nucleation and propagation mechanisms [158–160]. In ultrathin nanometer-sized magnets with perpendicular anisotropy, usually Bloch walls and Néel walls can be observed. Bloch wall

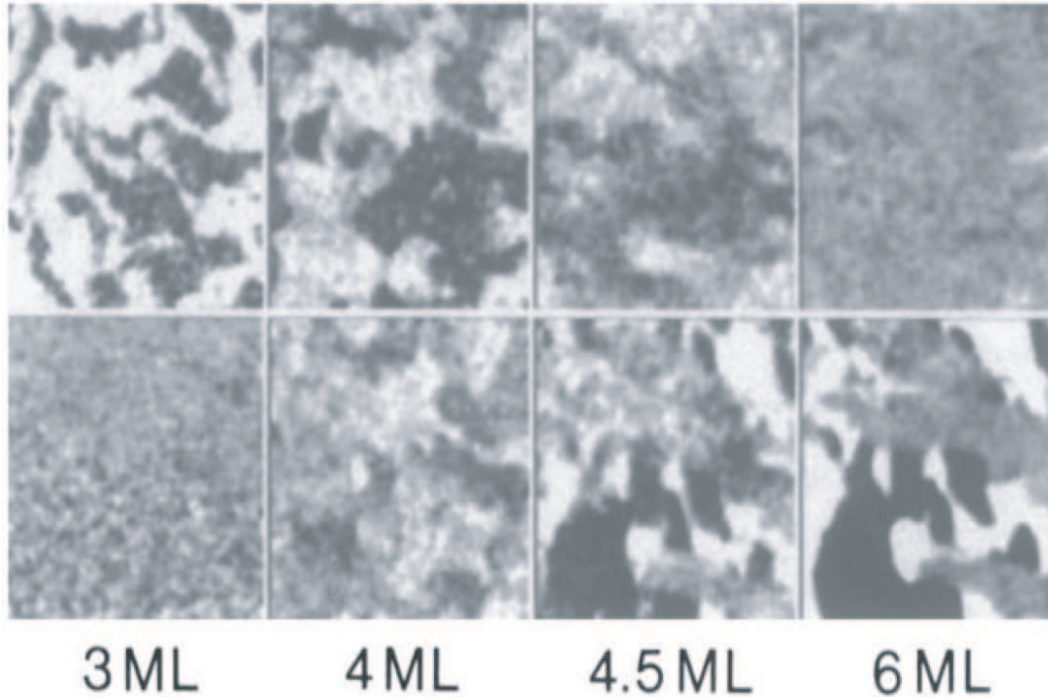


Fig. 3.3 – *Magnetic domain images by SEMPA for Co/Au(111) thin films, showing the evolution of domain size and switching behavior vs. film thickness. The images have been taken at identical positions on the sample (within 2% of scan area) between evaporation of additional layers. For each thickness, the upper image gives the out-of-plane and the lower the in-plane magnetization component. Gray scales from black to white indicates magnitude of magnetization component along the measured axis; scan area $20 \mu\text{m} \times 20 \mu\text{m}$. Note the collapse of the small domains on proceeding from 3 to 4 ML [145].*

refers to domain-wall with rotation of the magnetization in the plane of the wall. Néel wall refers to the domain-wall with a rotation of the magnetization perpendicular to the plane of the wall. It was shown that in the case of small enough wire transverse dimensions, Bloch wall model can be adapted to these structures, even if they are not at all Bloch walls [161].

It is important to distinguish between domain nucleation and domain-wall pinning. Nucleation-controlled magnets are, ideally, defect- and domain-free. Their coercivity field is essentially given by the nucleation field. In contrast, pinning-type magnets contain pronounced inhomogeneities, which ensure coercivity by impeding the motion of the domain walls. The sources of inhomogeneities are numerous in the case of nanostructures and ultra thin films. They are assigned to constriction effect in the branches of the nanostructures, alloying, kinks, atoms in second layer, structural defects, impurities (CO or H₂O contamination) and position dependent tensile stress.

Independently of the sources of inhomogeneities, models have been proposed to describe the magnetic extrinsic properties when magnetization reversal is governed by nucleation and domain-wall motion [148, 162, 163]. Motion is here a general term

3.2. THEORETICAL MODELS OF MAGNETIZATION REVERSAL : COHERENT ROTATION VS. NUCLEATION AND DOMAIN-WALL MOTION

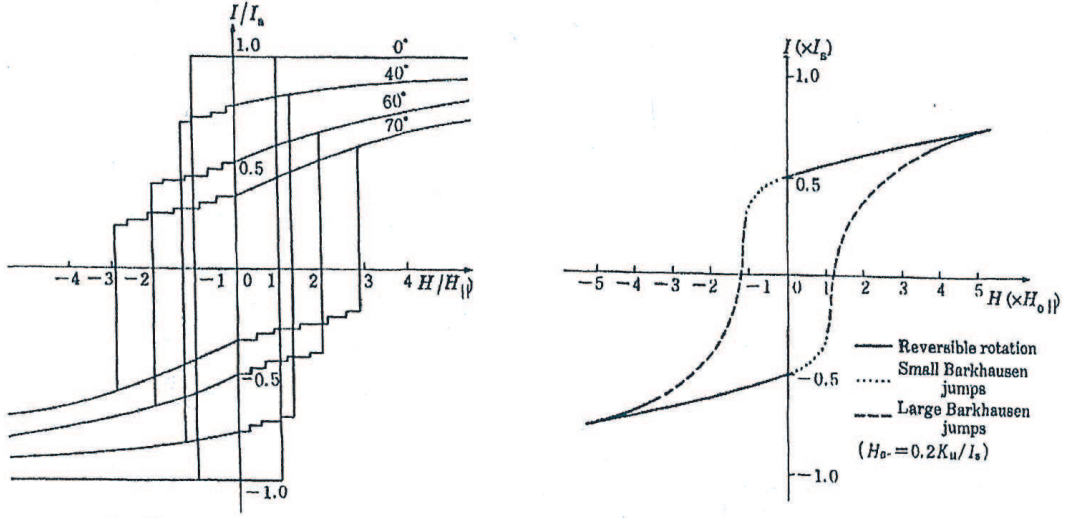


Fig. 3.4 – Magnetization curves when domain-wall motion is only responsible for magnetization reversal. (left) The angle refers to the direction of the applied field with respect to the easy axis direction of oriented domains. (right) Magnetization curve averaged on all orientations [121].

associating bowing and translation. Some studies focused on the determination of the magnetic domain-wall velocity as a function of an applied external field [164] in order to deduce the magnetization curves [165]. Phenomenological models have also been proposed to describe the influence of pinning on magnetic extrinsic properties [151, 166]. A study of the zero-field susceptibility can also be found elsewhere [167, 168]. In these works, the temperature dependence of χ is not revealed. An example of magnetization curves is given in Fig. 3.4 where domain-wall motion is the only mechanism of magnetization reversal.

One general approach is based on the phenomenological expression of the coercive field.

$$H_C(T) = H_C(T = 0 \text{ K}) \left(1 - \left(\frac{k_B T}{K V_n} \ln \frac{\tau}{\tau_0} \right)^{1/m} \right) \quad (3.11)$$

where V_n is the so-called *nucleation volume*, closely related to the switching volume of the magnet and m a phenomenological exponent often found between 1 and 2. They both have to be determined experimentally. However, the value 3/2 is actually quite common and it is noticeable to remark that this value is associated to strong domain-wall pinning [151] and misalignment between the field and the easy axis in the coherent rotation process [169, 170].

3.3 Shape-dependent effect on the mechanism of magnetization reversal

It has been seen that the shape of a nanostructure may influence strongly the mechanism of magnetization reversal by increasing pinning of the domain wall with constriction zones [171, 172] and edge effects or by altering the macrospin model thanks to variation of $\mathbf{H}_d(r)$ or a distribution of anisotropy through the nanostructure [144]. In this section, I will focus on two main characteristics of the nanostructures mentioned in this manuscript, namely their aspect ratio and their inhomogeneous distribution of anisotropy. Since we have built both ramified and compact nanostructures, it was important to compare the mechanism of magnetization reversal of both shapes.

The thermally activated magnetization reversal by domain-wall nucleation and displacement was theoretically investigated by Braun for the 1D problem, or equivalently for elongated particles (particles with in-plane aspect ratio larger than 1 : 10) [158, 173, 174]. Braun demonstrated that the excitation (or nucleus) with the lowest energy is an untwisted domain-wall pair and, once this nucleus has formed, the magnetization can reverse without further expense in energy. The nucleation barrier is proportional to the particle vertical cross-section S_z and in the limit of small field ($H < 2K/M$) reads $E_{DW} = 8S_z\sqrt{AK}$, where K includes contributions of crystalline and shape anisotropies. One defines a critical length L_{cr} by comparing the previous energy with the energy required for the coherent magnetization rotation, which, for a uniform distribution of anisotropy, reads $E_{CR} = S_zL_{cr}K$, giving $L_{cr} = 8\sqrt{A/K}$. Actually, for very elongated particles $L \gg L_{cr}$, the particle ends behave independently and at finite-temperature, due to the thermal fluctuations, magnetization reversal by nucleation of a reversed domain at one particle end becomes energetically favorable [175–177]. In this case, the nucleation barrier $E_{DW} = 4S_z\sqrt{AK}$ is half the value calculated for the untwisted domain-wall pair case and the critical length reads $L_{cr} = 4\sqrt{A/K}$ and $L_{cr} \approx 5\sqrt{A/\mu_0M^2}$ for the two limit cases of $\mu_0M^2 \ll K$ [175] and $\mu_0M^2 \gg K$ [178], respectively.

Experimental evidence of a shape-dependent switching behavior has been reported for one monolayer thick perpendicularly magnetized Fe islands on Mo(110) (see Fig. 3.5). Spin polarized-STM measurements (SP-STM) recording thermal switching rates of individual islands containing some hundreds atoms suggested that elongated particles (with a maximum aspect ratio of 1 : 4) switch faster than equally sized compact islands [124]. Bode *et al.* deduced $K = 0.096^{+0.010}_{-0.021}$ meV/atom and $\nu_0 = 4 \times 10^{10}$ s⁻¹ from measurements of the switching rate of compact islands at two different temperatures (13 K and 19 K). They report a critical length of $L_{cr} = 91 \pm 3$ Å and a wall-width of 29 ± 1 Å giving $A = 3.9^{+0.9}_{-1.2}$ meV/atom. The islands shorter than L_{cr} reverse coherently while the islands longer than L_{cr} reverse by nucleation and propagation of domain. As an example, in Fig. 3.5 the island 11 exhibits approximately the same area as island 16 but its switching rate is 31 times higher. This is due to different process of magnetization reversal. The energy barrier is found to be $E_{CR} = 32.2^{+5.3}_{-8.6}$ meV and $E_{DW} = 23.7^{+8.6}_{-9.1}$ meV for coherent rotation

3.3. SHAPE-DEPENDENT EFFECT ON THE MECHANISM OF MAGNETIZATION REVERSAL

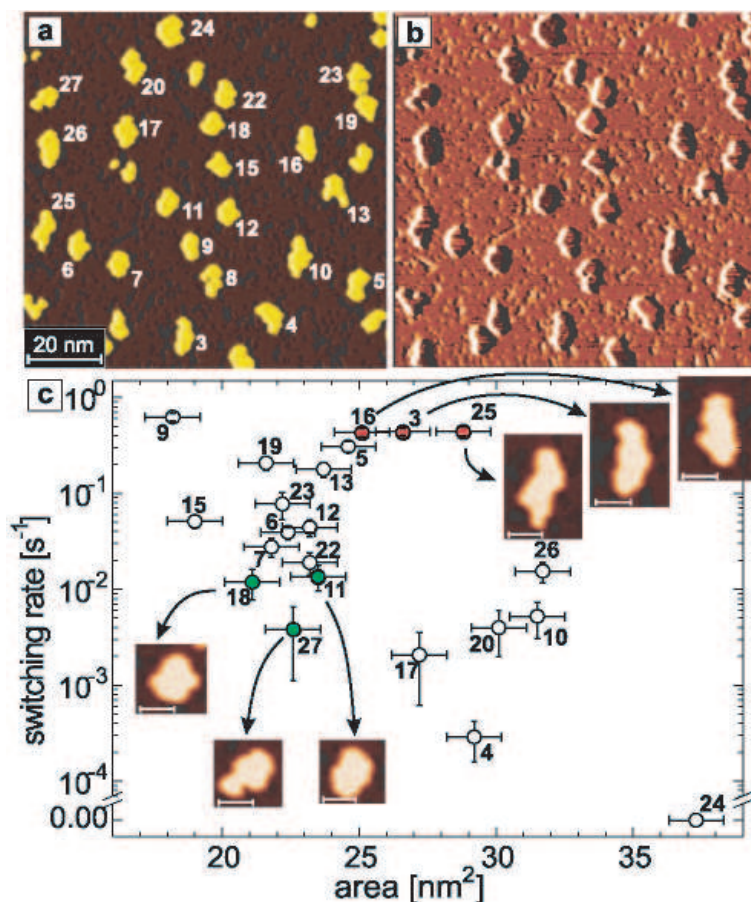


Fig. 3.5 – (a) Topography and (b) magnetic dI/dV signal of Fe islands on Mo(110) at $T = 13$ K. (c) Plot of the switching rate vs. the area of individual islands. The scatter of the switching rate points to a shape-dependent crossover from coherent rotation of compact Fe islands shorter than $L_{cr} = 91 \pm 3$ Å toward nucleation and expansion of reversed domains in elongated islands. (Insets) Topography of selected Fe islands (scale bar : 50 Å) [124].

and domain-wall nucleation, respectively. This explains qualitatively the higher switching rate of elongated islands compared to that of compact islands of equal volume. It is worth noticing that this technique cannot allowed a direct observation of the magnetization reversal. This process occurs on a time scale ($\approx 10^{-12}$ s) being much shorter than even the time increment between subsequent pixels ($\approx 10^{-3}$ s).

Mono- and bilayer Co islands on Pt(111) have also been investigated with SP-STM [138, 179]. It was shown that compact one monolayer thick Co nanostructures with base length until 600 Å are always seen mono-domain even if stripes structures exhibit domain-wall with width of 40 Å (Fig. 3.6). It was also observed that the overall magnetization of each island was oriented out-of-plane in the magnetic virgin state of the sample at a magnetic field of 0 T. Meier *et al.* interpreted this as a proof that the easy axis of magnetization was out-of-plane over all the island in contradiction with previous results. Prior to this studies, it was shown by integra-

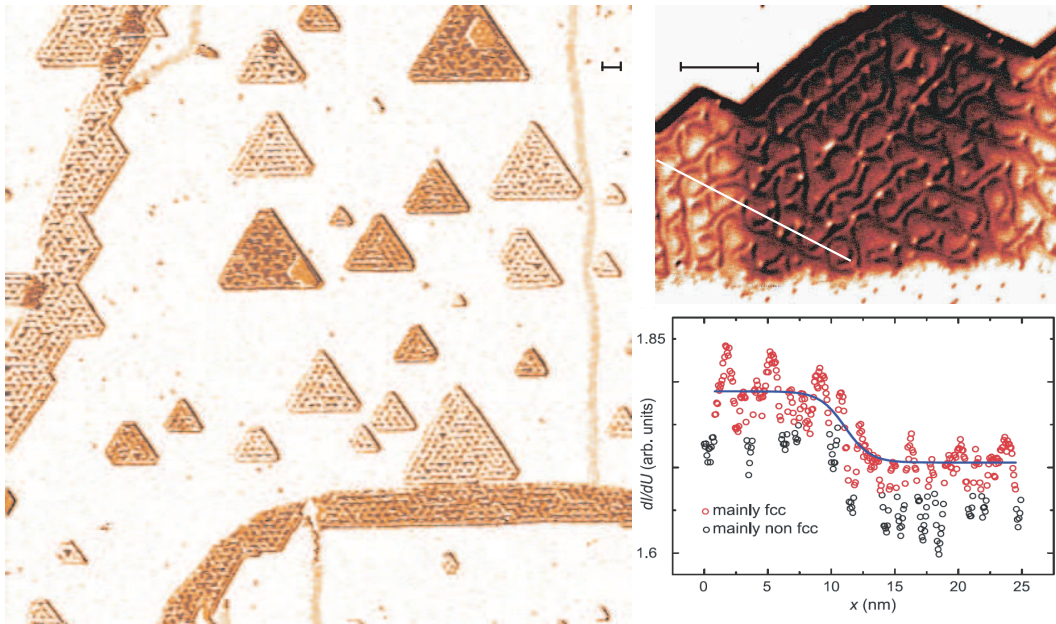


Fig. 3.6 – Out-of-plane sensitive magnetic dI/dU map of a Co monolayer islands (left) and wires (upper right) of Co on Pt(111) prepared by Co deposition on the Pt(111) surface at room deposition. No magnetic domain is observable on the islands while three domains are seen on the wires. (lower right) Domain wall profile (open circles) along the white line. The solid line gives a fit to the red data points. (scale bar :100 Å) [138].

ting magnetometry measurements [128] that a strong enhancement of the magnetic anisotropy occurred at the lowest coordinated atoms of the Co islands. A weak in-plane anisotropy and a strong out-of-plane anisotropy were deduced for inner and outer Co atoms, respectively. The question was partially solved by Rohart *et al.* [144] who demonstrated that circular one monolayer thick Co islands with enhanced magnetic anisotropy on edge atoms have mono-domain magnetization state until they reverse from out-of-plane to in-plane magnetization. The authors demonstrated also that even if the macrospin model failed rapidly with the diameter of the islands, the magnetization reversal remained closed to coherent rotation.

The determination of the mechanism of magnetization reversal of Co islands on Pt(111) surface remains an open question. Improvements in SP-STM have permitted to measure magnetization curves of a single adatom [180]. The shape dependent switching field of ferromagnetic islands is now accessible [124]. The use of one of these two techniques should give insight towards a clear evidence of the shape dependence of the magnetization reversal of Co nanostructures on Pt(111). Until then, only spatially integrated method such as μ -SQUID, XMCD and MOKE are suited to disentangle between coherent rotation and nucleation and domain-wall motion. I will address this issue in the next section by correctly fitting zero-field susceptibility MOKE measurements with the rotation coherent model for the two limit cases studied furthermore in this manuscript.

3.4 Mechanism of magnetization reversal in Co nanostructures

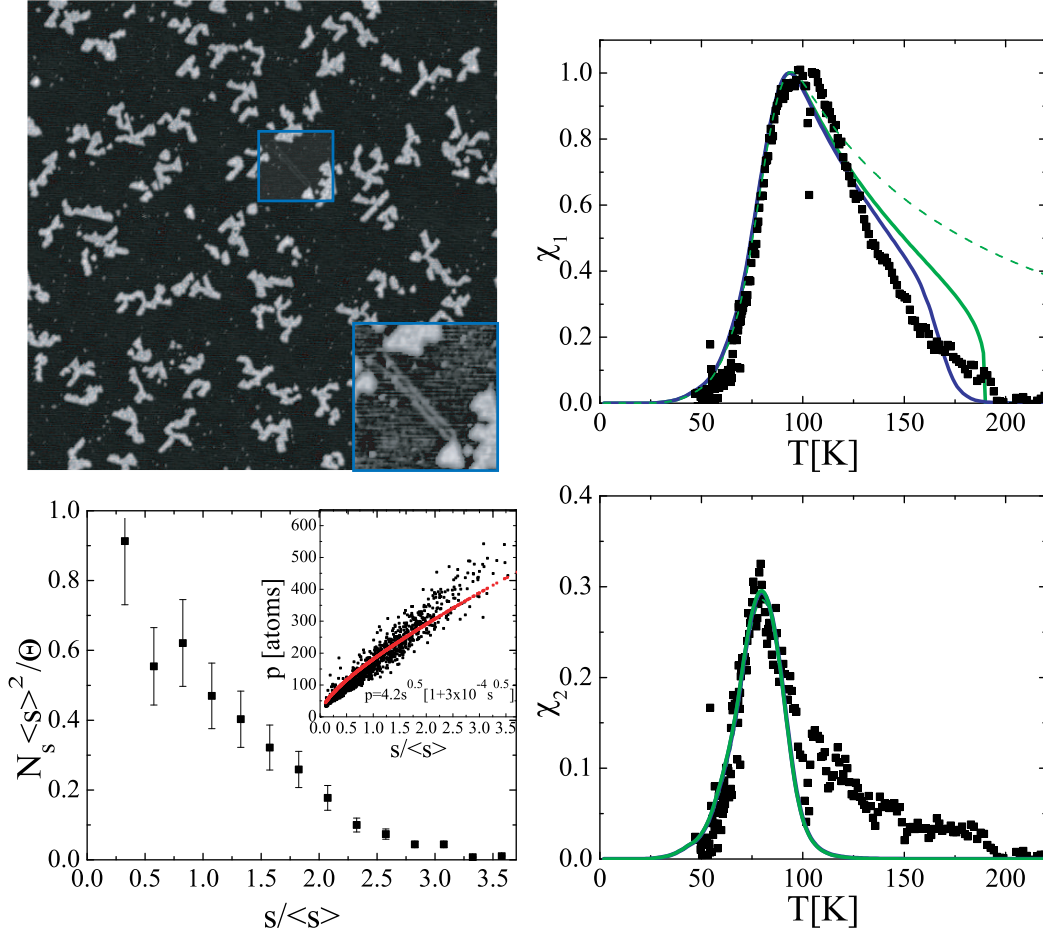


Fig. 3.7 – (upper left) $1500 \times 1500 \text{ \AA}^2$ STM image showing the Co induced double line due to the misfit between Co and Pt (in inset). Reconstructions on Co islands are also characteristic for one monolayer thick Co structures. (lower left) size s and perimeter p distribution, (upper right) real $\chi_1(T)$, and (lower right) imaginary $\chi_2(T)$ susceptibility for Co islands with coverage $\Theta = 0.12 \text{ ML}$. The mean size is $\langle s \rangle = 825 \pm 600$ atoms. For all three curves, $K_v = sE_s + pE_p$. The dashed green, full green and full blue curves represent the best fits assuming $T_C = \infty$, $T_C = 190 \text{ K}$ and T_C given by the Bander and Mills formula, respectively ($\Theta = 0.08 \text{ ML}$, $T_{dep} = 150 \text{ K}$, subsequent addition of $\Theta = 0.04 \text{ ML}$ at $T_{dep} = 250 \text{ K}$).

With atomic beam epitaxy, several islands morphologies can be produced by controlling the growth parameters [63]. The islands in Figs. 3.7 and 3.8 are formed upon two-step deposition of Co on Pt(111). Co deposition on Pt(111) at 150 K formed ramified islands due to limited mobility of atoms along the island edge. Further deposition at 250 K does not change the density of islands but increase the size and compactify the island by increasing edge mobility. The comparison between the small ramified islands (Fig. 3.7) and the large compact islands (Fig. 3.8) gives an

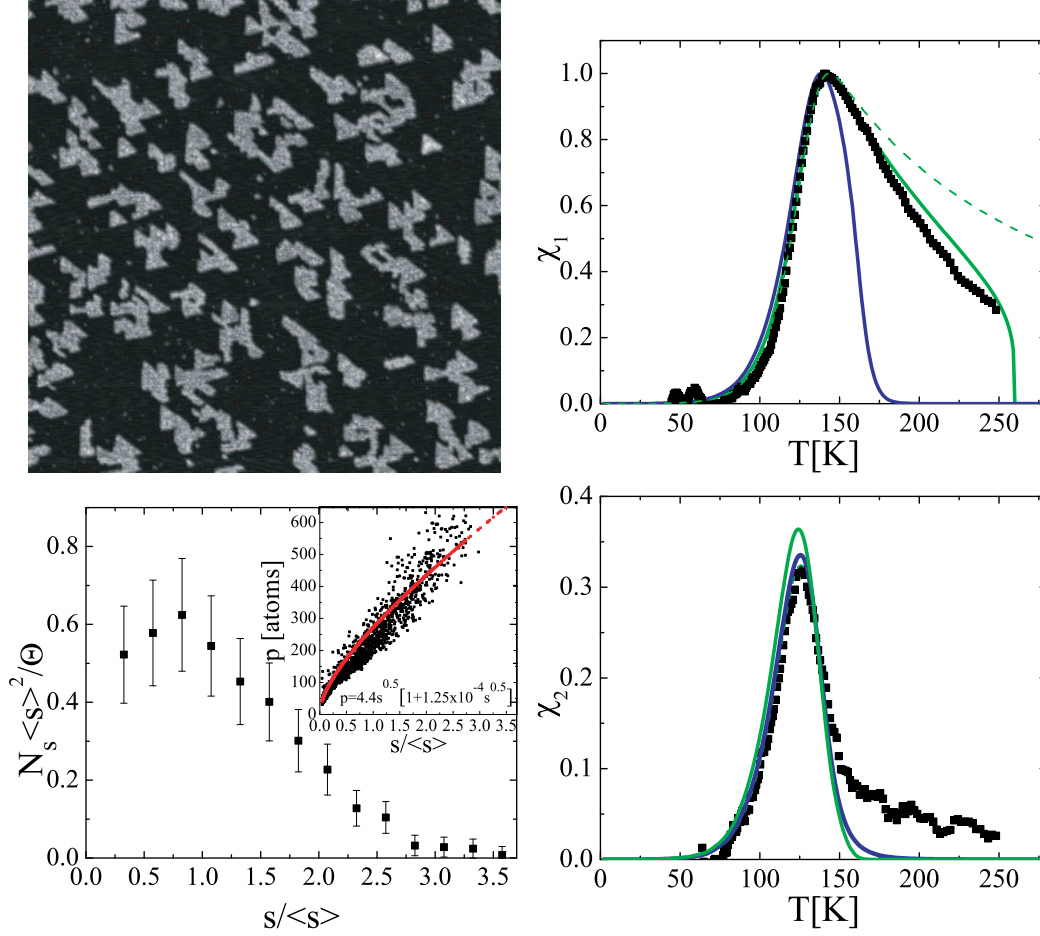


Fig. 3.8 — (upper left) $1500 \times 1500 \text{ \AA}^2$ STM image. Reconstructions on Co islands are characteristic for one monolayer thick Co structures. (lower left) size s and perimeter p distribution, (upper right) real $\chi_1(T)$, and (lower right) imaginary $\chi_2(T)$ susceptibility for Co islands with coverage $\Theta = 0.27 \text{ ML}$. The mean size is $\langle s \rangle = 1766 \pm 1250$ atoms. For all three curves, $K_v = sE_s + pE_p$. The dashed green, full green and full blue curves represent the best fits assuming $T_C = \infty$, $T_C = 260 \text{ K}$ and T_C given by the Bander and Mills formula, respectively ($\Theta = 0.08 \text{ ML}$, $T_{dep} = 150 \text{ K}$, subsequent addition of $\Theta = 0.19 \text{ ML}$ at $T_{dep} = 250 \text{ K}$).

overview of the mechanisms of magnetization reversal that occur in one monolayer thick nanometer-sized Co nanostructures on Pt(111).

The island size and perimeter distributions were obtained from a statistical ensemble of about 1200 islands imaged by STM for each sample. The size distributions are normalized to yield unit area under the curves. The mean sizes for the two samples are: $\langle s_1 \rangle = 825$ and $\langle s_2 \rangle = 1766$ atoms. The standard deviation is 600 and 1250 atoms, respectively. The nonlinear relationship between the island area and perimeter length (see insets) gives each of the two distributions its characteristic shape, thus enabling to disentangle the different role played by inner and outer atoms.

The magnetic behavior was characterized by measuring the temperature dependence of the zero-field susceptibility with MOKE. Independent of island shapes and

3.4. MECHANISM OF MAGNETIZATION REVERSAL IN CO NANOSTRUCTURES

sizes, a MOKE signal was observed only in polar configuration demonstrating an out-of-plane magnetization easy axis. The $\chi(T)$ curves were measured as the field derivative of the Kerr intensity with the external field sweeping around zero with frequency $\omega = 11 \text{ rad.s}^{-1}$ and an amplitude of ± 50 Gauss.

The fits of the experimental data were done assuming magnetization reversal by coherent rotation. MOKE is a spatially integrated method (the laser spot size was about 1 mm^2) reporting the properties of the island ensemble. Accordingly, we sum over all islands, taking their size and perimeter distribution into account. The $\chi(T)$ functions for a given island are the real and imaginary functions determined in section 3.2.1 for the case of coherent rotation. However, up to now, the overall magnetic moment $M_v(T)$ of the nanoparticle was assumed to be temperature independent which is equivalent to assuming an infinite Curie temperature. We use a more realistic description by introducing the temperature dependence of the magnetic moment in order to take into account that at $T = T_C$ the thermal energy overcomes the exchange energy causing the breaking of the ferromagnetic order in the island macrospin. We assume that $M_v(T)/M_v(0) = [(w(T) + 1)^3/(w(T) - 1)^3]^{1/8}[(w(T) - 3)/(w(T) + 3)]^{1/8}$, where $w(T) = \exp(4A/T)$ and $T_C = 4A/\ln(3)$ [181], which is the exact expression for the temperature dependence of the magnetization of a plane triangular Ising lattice. $M_v(0)$ is taken to be equal to sm , s being the number of constituent atoms and m their magnetic moment. This results in an abrupt drop of the real part of the susceptibility ($\chi_1(T)$) to zero at $T = T_C$ and a small increase of the observed T_B . This assumption is justified because m varies by much less than 20% for the size range of interest ([182] under the light of [183]). Note also that $M_v(0)$ respectively m enter as a scaling factor on the vertical axis. This implies that errors on m do not affect the shape of $\chi(T)$ which is used to determine K_v .

K_v strongly depends on the coordination of the constituent atoms [34, 184–186]. Therefore, the natural choice for the expression of K_v is $K_v = sE_s + pE_p$, where E_s and E_p are the contribution of highly coordinated (inner) and low coordinated (edge) atoms, respectively.

During the fit procedure, the value of the perimeter of each island was derived from the relation between surface and perimeter given in Figs. 3.7 and 3.8 and not directly from the data. The direct consequence of this procedure was a narrowing of the susceptibility peak. This approximation is justified if one considers that for islands of a given surface, the value of the perimeter fluctuates around a mean value following a binomial distribution. Hence, the ratio of the standard deviation of the distribution of perimeters over the mean value decreases by increasing the number N of islands following a $\frac{1}{\sqrt{N}}$ law. The large number of islands integrated in the MOKE signal (10^9 islands) compared to the number of islands collected by STM measurements (1200 islands) justifies the fitting procedure explained above. One should notice that the relation between perimeter and surface is not the classic one $p = \alpha s^\beta$ but has been modified to $p = \alpha s^{0.5} + \gamma s$ in order to give a better fit to the data assuming that the first term corresponds to compact shapes and the second corresponds to elongated shapes where the length increases much more rapidly than the section.

By simultaneously fitting the $\chi_1(T)$ and $\chi_2(T)$ curves the following magnetic

anisotropy energies per atom are obtained :

- small islands : $E_p = 1.1$ meV, $E_s = -0.115$ meV
- large islands : $E_p = 1.2$ meV, $E_s = -0.09$ meV

with an error of ± 0.2 meV on E_p and ± 0.003 meV on E_s . The value $E_p \approx 1$ meV/atom associated to edge atoms, having on average four in-plane neighbors, agrees with the MAE/atom measured by means of XMCD in small Co clusters on Pt(111) with a size of 7-10 atoms, where the lateral coordination of the majority of the constituent atoms is comparable [34]. It is also in good agreement with the value of 0.8 ± 0.1 meV/atom observed for Co islands on Au(788) [184], and with the estimate of 1.0 ± 0.3 meV/atom derived from [186] for Co islands on Au(111).

Since MOKE determines the total anisotropy $K_v = K_{MC} + K_{shape}$, it is interesting to evaluate the contribution of both crystalline(MC) and shape anisotropy. We assume cylindrical islands with ratio of one atom height over 50 atoms (100 Å) width. The demagnetizing field is then given by $H_d = -NM \approx -0.95M$ [187], N being the demagnetizing factor. The shape anisotropy per Co atom follows : $E_s^{shape} = \frac{1}{2}\mu_0 H_d M v_{at} = \frac{1}{2}\mu_0 \frac{0.95m_{Co}^2}{v_{at}} = -0.12$ meV, assuming a value of $2.1 \mu_B$ for the magnetic moment of Co [6]. One deduces $E_s^{MC} = 0.02 \pm 0.01$ meV for Co islands, which is surprisingly closed to bulk value. This result must be seen carefully as the value of N was estimated for an ideal circular shaped island and without taking into account any magneto-elastic contribution which has been seen to contribute strongly to the magnetic anisotropy energy (MAE).

The larger error in the estimation is not due to deficiencies in the fit procedure but is due to the fact that nominally identical samples actually show different T_B . Possible causes are the different strain affecting border atoms in islands [185] modifying the local density of states or different relaxation of the tensile stress taking place during the annealing procedure. Small oxidation induced variations of T_B are also awaited between samples when the base pressure or the measurement period slightly differs. [188]

3.5 Discussion

The real and imaginary zero-field susceptibility of the two limit sizes of Co islands studied was correctly fitted by the coherent rotation model with a magnetic anisotropy energy barrier divided in a perimeter and surface contribution. $M(T)$ was also assumed to follow the exact temperature dependence of the magnetization of a plane triangular Ising lattice giving $T_C = 190 \pm 10$ K and $T_C = 260 \pm 10$ K for small and large islands, respectively. Nevertheless, some divergences with the fit appear in the high T part of the $\chi_1(T)$ and $\chi_2(T)$ curves. Some are directly ascribed to the phase fluctuations from -180° to $+180^\circ$ in the temperature range when the imaginary part of $\chi(T)$ vanishes. However, it is necessary to discuss other effects such as the distri-

bution of anisotropy, the finite-temperature effect or the inter-island interactions in order to get a better insight in the understanding of the queue of $\chi(T)$ curves.

Magnetic anisotropy vs. size distribution

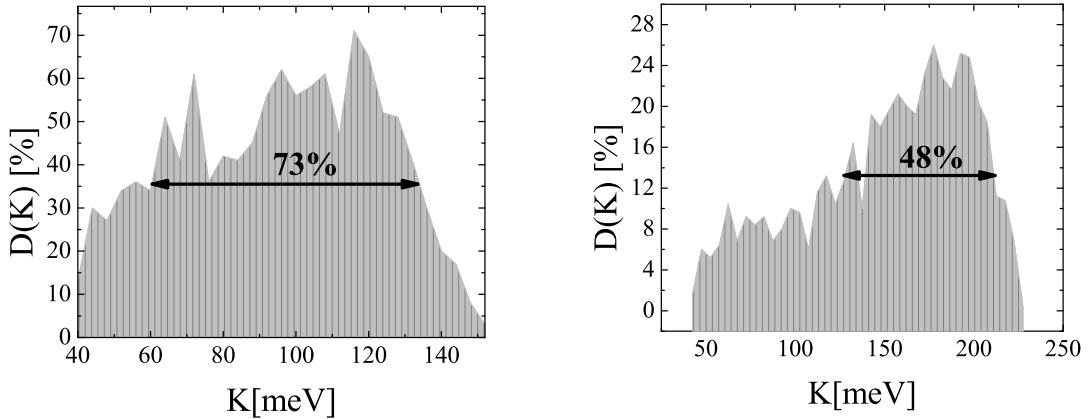


Fig. 3.9 – Distribution of anisotropy energy for the small (left) and large (right) Co islands grown on Pt(111). The FWHM is comparable to the best values obtained with colloids [189].

The predominant role played by the border atoms in determining the MAE is directly pointed out by the shape of the $\chi_2(T)$ curves. A MAE proportional to the island size would result in a much broader $\chi_2(T)$ curve with respect to the measured one. This directly follows geometrical considerations since for both small and large islands, the island size has a larger distribution than the one of the perimeter. By comparing with 3D colloid particles, where the MAE distribution is always larger than the one of the size [189], this also means that arrays of 2D nanoparticles grown by MBE may achieve narrower MAE distribution than anticipated on the basis of the size distribution alone. Experimentally, a very narrow MAE distribution with 34% for the Full Width at Half Maximum (FWHM) was achieved by Weiss *et al.* on non-interacting Co nanoparticles on Au(788) [184]. In our experiments, the distribution of anisotropy energy used to fit $\chi(T)$ is given in Fig. 3.9 for both small and large islands. One finds 73% and 46% FWHM in the case of small and large islands, respectively. These low values compared to the size distribution illustrate the narrow distribution in energy in grown nanoparticles.

We observe a narrowing of the anisotropy distribution with the island size. This evolution of the anisotropy distribution is qualitatively similar to the one of the size distribution. Therefore, we interpret the narrowing of the anisotropy distribution with island size as a pure geometrical effect associated with the island shape which compactifies and narrows the size distribution with increasing coverage. An other explanation has been proposed in the case of Co islands on gold surface by Rohart

et al. [190]. The authors attribute the origin of the MAE and its variation with the island size to the low-coordinated atoms combined with magnetoelastic effects.

As a concluding remark, it is worth noting that the island size distribution participates actively to the determination of the blocking temperature. The measured blocking temperature does not correspond to the T_B of the mean island but to the T_B of the islands which give the strongest contribution to the zero-field magnetic susceptibility. In our case, the corresponding island size responsible for the measured T_B is around $(1.8 \pm 0.1) \langle s \rangle$ for all the samples.

Choice of Curie temperature

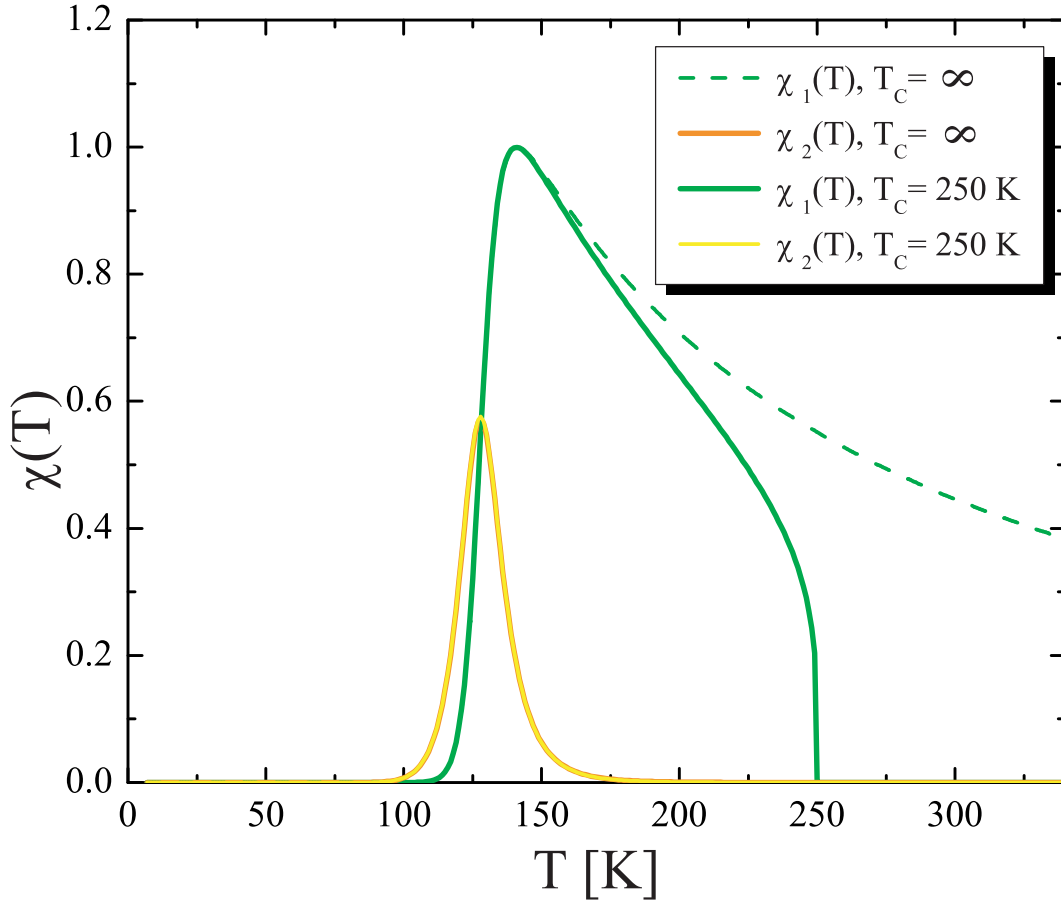


Fig. 3.10 – Zero-field susceptibility curves in the coherent rotation model with (blue and orange lines) and without (green and yellow lines) finite-temperature effect on M . (see Fig. 3.2 for parameters)

On the previous analysis, the temperature dependence of the magnetic moment was assumed. T_C was chosen to give the best fit. The consequence in the fit was an abrupt drop of the susceptibility starting few Kelvin before T_C . As a comparison, similar analysis were performed without any temperature dependence of the intrinsic

parameters, i.e. $T_C = \infty$ (see Figs 3.7 and 3.8). One first notices that T_B is not affected by this change. However, $\chi_1(T)$ exhibits the more gentle $\sim 1/T$ slope that is expected from the macrospin model (see Fig. 3.10) and, therefore, does not fit anymore with the MOKE measurements. The normalized $\chi_2(T)$ is not affected by the choice of infinite T_C . One deduces from this analysis that it is necessary to adapt finite-temperature effects to the macrospin model.

The absence of the abrupt drop of the susceptibility signal at T_C can probably be ascribed to the island morphology. Some small second layer clusters in fact decorate the compact islands. Because T_C strongly depends on coordination, these second layer nuclei can locally increase the island T_C explaining the weak signal still visible around the estimated Curie temperature. The partial Co/Pt exchange that was previously observed after annealing at 375 K [191] could also be present at lower temperature and thus participated to an enhancement of the Curie temperature as well as a widening of the island MAE distribution which is seen as a widening and flattening of the $\chi(T)$ curves.

Until the previous discussion, T_C was assumed to be independent of the size and shape of the islands. Nevertheless, various works have predicted a strong thickness- and inhomogeneity-dependence of T_C [192, 193]. Bander and Mills have demonstrated that there is a critical temperature for a 2D Heisenberg ferromagnet if a uniaxial anisotropy is present in the system [194]. In this model, the anisotropy constant K is temperature-independent. Thus, the new so-called 2D Curie temperature is inferred by the relation :

$$T_{2D} = T_{3D} / \ln \left(\frac{3\pi k_B T_{3D}}{4K} \right) \quad (3.12)$$

where T_{3D} is the Curie temperature of the same Heisenberg ferromagnet in three dimensions.

This expression of T_{2D} can be addressed for each Co particles independently. The result is a narrow queue in the $\chi_1(T)$ curves and a better fit in the case of the small islands (see Figs. 3.7 and 3.8). On the contrary, in the case of the large islands, the susceptibility curve vanishes around 200 K. The difference between the results and the theory can be inferred from the fact that a magnetic nanoparticle is by definition non infinite and also that interactions between Co atoms and the underlying Pt substrate assure that we cannot strictly speak about a 2D Heisenberg magnet. Nevertheless, the approach of Bander and Mills has the merit to be the only one, to my knowledge, to take into account the anisotropy constant in the determination of the 2D Curie temperature.

Finite-temperature effect on K_v

A strong temperature dependence was predicted for the MAE by Akulov [195]. Callen and Callen [196] have calculated the power law $\frac{K_v(T)}{K_v(0)} = \left(\frac{M_v(T)}{M_v(0)} \right)^\gamma$ with γ to be 10 for cubic anisotropy and 3 for uniaxial anisotropy. This power law is not

true for alloys on surface [197] and a correction to γ must be applied. In order to take into account these considerations, analysis have also been performed using finite-temperature anisotropy with $\gamma = 2$ and 3 [198–200]. The observed effects on χ were a reduction of T_B of around 10 K and a small narrowing of the curve. Hence, the values of E_s and E_p should be slightly increased in order to take into account finite-temperature effects on K_v .

Inter-island interactions

It was shown that mutual dipolar interactions between nanoparticles considerably flatten the $1/T$ slope of the real part of the susceptibility in the superparamagnetic regime [201, 202]. The absence of such flattening is already a good argument for the absence of dipolar interactions. Another good argument [184] can be inferred by comparing the switching field H_{sw} of a given island with the stray field H_{stray} created by the presence of its neighbors. An upper bound to the stray field is obtained assuming all macrospins of the neighbors to be aligned. Considering an ensemble of monodisperse compact monolayer particles containing 1200 atoms ($K_v \approx 190$ meV and $M_v \approx 160$ meV/T), one gets $H_{stray} \approx 30$ Oe (Eq. (4) of Ref. [203]). The temperature dependence of the switching field is given by $H_{sw} \approx H_0(1 - \sqrt{T/T_B})$ [204], where $H_0 = 2K_v/M_v = 2.4 \times 10^4$ Oe. The switching field becomes comparable to the stray field only in the narrow interval $0.995 T_B < T < T_B$.

Ferromagnetic coupling between adjacent islands mediated by the polarization of the Pt atoms of the substrate has to be discussed. As reported in Co/Pt layered systems [205–207] (or more generally [208]) and Co-Pt alloys [209–211] or Co adatoms on Pt surface [34, 180], Pt atoms that are paramagnetic in the bulk are significantly polarized in the vicinity of ferromagnetic Co atoms. Two kinds of polarization are then considered. On one hand, the exchange interaction leads to spin polarization of the Pt atoms. Planar interfaces between ferro-metal-ferro give rise to the oscillating RKKY-type interactions. This was seen recently on Co adatoms on Pt(111) surface in the vicinity of a monolayer stripe [180]. The exchange energy was around 0.1 meV at 10 Å of the monolayer stripe. These low values of exchange energy associated with a different magnetic configuration support the fact that we can ignore this kind of interactions. On the other hand, Co atoms induce a strong enhancement of Pt orbital moment. The magnetization profile of the Pt atoms can be approximated by an exponential function with a decay length of 4.1 Å, corresponding to the second Pt atoms, which characterizes the effective range of the magnetic coupling between Co and Pt [206, 207, 211]. In our experiments, the islands density is $\sim 2 \times 10^{-4}$ islands/sites on the Pt(111) surface and the characteristic length of an island is about 40 – 80 Å, yielding the distance between islands to vary around 35 – 115 Å. Thus, to a very good approximation, one can neglect the broadening of the $\chi(T)$ curves due to substrate induced magnetic interaction between islands.

3.6 Other mechanisms ?

Disentangling the mechanism of magnetization reversal in small and large, ramified and compact nanostructures requires more than correctly fitting the $\chi(T)$ curves of the two limit sizes and shapes Co nanostructures. A comparison showing the transition from one mechanism to the other is of great help in order to achieve this disentanglement. In this section, I sum up interesting attempts to explain extrinsic magnetic properties of ferromagnet with various models. To my knowledge, none of these models could directly be compared with our analysis. Therefore, we propose a model to describe the magnetization reversal by domain-wall motion after nucleation based on the macrospin model with a modified energy barrier. The comparison between the two models is extended over more kind of nanostructures. A non purely coherent rotation mechanism of magnetic reversal is ultimately observed for ramified islands grown to have longer arms than in the previous study.

State of the art

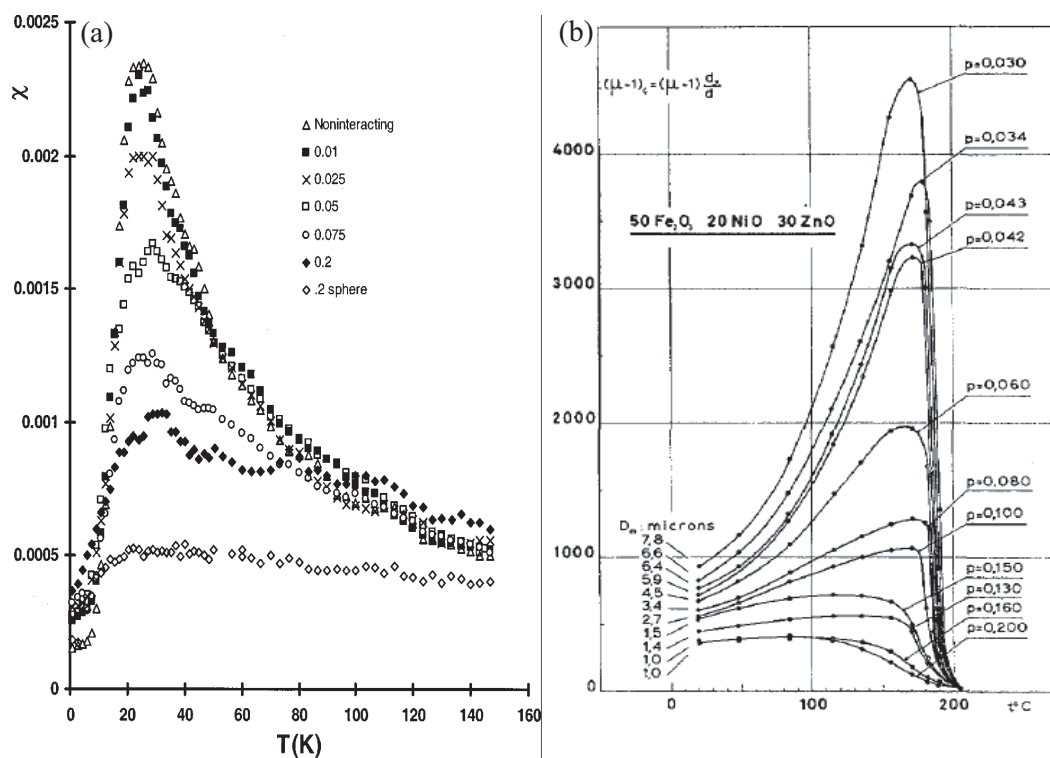


Fig. 3.11 – (a) Susceptibility vs temperature for various packing densities for Co particles with median diameter 30 \AA and standard deviation 1. Values of packing density are indicated in the legend. Here the coherent model is modified in order to take into account the dipolar field created by adjacent particles [201]. (b) Temperature dependence of corrected zero-field susceptibility for samples of varying diameter. The experimental data are explained by the Globus model of spherical particles with one moving domain-wall [212, 213]

In real materials, the ideal macrospin model is not verified. This is due to inhomogeneities in the demagnetizing field or local variation of the intrinsic magnetic properties, *e.g.* induced by a local variation of the atomic coordination. Nevertheless, this model has the advantage to be totally solved analytically and to be relatively flexible. One good example was used here by adding to this model the finite-temperature effects and the spatial variation of the anisotropy constant. Therefore, this model is frequently used with success to describe magnetization and susceptibility curves as well as relaxation rate [214]. Other adaptations of this model have been proposed to take into account the dipolar interaction between magnetic particles [201, 202](see Fig. 3.11(a)) or magnetization reversal discontinuities associated with nucleation and propagation phenomena [215, 216]. Most of the proposed models whether they are phenomenological or atomic models are computed by micromagnetic calculations [213, 217] and only in few cases an analytical solution is given [218, 219]. The multiplication of free parameters has the advantage to give better fit to the experimental data but the drawback to add uncertainty and not to allow a clear understanding of the mechanism of magnetization reversal. In this idea, a 2D adaptation of the Globus model may worth some interest from theoreticians [163, 212](see Fig. 3.11(b)). This model deals with spherical magnetic particles whom magnetization is driven by the motion (bowing and translation) of a single domain-wall. The few numbers of free parameters and the simplicity of the model makes it appealing to produce a direct comparison between magnetization reversal by coherent rotation and domain-wall motion after nucleation.

The macrospin model adapted to the nucleation and propagation of domains

We note that the energy barrier for nucleation of domain walls may be assumed proportional to the island section. A rough estimation of the distribution of island sections is given by the distribution of the area-to-perimeter ratios. By fitting the $\chi(T)$ curves assuming the energy barrier for switching $K_v = s/pE_{sec}$, where $E_{sec} \propto 4\sqrt{AK_v}$, instead of $K_v = sE_s + pE_p$, gives in general a slightly worse agreement with the experimental data (Fig. 3.12). In the case of small ramified islands, both fits are very similar suggesting a mix of both mechanisms, whether the experimental data corresponding to the compact islands superpose well with coherent rotation.

I present here results on Co islands grown with the same two steps procedure that was previously used but with coverage deposited at 250 K of $\Theta = 0.08$ ML. The mean size of the islands is $\langle s \rangle = 1100 \pm 800$ atoms and the relation between surface s and perimeter p could be correctly fitted by $p = 0.43s^{0.87}$. The result was some ramified islands owning long arms, typically $L_{arm} \geq 150$ Å. Fig. 3.13 shows that for this morphology a model assuming domain-wall motion after nucleation nicely reproduces the experimental data points, whereas the fit assuming $K_v = sE_s + pE_p$ gives an erroneous temperature dependence of $\chi(T)$. The proportionality constant in $E_{sec} \propto 4\sqrt{AK}$, which depends on the actual island shape, can be roughly estimated by comparing the values of the island mean section and of the ratio s/p

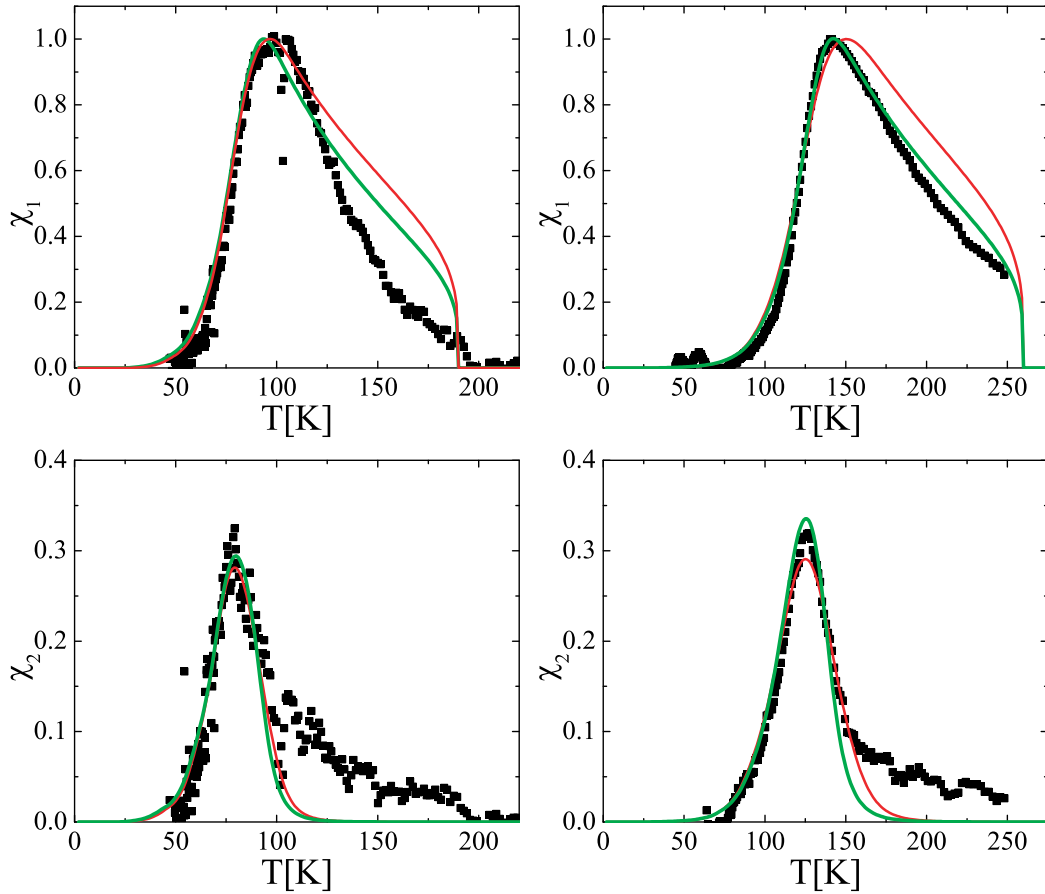


Fig. 3.12 – The experimental $\chi_1(T)$ and $\chi_2(T)$ curves measured for the two limit island sizes (ramified with small arms, compact and large) shown in Figs. 3.7 and 3.8. The red and blue curves represent the best fits assuming $K_v = s/pE_{sec}$ and $K_v = sE_s + pE_p$, respectively.

measured by STM on a set of islands. By doing so and taking the fit value of E_{sec} one estimates $AK = 2.0 \pm 0.5 \text{ meV}^2/\text{atom}^2$. Assuming A to be $12 \text{ meV}/\text{atom}$ gives $K = 0.17 \text{ meV}/\text{atom}$ which is in good agreement with the value usually found for coherent rotation. Altogether, this suggests a transition from coherent rotation to domain-wall motion after nucleation for Co/Pt(111) for ramified islands at a critical length of $L_{cr} \approx 150 \text{ \AA}$. We associate this transition to the strong shape and size dependence of the mechanism of magnetization reversal[124]. Ramified islands are more suited to reverse their magnetization by domain-wall motion while under a critical size and aspect ratio coherent rotation is preferred.

Validity of the model

This rough model can be subject to a strong opposition. Firstly, the macrospin model is clearly inappropriate during the magnetic turnover. Secondly, assuming that the total energy has a $\cos^2(\theta)$ dependency on K_v has no physical meaning for nucleation and/or domains propagation. Thus, this model cannot be seen as the model

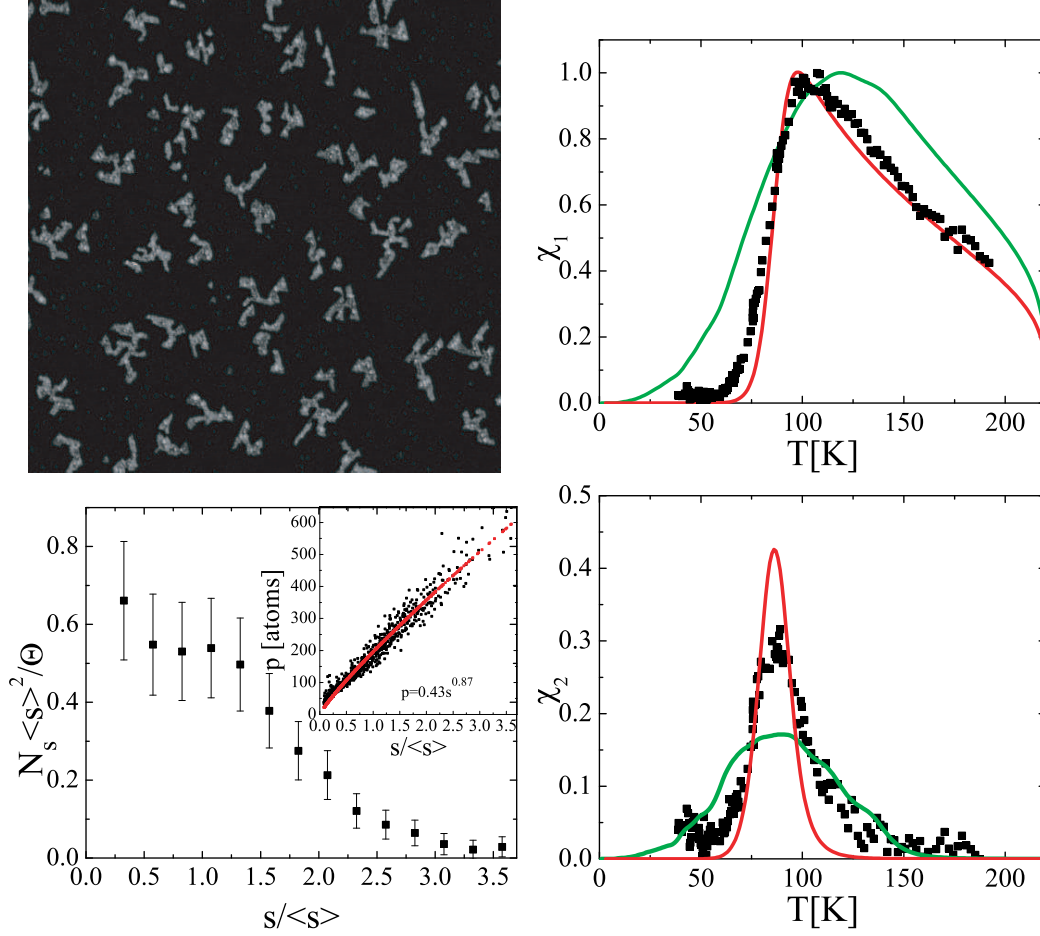


Fig. 3.13 – (upper left) $2000 \times 2000 \text{ \AA}^2$ STM image, (lower left) size s and perimeter p distribution, (upper right) real $\chi_1(T)$, and (lower right) imaginary $\chi_2(T)$ susceptibility for ramified Co islands with arms longer than 150 \AA . The mean size is $\langle s \rangle = 1100 \pm 800$ atoms. The red and green curves represent the best fits assuming $K_v = s/pE_{sec}$ and $K = sE_{as} + pE_{ap}$, respectively. For both curves, $T_C = 220 \text{ K}$ ($\Theta = 0.08 \text{ ML}$, $T_{dep} = 150 \text{ K}$, subsequent addition of $\Theta = 0.08 \text{ ML}$ at $T_{dep} = 250 \text{ K}$).

corresponding to this mechanism of magnetization reversal.

Nevertheless, some strong arguments support this model.

-The timescale during which the magnetization reversal occurs is order of magnitude smaller than the timescale of the measurement (0.1 s). Therefore, this is impossible to distinguish any variations of the total magnetization, making the first argument flawed.

-The main effect of this model is to change the distribution of energy barrier, consequently the distribution of the so-called "blocking temperature", which is directly reflected in the shape of the $\chi_2(T)$ peak. Nevertheless, the general shape of the normalized $\chi(T)$ curves is identical for each individual island. The shape of $\chi_2(T)$ as well as the abrupt raise in $\chi_1(T)$ for one island do not show a strong dependence on the mechanism of magnetization reversal. The key parameters to describe this

part of the curves are ω the frequency of the external sweeping field and the value of the energy barrier K_v , assuming a same attempt frequency for both mechanism. As an example, assuming a typical value of $K_v = 160$ meV and a frequency of 11 Hz gives a reduction of 14% and 27% of the peak value due to $\chi_{eq}(T)$ decreasing with a $1/T$ or $1/T^2$ slope, respectively, with respect to no temperature-dependence of χ_{eq} . As a contrary the downward slope of $\chi_1(T)$ is *per se* the direct expression of the mechanism of magnetization reversal as far as the finite-temperature effects can be ignored. However, it has been seen that T_C influences the slope of the curve very early after the peak. Therefore, once again, the mechanism of magnetization reversal can be ignored in a rather good approximation.

3.7 Conclusions and perspectives

The temperature dependence of the real and imaginary part of the zero-field susceptibility curves of Co nanostructures of different sizes and shapes has been described by a model of magnetization reversal by coherent rotation adapted to the finite-temperature effect and to the non-uniform repartition of anisotropy [128] and also by a model adapted to domain-wall motion after nucleation. The limits of the models were discussed. The results support that a transition mechanism occurs when the nanostructures are ramified with long arms around 150 Å. For ramified nanostructures with short arms, the mechanism responsible for magnetization reversal was not clearly distinguished and is presented as a probable mix of both coherent rotation and nucleation and propagation of domains. A probable cause of this mix is due to the large polydispersity in the size distribution. Ramified islands with longer arms present an unequivocal preference for magnetization reversal via nucleation and propagation of domains. On the contrary, the mechanism of magnetization reversal of large compact islands with narrower size distribution is well described by coherent rotation. Between these two limit cases exist a complex transition mechanism of magnetization reversal corresponding to the transition from ramified to compact nanostructures. These results strongly support the idea that the magnetization turnover is inferred to the size and the shape of the nanostructures.

The comparative use of two methods is always preferred in order to disentangle the origin of the magnetization reversal. In this chapter, we have based our analysis on the different temperature dependence of $\chi(T)$ curves making use of different distribution of energy barrier to reverse the magnetization. Alternative experiments and analysis may be achieved in the future in order to give a deeper understanding on the process of magnetization reversal. As an example, comparison with $\chi(T)$ curves corresponding to models solved analytically or by micromagnetic simulations could be performed. These models should involve inhomogeneities due to the high degree of ramification of the nanostructures which would act like a viscosity term in the motion of domain-wall as well as a perturbation to the nucleation of domain. A mean-field approach seems more reasonable as every islands shows different degree of ramification.

An other solution consists on performing magnetization curves near the Curie temperature [220], which is then assumed to be island-independent. Near the Curie

temperature, the remanent magnetization M_r as well as the saturation magnetization M_s should be strongly reduces following a power law similar to the one that was used during the analysis. Thus, a direct observation of their value may be measurable and the critical exponent of the power law should be deduced. The temperature dependence of M_r and M_s gives rise to T_r and T_C , the temperature for which $M_r = 0$ and $M_s = 0$, respectively. Coherent rotation process results in $T_r = T_C$, which is not the case for domain-wall propagation after nucleation. Altogether, the critical exponent and the difference between T_r and T_C compared with models of magnetization reversal taking into account the size distribution of the islands should allow one to gain accuracy on the determination of the magnetization reversal process.

Magnetism of Co-based nanostructures

4

In the framework of the exponential growth of information storage density, industry has pushed the size limit of a bit of information to the nanoscale. The reduced dimensionality at the surface of a thin film or at the edge of a nanostructure leads to more atomic-like electronic properties. 2D nanostructures created and analyzed under well-defined conditions (UHV, STM, and in situ magnetic characterization) represent an ideal prototype system to investigate the role of the different anisotropy energies and the contribution due to the different atomic environments. Being able to build nanostructures with tailored magnetic properties becomes of great importance for magnetic data storage application. This goal might be fully achieved by means of core-shell nanostructures. For example, putting an element with low anisotropy at the edge and an element with high moment in the middle of the island produces soft magnets with high moments and therefore very low switching fields. On the other hand, hard elements at the border and nonmagnetic elements in the middle increase the islands anisotropy while minimizing its overall magnetic moment. To this purpose, bimetallic $3d-3d$ and $3d-4/5d$ alloys are perfectly suitable structures. In this chapter, we report on the magnetism of bimetallic FeCo, CoPt and CoPd 2D islands. Self-assembly of atoms deposited by atomic beam epitaxy (ABE) on a crystalline substrate surface allows to grow 2D islands with atomic scale control. The easy axis of magnetization was always measured out-of-plane for all the samples. Magneto-optic Kerr effect measurements permits us to access the energy barrier for magnetization reversal through the blocking temperature T_B . The different contributions to the blocking temperature arising from the stoichiometry, from the chemical configuration and from the low-dimension effect are disentangled thanks to the investigation of distinct kinds of core-shell nanostructures.

In a first part, we investigated the T_B -dependence on the alloy composition x in $\text{Fe}_x\text{Co}_{1-x}$ shell/Pt core nanostructures, with x varying from $x = 0$ to 1. We also

estimate the T_B variation when Fe-Co and Pt-Co interfaces are created in Co islands decorated by Fe or Pt atoms. Experimental results were compared to calculations performed by Bornemann *et al.* in Munich. They performed fully relativistic *ab initio* calculations of the magnetocrystalline anisotropy energy K_{mc} and the anisotropy of the orbital moment μ_{orb} for different core-shell hexagonal islands made of up to 271 atoms deposited on Pt(111). The total number of atoms in the pure Co islands has been varied from 1 to 271. Bimetallic islands composed of a Co core and a Fe or Pt shell have been studied with a shell thickness from 1 to 3 atomic rims. The experimental features can be well-accounted for by the theoretical results. We discuss the lengthscale over which the magnetic properties are affected at the interface.

In a second part, the origin of the magnetism of bimetallic CoPd nanostructures is discussed on the basis of the analysis of two different systems. The first one reproduces the previous experiments with core-shell islands. In this case, Co cores are decorated with Pd. The second system refers to Co islands followed by a Pd deposition at 50 K. At this temperature, the mean free diffusion path of Pd atoms is strongly reduced. Therefore, small Pd clusters grew over the entire substrate with a statistical repartition. Quantitative analysis disentangles the contribution to T_B of the creation of a lateral and a vertical interface between Co and Pd. The "lateral" energy yields -0.18 ± 0.05 meV/atom, which give in-plane contribution to the magnetic anisotropy. We found the peculiar result that the "vertical" energy varies from 0.05 ± 0.05 meV/atom to 0.23 ± 0.08 meV/atom. This variation of energy is associated with the coalescence of the Pd clusters on top of the Co islands.

4.1 State of the art

4.1.1 Magnetism of CoX (X = Fe, Pt or Pd) bimetallic structures

The most relevant properties for magnetic information storage are magnetic anisotropy energy (MAE) K and magnetic moment M . In order to inhibit thermally activated magnetization reversal the MAE has to be 1.2 eV per bit. Reducing the bit size therefore requires higher MAE per atom. At the same time, the magnetization density of the recording medium must increase in order to stay with technologically available write fields ($H_{wr} \approx K/M$). In order to reduce dipolar magnetic interactions between adjacent bits the easy axis has to be perpendicular to the plane, and finally narrow switching and stray field distributions are required.

Bimetallic alloys represent a viable route to tune both M and the MAE, as these quantities are strongly influenced by compositional effects and lattice distortions. In the case of epitaxial growth of bidimensional nanostructures, the symmetry breaking associated with the reduced dimensionality and the presence of interfaces (with substrate, with vacuum and between magnetic elements) strongly influences the elec-

tronic structure. It implies a narrowing of the d -bands of the density of state (DOS)^a which is known to strongly affect M and the MAE [33]. In the following, I discuss how M and K are affected by the effect of composition in bimetallic alloys. I focus, in particular in the case of $3d$ and $3d - 4d/5d$ alloys.

Tailoring the overall magnetic moment M

Slater-Pauling curves : the case of $3d$ alloys Slater Pauling curves [221] give the evolution of the total magnetic moment of bulk $3d$ alloys with stoichiometry^b. In the case of bulk (bcc) FeCo alloy, a typical bell-shape with a maximum around 30% of Co was observed and predicted [224–229]. Firstly, it was explained by Friedel by means of a rigid band model [230]. Later, calculations of the total and local density of states allows one to understand the variation of the magnetic moment with change of the local atomic environment [224, 226]. A fine tuning of the $3d \uparrow$ and $3d \downarrow$ spin bands is eventually found to be responsible for the shape of the Slater-Pauling curves of bulk $3d$ alloys.

In bulk materials, the high symmetry causes the quenching of the orbital moment. The total magnetic moment is, therefore, mainly given by the spin moment. This is not the case in 2D structures, multilayers and clusters when the presence of interfaces or reduced dimensionality might induce an enhancement of the local orbital moment. Therefore, the variation of the orbital moment of the two species can be inferred from the variation of the $3d \uparrow$ and $3d \downarrow$ spin bands with alloy composition. This variation is induced partly by the reduced dimensionality and the hybridization between the d orbitals of the two magnetic elements together and with the substrate. Despite a different origin, the bell-shape of the Slater-Pauling curve is generally observed in the case of FeCo clusters [231] and, 2D FeCo films [33, 232]. In the case of FeCo multilayers, Pizzini *et al.* [233] reported on two samples with varying Co and Fe concentrations. The average magnetization was enhanced with respect to bulk Fe, and decreased as the Fe thickness increased.

The case of $3d - 4d/5d$ alloys Pd($4d$) and Pt($5d$) are known to be two non-magnetic elements in bulk which are highly polarizable by $3d$ magnetic elements. After deposition of a Co adatoms on a Pd(111) or Pt(111) surface, Pd and Pt in the vicinity of the Co adatoms are polarized. Their magnetic moment decreases exponentially until the fifth [234], respectively the second [34] neighbor for Pd and Pt. Co adatoms on a Pt(111) surface is known to induce an orbital moment on Pt sites as high as $(1.8 \pm 0.7) \mu_B$. This giant magnetization is inferred from the combined effect of the $d-d$ hybridization and the broken symmetry of the system. In multilayered system, Ferrer has shown that only the Pt atoms in contact with the Co overlayer are magnetized ($0.2 \mu_B$) being the magnetization of the second Pt layer about ten times smaller [205].

^aThe limit of band narrowing induced by the reduction of dimensionality corresponds to the discrete energy levels of single atoms.

^bThe term Slater-Pauling curve is also associated to the variation of the Curie temperature T_C of bulk $3d$ elements upon alloying. The observed trend is an increase of T_C with alloying [222, 223].

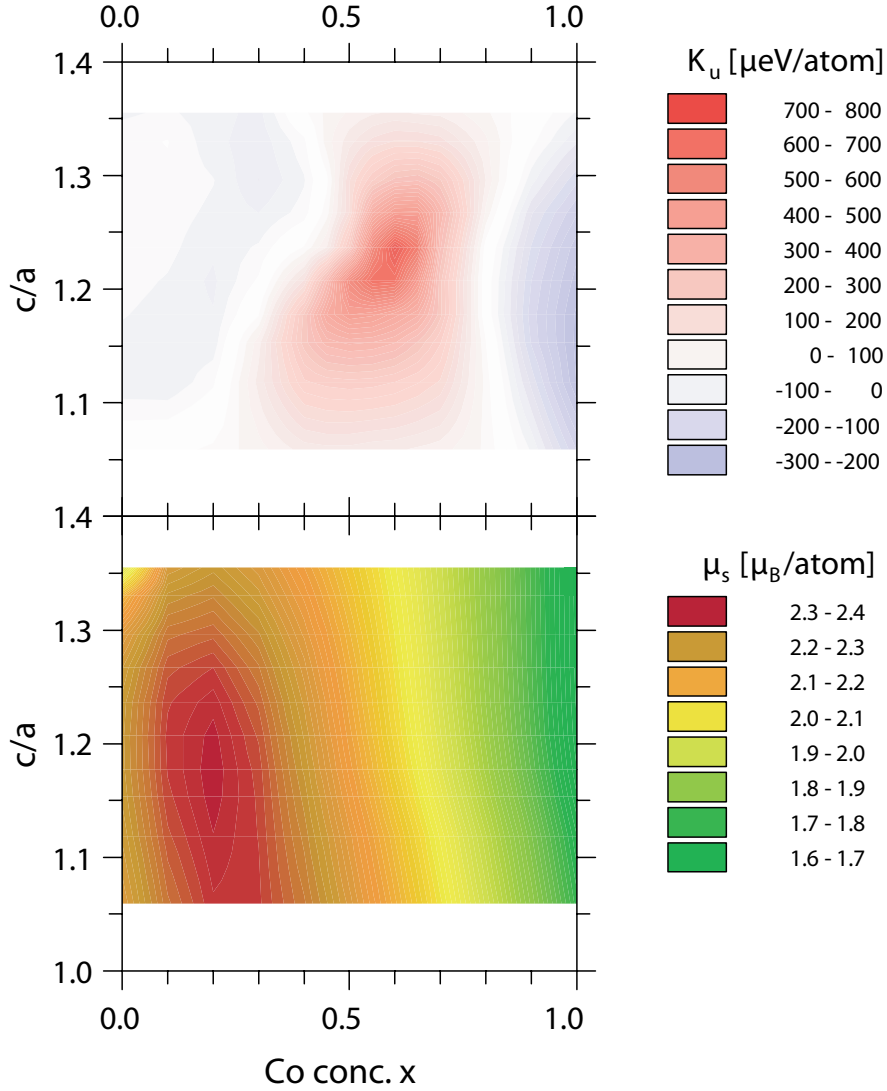


Fig. 4.1 – Calculated uniaxial MAE K_u (top) and saturation magnetic moment μ_s (bottom) of tetragonal $\text{Fe}_{1-x}\text{Co}_x$ as a function of the c/a ratio and the Co concentration x (from [229]).

A recent study from Dennler [235] reviews and estimates the variation of the overall magnetization of $\text{CoRh}(3d - 4d)$ and $\text{CoPt}(3d - 5d)$ clusters and films versus their composition. A quasi-linear growth from no magnetization to the magnetic moment of Co is observed while increasing Co concentration. Therefore, we can roughly conclude that the presence of the $4/5d$ elements has only a fractional role on the overall magnetic moment.

To conclude with, the overall magnetization of a bimetallic structure can be tuned by accurately choosing the two elements of the alloy. FePt and FeCo are good examples of alloys with comparable MAE but with respectively lower and higher magnetic moment with respect to Fe and Co bulk values.

Candidates for high K values

The 3d alloy FeCo The MAE of the bcc FeCo alloys is in the order of only few $\mu\text{eV}/\text{atom}$ [236]. However, based on first-principles calculations, tetragonally distorted FeCo alloys have been promised to exhibit giant magnetic anisotropy energy of the order of 700-800 $\mu\text{eV}/\text{atom}$ (see Fig. 4.1 from [229]). This can be understood as follows. In bulk, the high symmetry of the bcc structure strongly quenches the orbital moment with the consequence that also the MAE is close to zero. A tetragonal distortion destroys the translational symmetry of the bcc structure. The unquenched orbital moment due to the reduced symmetry is accompanied by an anisotropy of the orbital moment itself which in turn generates a large value of the MAE via the spin-orbit coupling.

Suitable, tetragonally distorted $\text{Fe}_{1-x}\text{Co}_x$ alloys were recently realized by growing FeCo/Pt multilayers [237], $\text{Fe}_{1-x}\text{Co}_x$ films on a Pd(001) substrate [238] and $\text{Fe}_{1-x}\text{Co}_x$ films on a Rh(001) substrate [232]. Prior to these works, the evolution of the perpendicular anisotropy had already been studied on the system $\text{Fe}_{1-x}\text{Co}_x$ films on a Cu(001) substrate [239]. In all cases, a largely increased perpendicular anisotropy was found experimentally for specific compositions around $x = 0.6$. Andersson *et al.* report a MAE as high as 210 $\mu\text{eV}/\text{atom}$. The strong composition dependence of the MAE [33, 232] reflects the variation of the orbital moment in agreement with the models of Bruno [126] and Van der Laan [127].

From an other aspect, a strong enhancement of the MAE caused by the presence of an interface between Fe and Co planes has been pointed out recently [240–242]. The reduced dimensionality observed in Fe/Co superlattices causes a large magnetic anisotropy in the direction of the interface between Fe and Co.

The 3d–4d/5d alloys CoPt and CoPd A large number of experimental and theoretical investigations on bulk/thick films (Pd [243], Pt [209]), multilayers (Pd [244–260], Pt [261–265]), thin films (Pd [266–271], Pt [191, 205, 272–276]), clusters (Pd [277], Pt [278]) and adatoms on surface (Pd [279], Pt [34, 280, 281]) have demonstrated that CoPd and CoPt alloys are good candidates for perpendicular magnetic recording. Mainly, three kinds of effects giving rise to an enhancement of the perpendicular magnetic anisotropy highlight the role played by the local atomic environment on the magnetic properties. In the following, I illustrate these effects with examples issued from literature.

- Bulk alloy effect : Compared to bulk hcp Co, CoPt alloying in the bulk-ordered L1_0 phase results in a 20 times larger MAE up to 1 meV/Co atom [209] (and references therein), owing to the strong spin-orbit coupling of the Pt 5d states.

- Surface alloy effect : Robach *et al.* have pointed out intermixing induced spin reorientation on very thin Co layers on Pt(111) [191]. Site exchange affecting up to 4% of the interface atoms is seen as sufficient to reverse the magnetization of a film around 6 atomic layers from in-plane to out-of-plane. The strong anisotropic 3d – 5d hybridization between Co and Pt and the enhancement of the number of Pt-Co bonds along the surface normal due to the exchange between Co and Pt atoms cause the

easy axis to rotate out-of-plane.

- Interface effect : an enhancement of perpendicular magnetic anisotropy (PMA) has equally been observed in multilayers and thin films. A strong and localized interfacial $3d-4/5d$ hybridization produces an enhanced perpendicular Co orbital moment responsible for the high PMA. Dorantes-Dávila *et al.* has used a tight-binding Hamiltonian approach to estimate the contribution brought by the presence of an Co-Pd interface to the MAE. They found a magneto-crystalline energy of 0.3 meV/atom associated with this interface. They predict equally an enhancement of the magnetic moment of Pd to $\mu_{Pd} \approx 0.3 - 0.45 \mu_B$ [259, 282].

The effect of interfacial electronic hybridization with the substrate is well exemplified by the magnetic behavior observed for surface-adsorbed individual atoms. Giant magnetic anisotropies of 9.3 ± 1.7 meV/atom have been found for single Co atoms on Pt(111) [34], a $5d$ transition metal, while vanishing MAE values have been observed for single Co atoms when deposited on alkali metals, where only $3d-sp$ hybridization is possible [283]. In addition to electronic change via hybridization, in thin films the lattice mismatch between film and substrate can induce modifications of the crystallographic translational symmetry, which can result in additional modifications of the magnetic properties [129].

4.1.2 Growing core-shell nanostructures

For many elements the preparation of bi-metallic core-shell islands is non-trivial due to the tendency of insertion into the substrate or core, and the Ehrlich-Schwöbel barrier inhibiting descent of the shell element arriving on the core. An example for islands with a Pt core and a Co rim on Pt(111) performed by Weiss *et al.* is illustrated in Fig. 4.2 [6, 284].

The desired density and size of the core are defined by deposition temperature and coverage, respectively. At the experimental deposition flux of $F = 0.02$ ML/min Pt/Pt(111) forms the desired density of $n_x = 2.5 \times 10^{-4}$ islands/unit cell at a $T_{dep} = 200$ K, as inferred from inserting the diffusion barrier and pre-exponential factor of that system [77, 285] into the scaling laws of nucleation [62]. Limited mobility along steps gives rise to fractal island shapes for that system up to $T_{dep} = 400$ K [286], see also Fig. 4.2(a). In order to get a compact core the islands have to be annealed. This also leads to coarsening implying a slightly lower deposition temperature for the first step. The ideal parameters for Pt/Pt(111) are deposition at 170 K, followed by annealing at 770 K leading to compact monolayer Pt islands with a quasi-hexagonal thermodynamic equilibrium shape [286], see Fig. 4.2(b).

A two to three atoms wide rim is created around the Pt core by deposition of 0.15 ML Co at 220 K, see Fig. 4.2(c). In the STM images, Co and Pt can be discerned by their apparent height difference of about 0.3 Å. The Co deposition temperature has

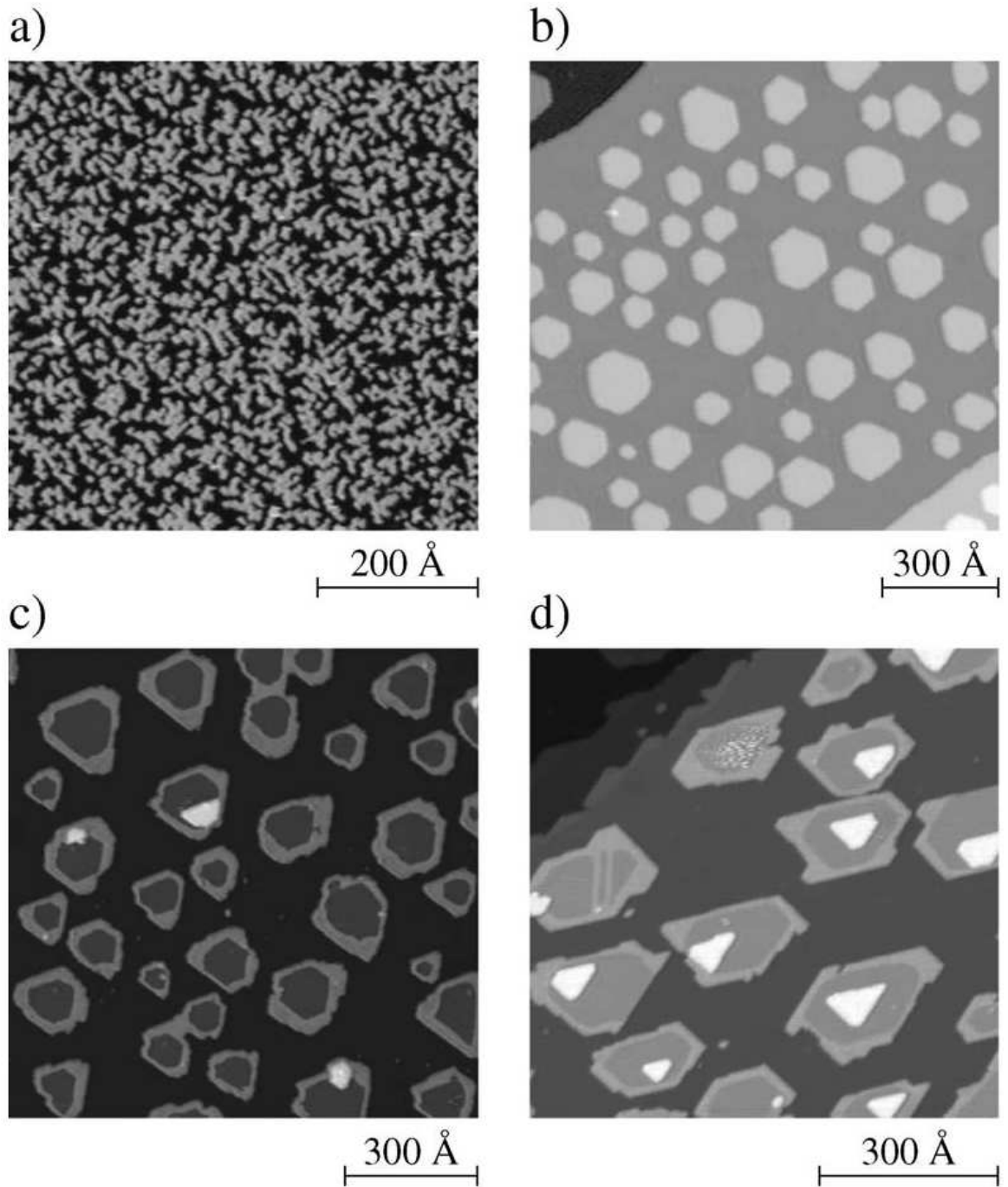


Fig. 4.2 – STM topographs illustrating the growth steps for the creation of islands with a Pt core surrounded by a Co rim. (a) Pt deposition at 130 K produces small fractal islands ($\Theta = 0.40$ ML). (b) Annealing to $T_{ann} = 770$ K transforms fractal islands into larger quasi hexagons ($\Theta = 0.25$ ML, $T_{dep} = 170$ K). (c) Co deposition at 220 K allows to decorate the Pt cores with thin Co rims ($\Theta_{Co} = 0.15$ ML). (d) Co deposition at slightly too high temperatures and on too large Pt cores causes Co insertion into Pt (see pair of dislocations on one Pt island) and second layer growth ($T_{dep,Pt} = 240$ K, $T_{ann} = 790$ K, $T_{dep,Co} = 250$ K) (from [6, 284]).

to be chosen high enough to inhibit nucleation of Co islands between and on-top of Pt islands. The first requirement is less stringent, one readily achieves $n_{x,Co} \ll n_{Pt-core}$, while the second requirement is in conflict with Co insertion into the Pt(111) surface starting at 180 K. The probability of second layer nucleation is essentially given by the Ehrlich-Schwöbel barrier [287–289] and has to be sufficiently low. Co insertion in the presence of Pt adatom islands takes place at slightly higher temperatures since the islands reduce the tensile stress of the Pt(111) surface. The temperature range constituting the best compromise between avoiding insertion and second layer nucleation is for the present system $200 \text{ K} \leq T_{dep,Co} \leq 260 \text{ K}$. Figure 15.11(c) shows that Co islands only occasionally grow on-top of the biggest Pt islands. The size of the Pt core and the deposition temperature are quite critical as illustrated in Fig. 4.2(d). Insertion of Co in the Pt core took place at one island on the left, as evidenced by the pair of parallel partial dislocations imaged bright. In addition, almost on all the cores small second layer nuclei can be observed.

The case of Co, Pd and Fe growth on Pt(111) In the previous example, we learn how the experimental determination of the growth parameters of Pt and Co (energy barrier for monomer diffusion, attempt frequency) allow building core-shell nanostructures with controlled shape, size and density. In the following, we have grown different kinds of core-shell nanostructures so as to study magnetic properties issued from the formation of an alloy and the creation of interfaces. To this purpose, we have used previous studies on nucleation and growth of metals on Pt(111) surface. The growth of Co/Pt(111) [78], Pd/Pt(111) [290] and Fe/Pt(111) (the second chapter of this thesis) were all studied on the same Pt sample under the same experimental conditions. The results on Pt homoepitaxy [63, 77, 285, 286, 291, 292] were also confirmed on our sample. Therefore, the growth parameters of the used elements were considered as perfectly known. Fig. 4.3 shows the Arrhenius plot of the stable island density versus the inverse temperature in the case of Co/Pt(111) (from [78]). From the growth experiment, Ph. Bulushek deduced a monomer diffusion of $200 \pm 10 \text{ meV/atom}$. This study reveals also that Co start insertion in the Pt substrate at around 180 K but the larger effects manifest above 300 K. The size and the shape of the Co islands upon varying deposition temperatures were analyzed. At 130 K, Co islands are ramified, whereas at 200 K, Co islands starts growing in a more compact triangular shape. Above 270 K, Co grows in double layers. Owing to experimental necessities (no coalescence between islands, large MOKE signal), we needed to grow compact Co nanostructures with a density of $2 \times 10^{-4} \text{ island/site}$. This could be achieved only by two-steps deposition. The first deposition step was at $T_{dep} = 150 \text{ K}$ to fix the island density, while the second deposition step was performed at $T_{dep} = 250 \text{ K}$ to ensure the more compact growth without formation of Co double layers.

Studies for Pd and Pt yield monomer diffusion energy of $300 \pm 10 \text{ meV/atom}$ [290] and $260 \pm 10 \text{ meV/atom}$ [285], respectively. At 250 K, Pt, Pd and Fe have a mean free diffusion path larger than the distance between Co islands which is a necessary condition to create core-shell structures.

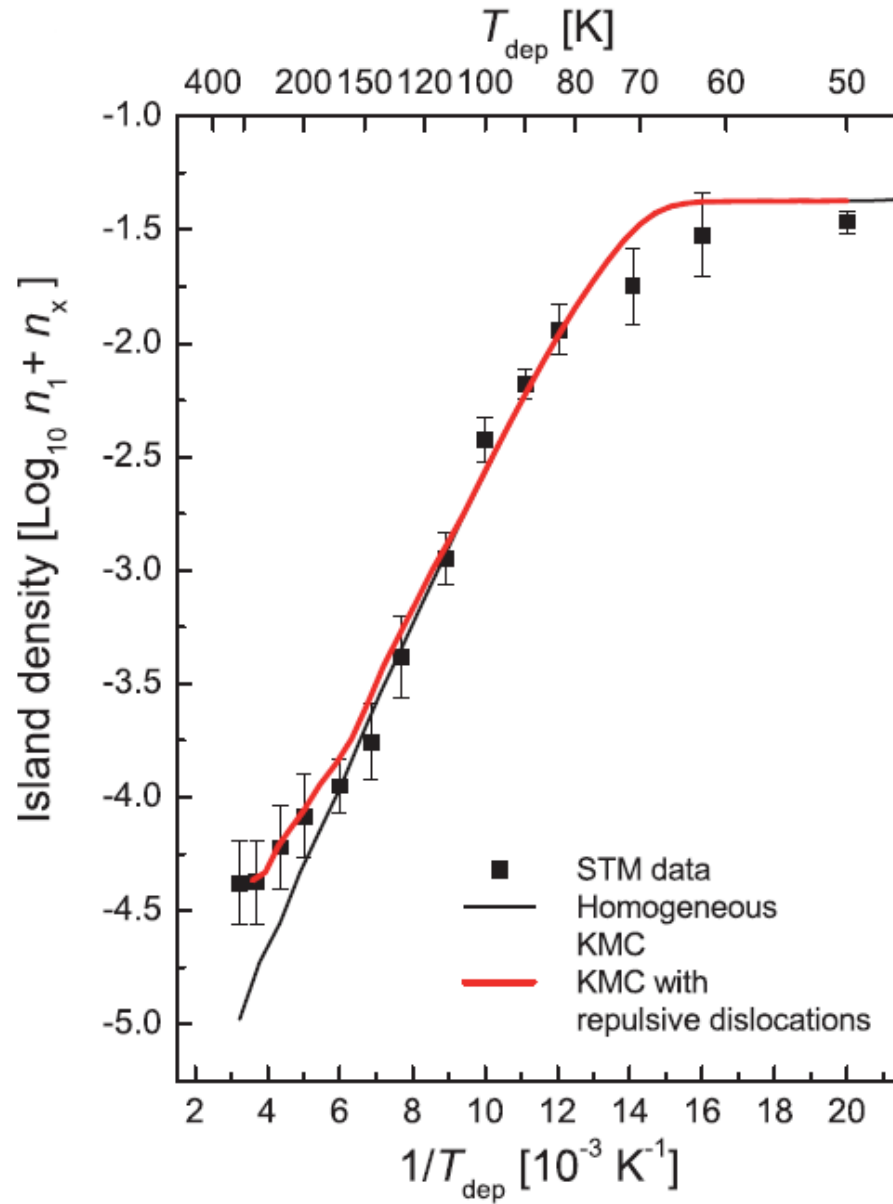


Fig. 4.3 – Arrhenius plot of the island density of 0.1 ML Co on Pt(111) obtained by KMC with repulsive and dynamically growing dislocations (red curve) and in the case of homogeneous KMC. Black dots : Experimental data. (from [78]).

4.2 Magnetism of FeCo rim around Pt core : the alloy effect

The magnetic properties created by alloying Co and Fe atoms have been investigated by Stefano Rusponi using a growth procedure similar to the one presented in Section 4.1.2. The results from this experiment are discussed here since they will be used in Section 4.3.

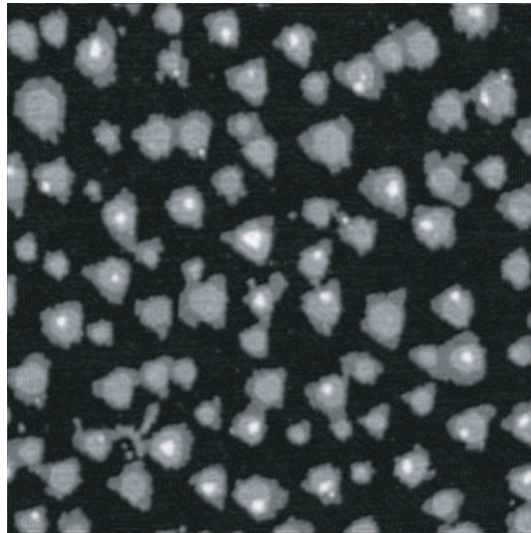
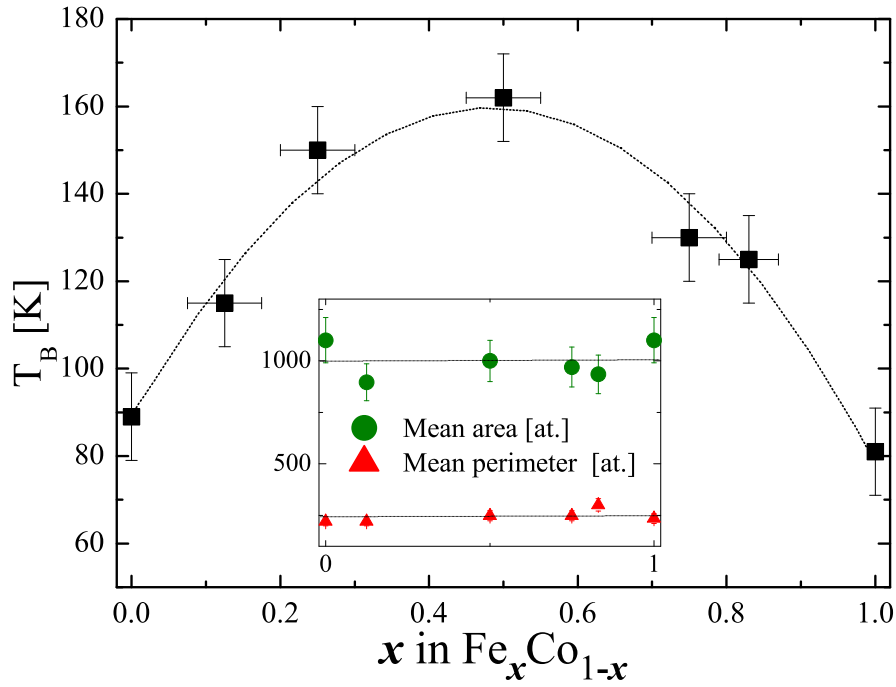


Fig. 4.4 – (top) Blocking temperature T_B as a function of the composition x in monolayer high $\text{Fe}_x\text{Co}_{1-x}$ -alloy shells surrounding Pt cores on a Pt(111) surface. The inset shows the mean shell area A_s and perimeter P_s to be independent of composition. The dotted curve is the T_B -variation according to the model discussed in the text. (bottom) $1400 \times 1400 \text{ \AA}^2$ STM constant current topograph of core-shell islands displaying the cores with slightly higher apparent height than the shells (core : $\Theta_c = 0.15 \text{ ML}$, $T_{dep} = 250 \text{ K}$, $T_{ann} = 800 \text{ K}$; shell : $x = 0.5$, $\Theta_s = 0.20 \text{ ML}$, $T_{dep} = 300 \text{ K}$).

The influence of the alloy composition on T_B is shown in Fig. 4.4(top). T_B increases by 200% for equal amounts of Fe and Co compared with pure Co or Fe. Before discussing this result in quantitative terms we note that for low-dimensional systems, it is not trivial to investigate this effect since the magnetocrystalline anisotropy is strongly affected by the atomic coordination [34, 128]. Simple co-deposition of the two elements was observed to lead to changes in morphology of the alloy islands as their composition was varied. These are caused by the different terrace and step edge diffusion barriers of the two elements, leading to composition dependent island densities and shapes, respectively. Both effects lead to a varying number and coordination of perimeter atoms for each composition [128]. In order to create alloy islands with a composition independent morphology compact Pt islands were used as nucleation sites onto which Fe and Co were co-deposited. Deposition of Fe and Co was performed at 300 K, where the mean free diffusion paths of the adatoms of both elements are sufficient to reach the Pt cores for the applied deposition fluxes. The composition was changed by varying the Fe and Co fluxes. This way monolayer high FeCo shells surrounding compact non-ferromagnetic Pt cores could be created. The coverage optimizing the magnetic signal of monolayer islands is limited by coalescence. For compact islands on trigonal substrates, first coalescence events appear at 0.2 ML but their number becomes significant only above 0.4 ML [62]. The total coverage was therefore chosen to be 0.35 ML and divided into $\Theta_c = 0.15 \pm 0.01$ ML and $\Theta_s = 0.20 \pm 0.03$ ML for core and shell, respectively. The STM contrast between core and shell in Fig. 4.4 (bottom) was used to determine the mean area A_s and perimeter P_s of the $\text{Fe}_x\text{Co}_{1-x}$ -shells from analyzing 1000 islands for each composition x with a routine added for this purpose to our image processing program. The inset of Fig. 4.4 (top) shows these quantities to be within the error bars independent of composition and the observed variation of the magnetic hardness reflects exclusively the alloy composition.

Results

The energy barrier E_b is linked to the blocking temperature through the relation $T_B = E_b/(k_B \ln \nu_0/f)$, where k_B is the Boltzmann constant, ν_0 is the attempt frequency for thermal magnetization reversal and in the range of $10^9 - 10^{12}$ Hz. It is observed that the variation of T_B over the whole composition range can be inferred from the superposition of a linear function going from pure Co to pure Fe shells and an inverted parabola describing the additional energy barrier due to the alloy effect. This yields the energy barrier for thermal magnetization reversal $E_{\text{alloy}}(x) = A_s(E_{\text{Fe}}x + E_{\text{Co}}(1-x) + E_a(1-4(x-0.5)^2))$. The curve shown in Fig. 4.4 (top) yields $E_{\text{Fe}} = 0.147 \pm 0.016$ meV/atom, $E_{\text{Co}} = 0.165 \pm 0.018$ meV/atom, and $E_a = 0.138 \pm 0.015$ meV/atom. The error bars result from assuming attempt frequencies of $\nu_0 = 2 \times 10^{10 \pm 1}$ Hz. The values for pure Fe and Co represent an average over all shell atoms. The shells are on average 5 ± 1 atoms wide. The outer atoms are step atoms and have energy barriers of 0.9 ± 0.1 meV/atom in the case of Co [128], and similar values for Fe as concluded by similar T_B -values for $x = 0$ and 1 in Fig. 4.4 (top). Note that the values above are averaged over the entire shell.

Discussion

We attribute the variation of T_B with the 200%-increase for $x = 0.5$ to the shell electronic structure rather than to a variation of strain or crystallographic ordering with x . From STM images it is seen that the shells have no dislocations for all compositions. Therefore the shell atoms are on pseudomorphic Pt(111) lattice sites and under tensile stress. The absence of dislocations is expected as the shell width is below the size where dislocation formation sets in in pure Co [188] islands, which is 50 to 80 Å. Pure Fe islands have no dislocations independent of size since Fe grows pseudomorphic up to completion of the first monolayer [44]. The chemical order in the alloy shells is very likely random due to growth by codeposition and at room temperature. Ordered alloys would in our case be alternate rows of Co and Fe and their preparation is expected to require annealing or growth temperatures far above 400 K, where alloy formation with the substrate sets in. For small 3D FePt particles the partial ordering into the L1₀-phase required annealing to 870 K [293] and thin films FePt on MgO(100) needed growth temperatures of 770 K in order to reveal the L1₀-order [294].

4.3 Magnetism of Fe, Co and Pt rim around Co core : the interface effect

Morphology

We now turn from the alloy effect on T_B to the magnetic hardness induced by a sharp Fe-Co interface and compare it to Pt-Co interface. We prepared 0.12 ML of monolayer high Co core islands which were subsequently decorated by Co, Fe or Pt atoms (referred as shell atoms). To avoid evolution of the magnetic properties due to contamination from the residual gas [188, 295] a fresh sample has been prepared for each Θ_s . We limited ourselves to $\Theta_s \leq 0.15$ ML since coalescence sets in earlier for ramified islands [62]. The deposition temperatures were again chosen such that the mean free diffusion paths of the shell atoms were larger than the mean distance between Co cores. Fig. 4.5(a) presents a STM topograph of the Co cores before decoration. The different kinds of decoration is shown in Figs 4.3 (b) Co, (c) Fe and (d) Pt. The growth procedure permits us to keep constant the island densities to $1.9 \pm 0.3 \times 10^{-4}$ islands/site for all samples. The error bar within the same kind of samples was reduced to 0.15×10^{-4} islands/site.

4.3. MAGNETISM OF FE, CO AND PT RIM AROUND CO CORE : THE INTERFACE EFFECT

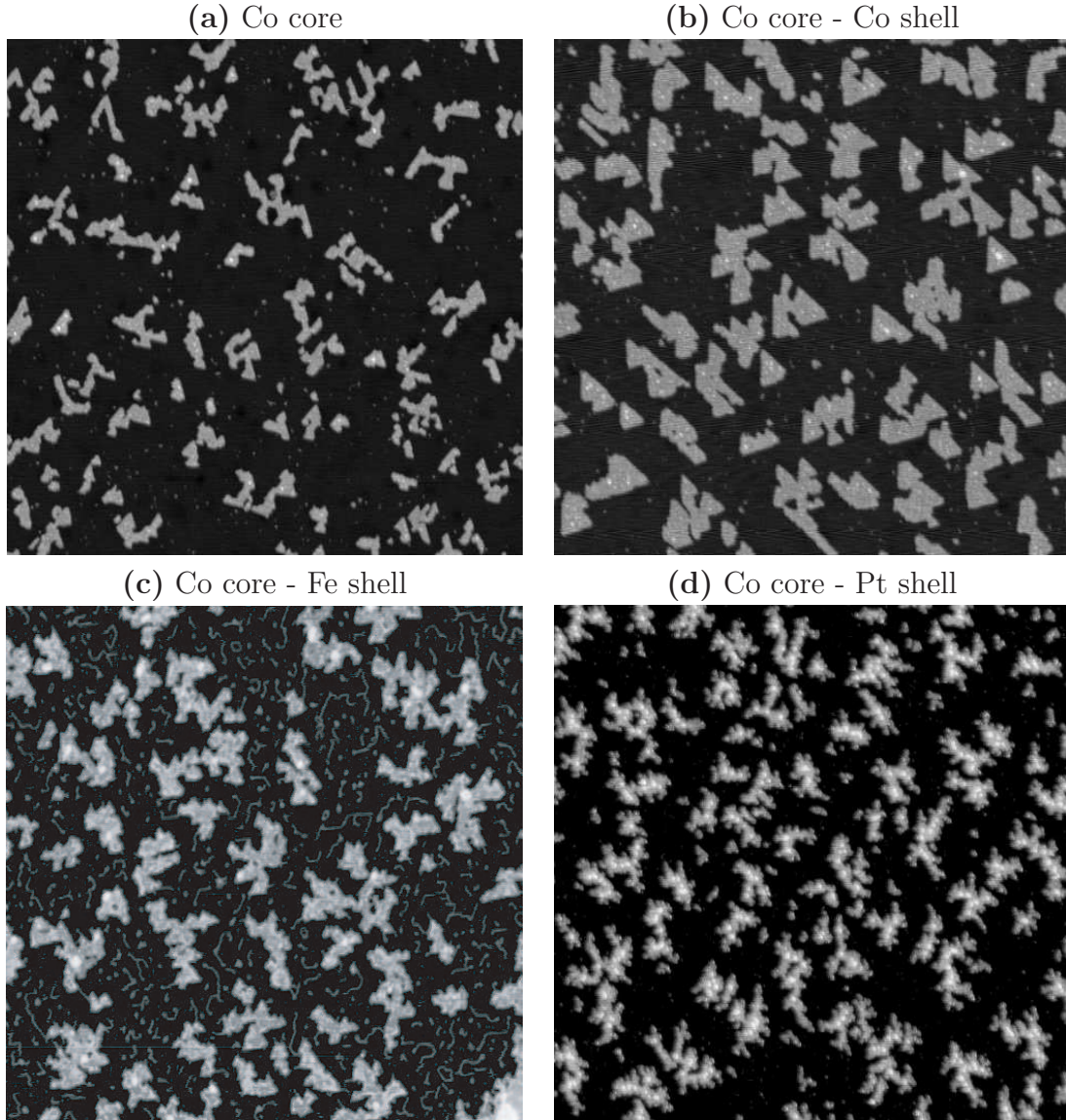


Fig. 4.5 – STM topographs of core-shell islands with Co cores. (a) size : $1800 \times 1800 \text{ \AA}^2$, Co cores without decoration ($\Theta_c = 0.12 \text{ ML}$, $T_{dep,c} = 150 \text{ K}$); (b) size : $1800 \times 1800 \text{ \AA}^2$, Co cores surrounded by Co shell ($\Theta_s = 0.15 \pm 0.02 \text{ ML}$, $T_{dep,s} = 250 \text{ K}$); (c) size : $2000 \times 2000 \text{ \AA}^2$, Co cores surrounded by Fe shell ($\Theta_s = 0.135 \pm 0.02 \text{ ML}$, $T_{dep,s} = 250 \text{ K}$), the contrast has been chosen to emphasize the difference between Co and Fe. Fe wires are also visible. A thermal drift in the up-down direction slightly distorts the image. (d) size : $2000 \times 2000 \text{ \AA}^2$, Co cores surrounded by Pt shell ($\Theta_c = 0.21 \text{ ML}$, $T_{dep,c} = 150 \text{ and } 250 \text{ K}$, $\Theta_s = 0.075 \pm 0.02 \text{ ML}$, $T_{dep,s} = 250 \text{ K}$). Pt in top of the Co layer represents 0.015 ML .

Co and Fe shell The morphology of Co and Fe decorated Co cores is presented in Fig. 4.5 (b) and (c) in the case $\Theta_s = 0.15 \pm 0.03$ ML and $\Theta_s = 0.135 \pm 0.03$ ML, respectively. We have observed that the morphology of the two kinds of islands is very similar. At low coverage, the islands appear ramified and they compactify with increasing shell coverage. In samples with Fe decoration, we have observed the Fe wires already presented in Chapter 2. The general trend was an increase of their density with Fe coverage. Their coverage can be estimated from a direct comparison with the results presented in Chapter 2 around 0.02 ± 0.01 ML at the largest Fe coverage.

Fig. 4.6 presents the mean perimeter of the pure and Fe-decorated Co islands as a function of the coverage in the shell. The general trend in both cases is an increase of the mean perimeter with the shell coverage in the range 150 – 250 atoms. Similar variations have been observed for the island mean sizes of the different kinds of samples. Note that the x-error bars have been suppressed since the relative error on the determination of the coverage is the same. The absolute error should be ± 0.03 ML as indicated previously. The vertical error bars are inferred from an estimate of the tip convolution effect and from the number of islands that have been analyzed.

Fig. 4.7 is a $500 \times 500 \text{ \AA}^2$ high resolution STM topograph showing chemical resolution between Fe and Co. In this image, 0.15 ML of Fe were deposited around Co cores representing 0.12 ML. Fe appears as bright zone with relative height 0.40 \AA higher than Co (see, linecuts in the figure). The highest spots on top of some Co islands with relative height of 2.35 \AA (see the green linecut) is interpreted as Fe clusters formed upon deposition. The amount of these clusters is estimated to be less than 0.01 ML in all samples. The bright lines with a relative height 0.25 \AA (see the red linecut) correspond to the so called reconstruction lines characteristic of the first Co layer on Pt(111). The presence of these reconstruction lines supports that no insertion of Fe in Co cores occurs. This result can be seen as a consequence of the high cohesive energy of both Co and Fe nanostructures [296, 297]. The main result from the chemical resolution images is that Fe grows irregularly around Co cores. We observe Fe stripes until around 5 atom width ($\approx 12 \text{ \AA}$) surrounding Co cores. We could roughly estimate that $77 \pm 15\%$ of the Co edge were surrounded by Fe in the case represented in Fig. 4.7.

Pt shell In the case of Pt decoration, we have grown Co islands with $\Theta_c = 0.19 \pm 0.03$ ML and with equal island density that in the case of Co and Fe decoration. Fig. 4.5 (d) shows the morphology of such Co cores surrounded by $\Theta_s = 0.075 \pm 0.020$ ML Pt shell. The coverage of atoms on top of the Co layer was measured around 0.015 ML. An accurate measurement of the amount of atoms on top of the Co layer could not be performed for each sample but our observations suggest that Pt atoms landing on top of the Co islands do not descend onto the Pt(111) surface. A homogeneous ramified shape is observed for all the islands in Fig. 4.5 (d). This shape is characteristic of the Pt homoepitaxy grown at 250 K and is explained by a low edge mobility of Pt adatoms around Co islands. The evolution of the mean perimeter with the Pt coverage follows the same constant increase trend reported in the case

4.3. MAGNETISM OF FE, CO AND PT RIM AROUND CO CORE : THE INTERFACE EFFECT

of Co or Fe shell. However, the STM resolution did not allow to measure the island perimeter with sufficiently accuracy to give reliable values.

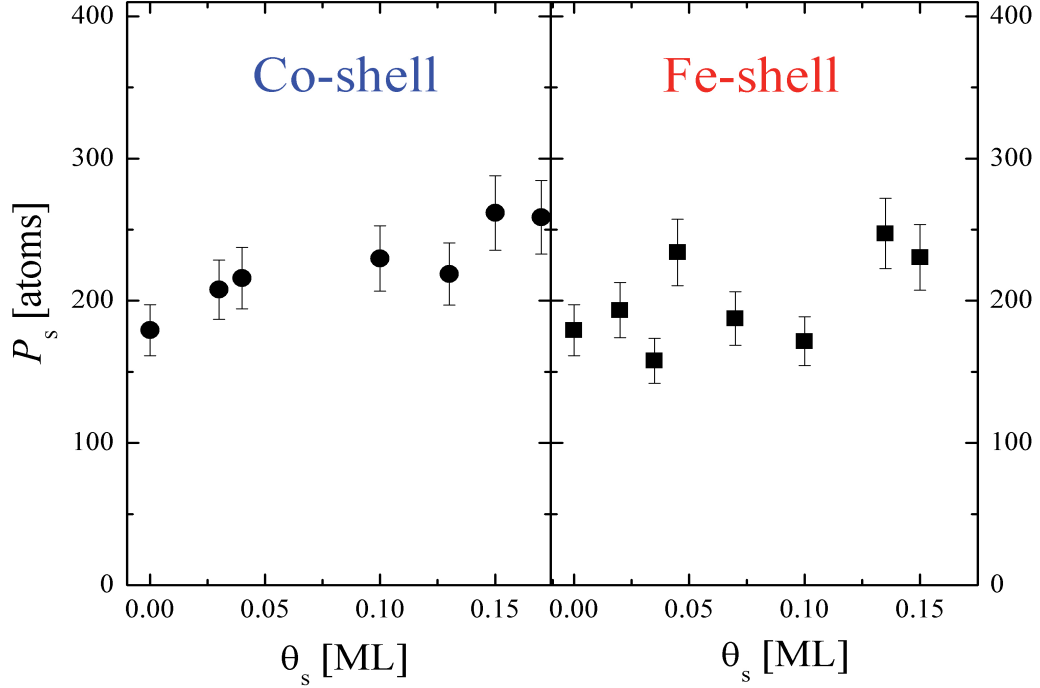


Fig. 4.6 – Mean shell perimeter P_s as a function of the shell coverage Θ_s in the case of Co (left) and Fe (right) decoration.

Magnetic results

The variation of the blocking temperature versus the shell coverage is presented in Fig. 4.8 (left) for Fe-, Co- and Pt-shells. Pure Co islands show a slight increase of T_B as a function of Θ_s . The variation of T_B with Θ_s is similar with the one of the island perimeter presented in Fig. 4.6. This result is in perfect agreement with previous results from Rusponi *et al.* on a similar system [128]. The authors outlined the predominant role of the low coordinated outer atoms on the magnetic anisotropy energy.

Co-Fe interface Adding a few percent of a monolayer of Fe significantly affects T_B . We observe a steep linear increase of T_B until $\Theta_s = 0.07$ ML, where T_B almost doubles its initial value. At higher coverage, T_B keeps increasing linearly to a first approximation, but with a much smaller slope. From the mean core perimeter and the island density we infer a mean number of monatomic Fe chains surrounding the Co core. The change in slope takes place at the estimation of two atomic rims. This result can be a consequence of the irregular decoration already mentioned that delay the limit coverage corresponding to a change in the slope of the curve. An other

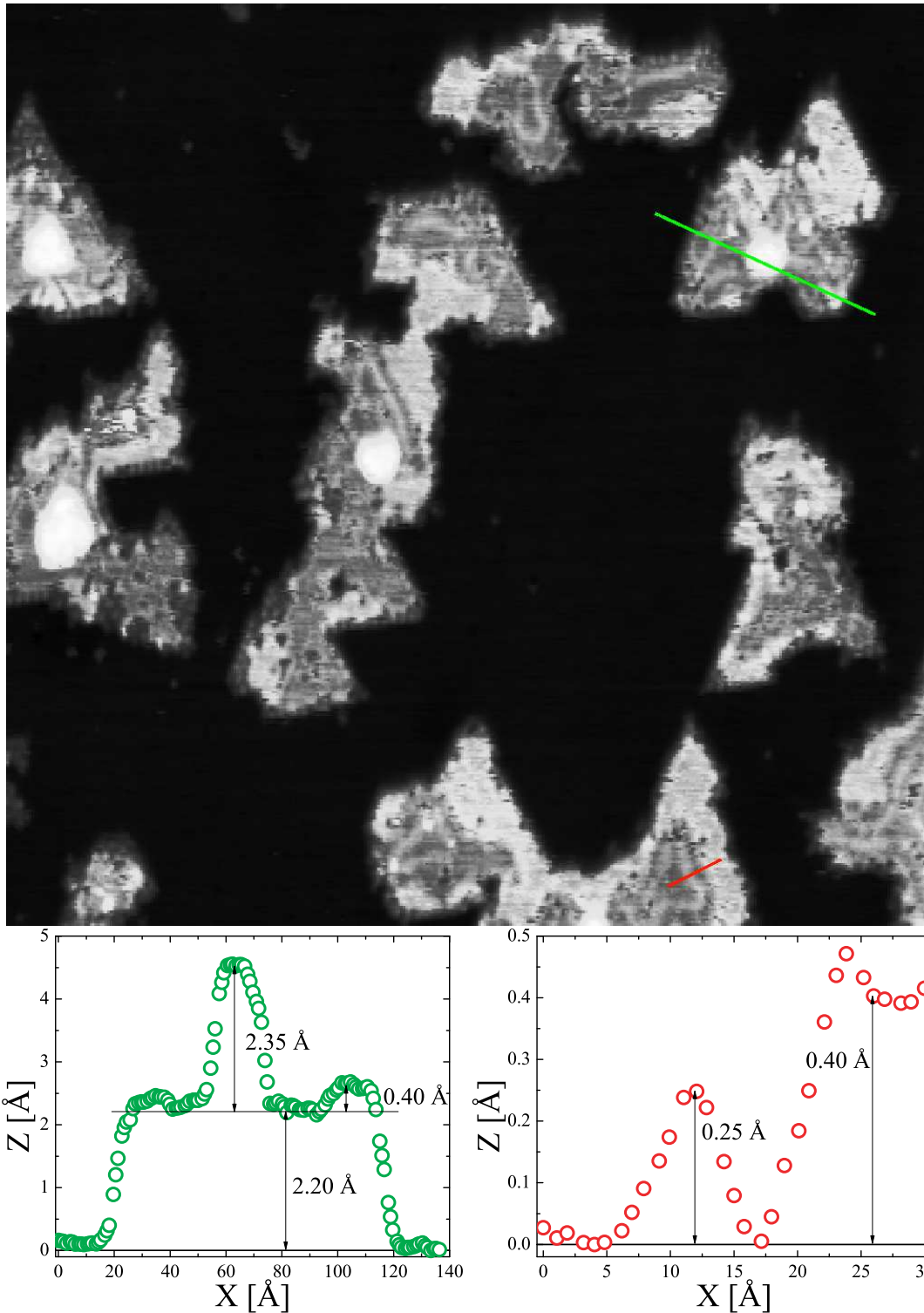


Fig. 4.7 – (top) $500 \times 500 \text{ \AA}^2$ STM topograph of Co core Fe shell islands displaying chemical resolution between Fe and Co atoms. Reconstruction lines are visible on Co cores. The Fe atoms surround partially the Co core. Fe atoms in top of the first layer represents 0.01 ML. (bottom) Two height profiles along the green and red linecuts show the height of an Fe cluster on a Co island and the relative height of a reconstruction line closed to the Fe shell, respectively ($\Theta_c = 0.12 \text{ ML}$, $T_{dep,c} = 150 \text{ K}$, $\Theta_s = 0.15 \pm 0.02 \text{ ML}$, $T_{dep,s} = 250 \text{ K}$).

4.3. MAGNETISM OF FE, CO AND PT RIM AROUND CO CORE : THE INTERFACE EFFECT

explanation might be that the magnetic interface effect appears only if the interface atoms are not at the same time low-coordinated step atoms. We note that blocking temperatures of 175 K can be achieved by a two atom wide Fe shell whereas pure Co islands of the same size and morphology have only 115 K. A rough expression in terms of interface and step energies for thermal magnetization reversal can be written in the case where the interface is fully established. There $E_b = p_s E_{p,Fe} + p_c (E_i - E_{p,Co})$, where p_s and p_c are mean shell and core perimeter lengths and $\Delta E_i = E_i - E_{p,Co}$ is the extra energy induced by the creation of a Fe-Co interface of one atom length, for which we find $\Delta E_i = 0.9 \pm 0.2$ meV/atom. This value is much larger than the one of the alloy suggesting that for Fe and Co atoms the creation of an interface rather than the formation of an homogeneous alloy may lead to magnetically harder particles for a given size.

discussion A number of approximations that have been made in order to estimate ΔE_i will be discussed in the following.

- Atoms in second layer : we have neglected the contribution brought by the atoms on top of Co islands to T_B . The low concentration around 0.01 ML of clusters on top of Co islands suggests that these clusters do not contribute significantly to the magnetic properties. Moreover, the presence of clusters is not detected on all islands resulting into two kinds of population of islands. A strong enhancement of T_B associated with the presence of these clusters would result in a clear double peak in $\chi(T)$ curves [184], which was not observed. Finally, we did not observe a particular trend of T_B with the coverage of atoms in second layer.

- presence of Fe wires : a fast estimation of the contribution of a few atom size structure to $\chi(T)$ curves has been made in Chapter 1. The estimated blocking temperature for such systems with high anisotropy but small size is one order of magnitude smaller than the blocking temperature of the islands. Moreover, the contribution to $\chi(T)$ curves is proportional to M^2 the overall magnetization to the square. M represents the sum of all the magnetic moment of the atoms of the nanostructures. The magnetic moments of 1D structures is expected to increase compared to the case of 2D structures. Nevertheless, the order of magnitude remains the same. Therefore, the contribution to $\chi(T)$ of a wire composed by few atoms is many orders of magnitude smaller than the contribution of an island composed by hundreds of atoms. From this, it is straightforward to neglect any contributions from the Fe wires to the $\chi(T)$ curves.

- The irregular decoration observed in some STM topographs with high Fe coverage was not taken into account in this model. We could do so by assuming a decoration slightly favoring segregation of Fe and Co and assuming a low edge mobility of Fe atoms. The evolution of the free Co perimeter $p_{Co,free}$, i.e. the non decorated perimeter, would therefore depend on the proportion of Co perimeter already decorated by Fe $p_{Co,total} - p_{Co,free}$. This would result in an exponential law $p_{Co,free} = p_{Co,total} \exp -(\alpha \Theta_{Pd})$ yielding $\Delta E_i = 1.2 \pm 0.5$ meV/atom.

- Our model is based on the assumption that the magnetic properties of the ensemble of islands are the same as the magnetic properties of the mean island.

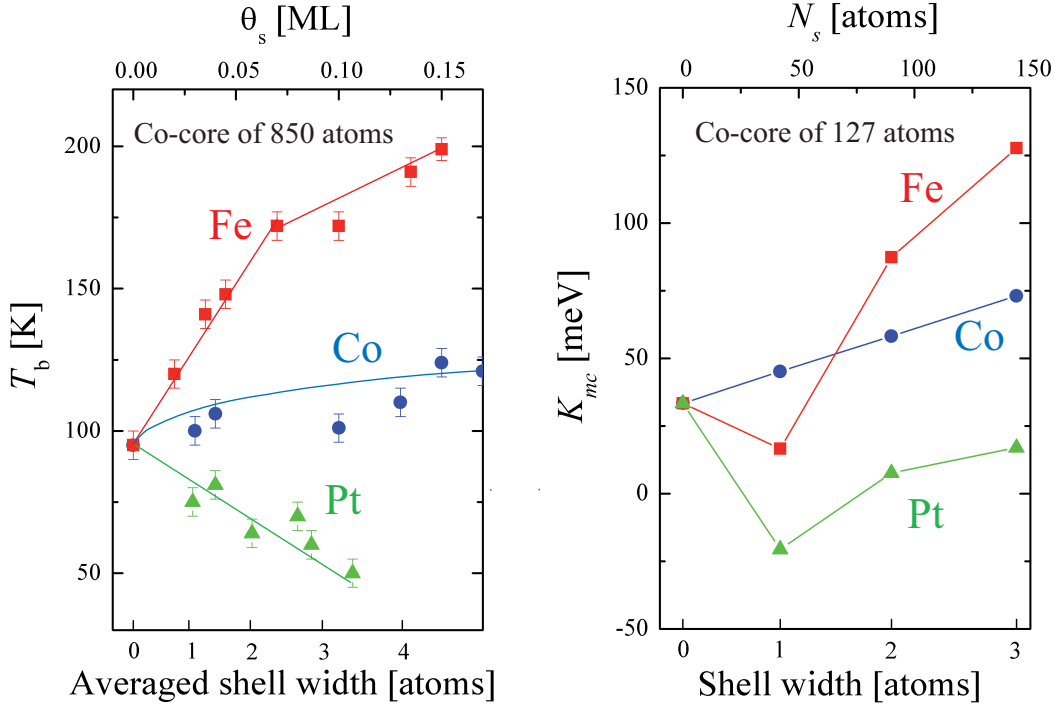


Fig. 4.8 – (left) T_B as a function of the coverage Θ_s in the shell for a Fe-shell (red squares), Co-shell (blue circles) and Pt-shell (green triangles) with $\Theta_c = 0.12$ ML. The estimated number of atomic rims corresponding to Θ_s is given as an indication. (right) Magnetocrystalline anisotropy energy K_{mc} calculated for an hexagonal Co core of 127 atoms decorated by 1 to 3 atomic rims of Fe (red squares), Co (blue circles) and Pt (green triangles).

Whereas this assumption can be fully justified in the case of Pt cores where the island size distribution is small due to the compact core shape, this is not true in the case of ramified islands. In this case, the largest island size distribution and the dependence of $\chi(T)$ with M^2 (see Chapter 3) give evidence that our simple model underestimate the characteristic perimeter and, therefore, slightly overestimate E_i . All together with the previously discussed approximations, our rough model gives good order of magnitude of the contribution due to the creation of an Fe-Co interface to the energy barrier for thermally activated magnetization reversal.

Co-Pt interface The formation of a Pt-Co interface leads to an opposite T_B -variation. By increasing the coverage of the Pt shell, T_B decreases progressively. For

4.3. MAGNETISM OF FE, CO AND PT RIM AROUND CO CORE : THE INTERFACE EFFECT

$\Theta_s = 0.10$ ML, T_B is reduced by 50%. The lowest measured T_B is the limit of our measurement temperature range. Up to 50K, no slope change can be seen on the curve. From our measurements we cannot clearly determine the limit coverage for the total completion of core decoration. Nevertheless, an order of magnitude -0.6 meV/atom can be estimated for the energy barrier per Pt-Co couple at the interface, assuming that the Co island is fully decorated at $\Theta_s = 0.07$ ML and that atoms in second layer do not contribute to lowering T_B .

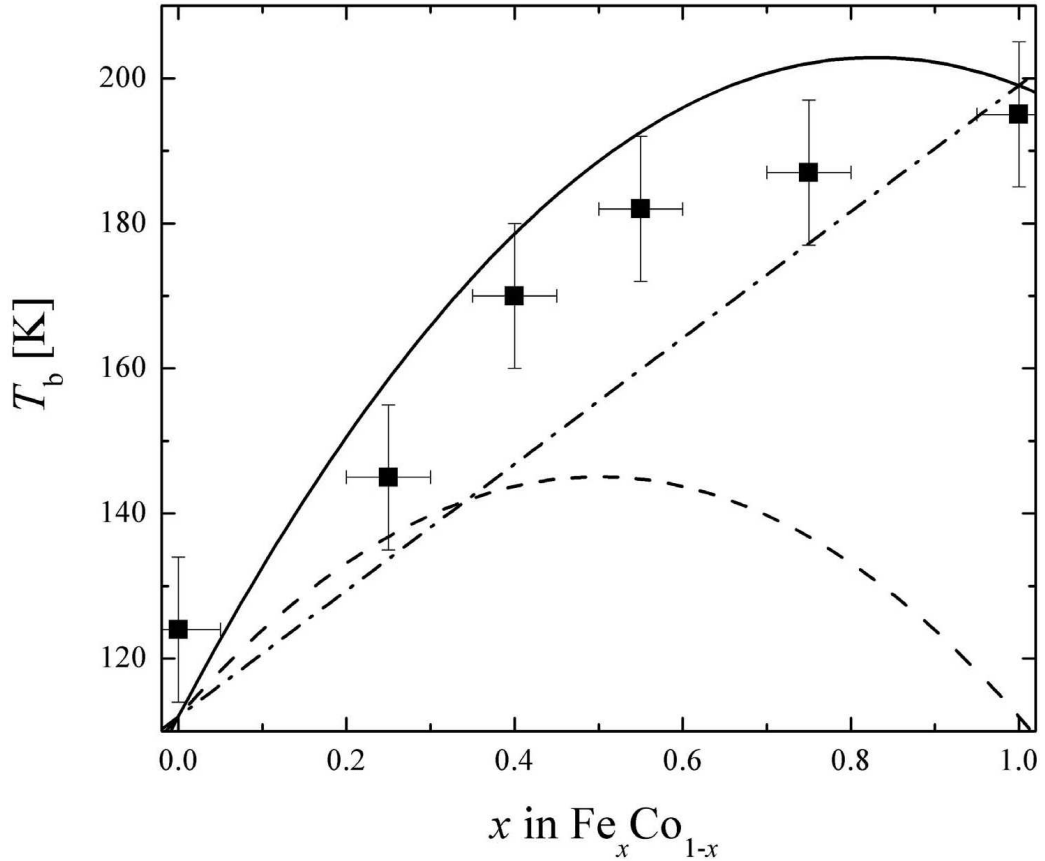


Fig. 4.9 – T_B as a function of the composition x in monolayer high $Fe_x Co_{1-x}$ -shells surrounding Co cores ($\Theta_c = 0.12$ ML, $T_{dep} = 150$ K, $\Theta_s = 0.27 \pm 0.03$ ML, $T_{dep} = 300$ K). The solid line shows $E(x)$ as described in the text. The dashed and dash dotted lines represent the alloy and the interface contribution, respectively.

Combining alloy and interface effect The consistency of our results and the large effect of the Fe-Co interface are illustrated in Fig. 4.9 where we have put alloy shells of varying composition around Co cores. The total coverage was kept constant to $\Theta = 0.39 \pm 0.03$ ML which corresponds to a shell width of 5 ± 1 atoms. T_B increases between $x = 0$ and $x = 1$. Varying x changes not only the alloy composition but also the Fe-Co interface length. For small x there are less Fe atoms available for creating the interface, while it develops its full length at $x = 1$. Now we can write for the

energy barrier for thermal magnetization reversal $E_b(x) = E_{\text{alloy}}(x) + xP_c\Delta E_i$, where the first term represents the alloy contribution with $E_{\text{alloy}}(x)$ as defined in the Pt core experiments. The second term is the interface contribution with xP_c the Fe-Co interface length. The curve resulting from the formerly determined values of E_{alloy} and ΔE_i accounts very well for the experimental data. From this, we can conclude that the Pt-Fe_xCo_{1-x} interface in Fig. 4.4 do not give a composition dependent contribution to the blocking temperature.

Agreement between experimental results and theoretical calculations

Our experimental results have been compared to *ab initio* calculations performed by Bornemann and coworkers from the Department of Physical Chemistry in Munich. Fully relativistic ab-initio SDFFT calculations were realized by applying a spin-polarized Korringa-Kohn-Rostoker (KKR) multiple scattering formalism in real space [298] to perfectly hexagonal one monolayer high islands deposited on a Pt(111) substrate [299]. Therefore, it was possible to estimate the magnetocrystalline anisotropy energy K_{mc} and the orbital moment anisotropy $\Delta_{\mu orb}$ for different core-shell single islands on Pt(111). K_{mc} was given by the difference in the total energy F between two directions of magnetization (in-plane and out-of-plane). $\Delta_{\mu orb}$ was the estimate difference of orbital moment between the two same directions of magnetization. The calculations have been performed for a single hexagonal cluster with varying size from 1 to almost 300 atoms with the most simple realistic structure. A pseudomorphic arrangement of the island atoms was assumed in agreement with the experimental observations as discussed above. No relaxation between the last Pt-layer and the islands and even for the outermost shell were taken into account. In 2D islands, the stress may partly be relieved by relaxation at the edge [300]. Our measurements do not allow to quantify such relaxation, we therefore know that the results for K_{mc} contain a systematic error and focus on the variation of K_{mc} with the size and the chemical configuration. The evolution of the total magnetocrystalline anisotropy energy K_{mc} of Co islands upon progressive decoration by Fe, Co or Pt atoms is presented in Fig. 4.8 (right). The number of atomic rims in the shell is increased from 1 to 3 and the corresponding total number of atoms in the island varies from 127 to 271. For a pure Co island, K_{mc} varies progressively from 33 to 73 meV. The decoration of the Co island with one atomic Fe rim leads to a reduction of K_{mc} , followed by a large enhancement when 2 and 3 atomic rims are considered. With 3 atomic Fe rims, K_{mc} is multiplied by 3.8 as compared to the case of the pure Co island. The effect of one Pt rim is to decrease K_{mc} up to a negative value. With 3 atomic Pt rims, K_{mc} amounts to 25% of the value for a pure Co island with the same size.

4.3. MAGNETISM OF FE, CO AND PT RIM AROUND CO CORE : THE INTERFACE EFFECT

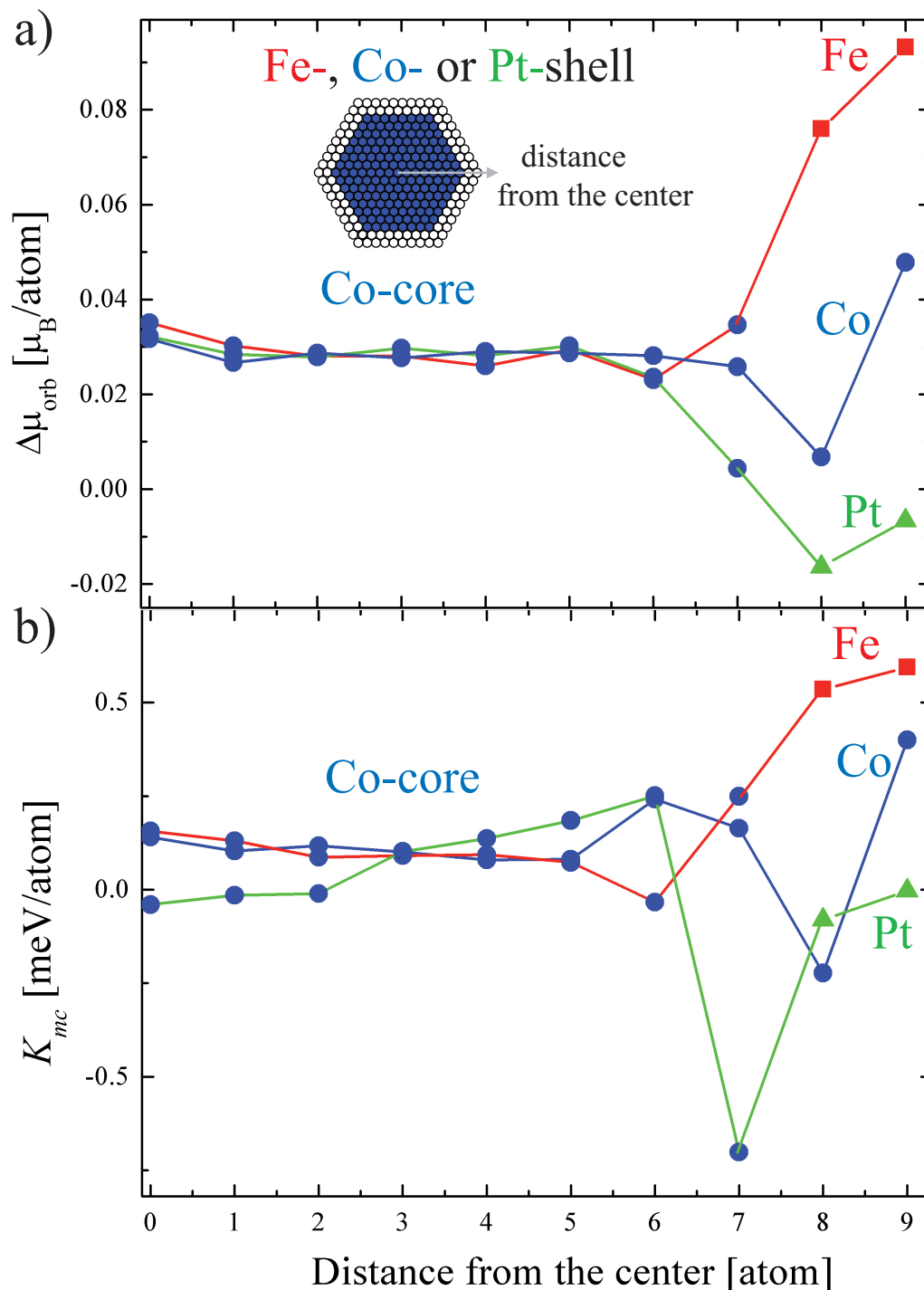


Fig. 4.10 – (top) Shell resolved atomic anisotropy of the orbital moment $\Delta\mu_{orb}$ for Co-core of 169 atoms surrounded by two atomic rims of Fe (red squares), Co (blue circles) and Pt (green triangles). (bottom) Atomic magnetocrystalline anisotropy energy K_{mc} for the same islands with the same color code. The distance from the central Co atom is given in atom and corresponds to the hexagonal shells of equivalent atoms.

Discussion

These element specific features of the calculated K_{mc} are very similar to the ones shown by the measured T_B and it is tempting to compare both quantities quantitatively. Before doing this, we remind the required assumptions for this comparison. For an individual island, the blocking temperature writes $T_B = E_b/(k_B \ln(\nu_0/f))$, where ν_0 is the attempt frequency for thermal magnetization reversal and in the range of $10^9 - 10^{12}$ Hz [301, 302]. E_b is the energy barrier between the two low-energy states for the magnetization and is related to the total magnetic anisotropy energy K through the general formula $E_b = \alpha K^\beta$. The coefficients α and β depend on the reversal mechanism for the magnetization. For coherent rotation $E = K = K_{mc} + K_{dip}$, while $\beta = 1/2$ is expected if reversal takes place by nucleation and propagation magnetic domain walls [301, 303, 304]. The shape anisotropy K_{dip} arises from the dipolar interactions between the magnetic moments and is not expected to significantly vary here with the composition. Though the knowledge of the power-law relating T_B and K_{mc} would require further investigations, we compare quantitatively E_b and K_{mc} for islands with the same size and shape after discussing the spatial dependence of the calculated K_{mc} .

The analysis of the experimental energy barriers has been realized in term of perimeter E_p and interface E_i contributions localized on the atoms at the border of the islands or at the interfaces. The description of these local contributions to the total E is equivalent to the Neel contribution in thin film anisotropy, attributed to the interface between two different materials or to the vacuum. The validity of this analysis is here quantitatively discussed, regarding spatially resolved calculated K_{mc} and $\Delta_{\mu orb}$. Fig. 4.10 presents the spatial dependence of K_{mc} and $\Delta_{\mu orb}$, plot as a function of the distance from the central Co atom. The abscissa-axis corresponds to the different atomic shells, starting from the central Co atom up to the outermost ninth shell of a perfect hexagonal island, corresponding to a total size of 271 atoms. The bottom curve presents K_{mc} of Co core of 169 atoms with two atomic rims of Fe, Co and Pt. Inside the island, K_{mc} is similar for the different clusters, up to the sixth shell, and varies slightly between 0.0 and 0.2 meV per atom. For the outermost three shells, the values strongly depend on the material decorating the island. For Fe, K_{mc} reaches 0.6 meV whereas the maximal value in the case of pure Co corresponds to the outer atoms while the penultimate shell has even negative K_{mc} . In the case of Pt, the two outermost Pt shells have K_{mc} around 0 and the seventh Co shell is decreased down to -0.7 meV. We note that $\Delta_{\mu orb}$ (top curve of Fig. 4.10) has a similar spatial dependence. The similar behaviors of K_{mc} and $\Delta_{\mu orb}$ is the consequence of the common physical origin by spin-orbit coupling as predicted theoretically by Bruno [126] and van der Laan [127], for 3d transition metals. Nevertheless for some points even the sign is changing between both quantities. This could be a consequence of the hybridization of 3d and 5d character, as previously mentioned. This spatially resolved investigation underlines that the presence of an interface in a core-shell island affects significantly and locally the magnetic properties, in an element-specific way.

4.4 Magnetism of CoPd nanostructures

In this section, we present results on the system composed by monolayer bimetallic Co-Pd nanostructures. We focus on two contributions to the magnetic anisotropy which are due to the creation of sharp lateral and vertical interfaces between Co and Pd. First, we discuss the same kind of core-shell structures described previously. Then, we report on statistic deposition of Pd around Co islands. These two systems combined with a realistic model based on interface contribution to the magnetic anisotropy give quantitative insight to a microscopic understanding of the origin of magnetocrystalline anisotropy in bimetallic alloy.

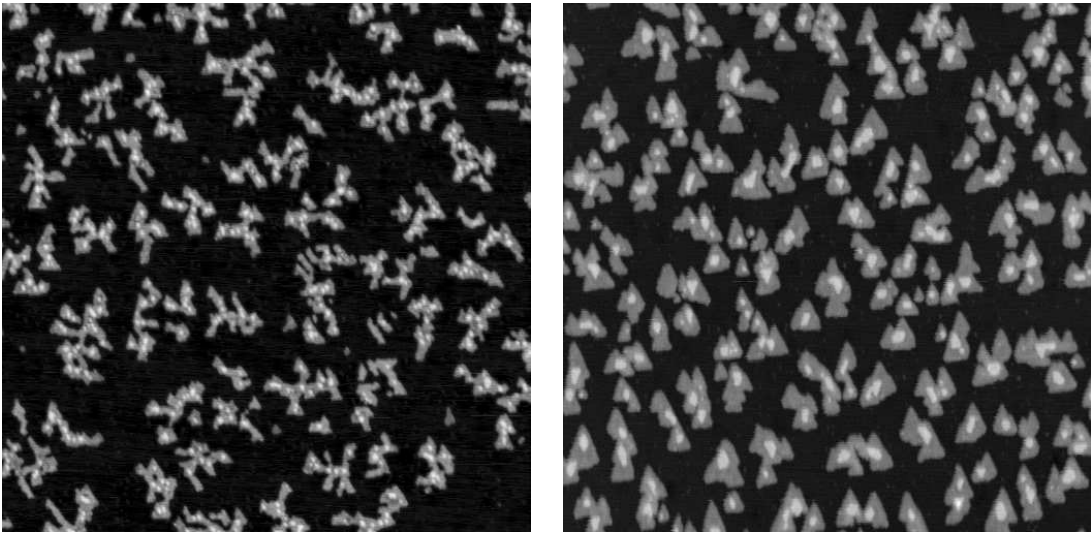


Fig. 4.11 – $2000 \times 2000 \text{ \AA}^2$ STM topographs of core-shell islands with Co cores ($\Theta_c = 0.19 \text{ ML}$, $T_{dep,c} = 150$ and 250 K) decorated by $0.08 \pm 0.02 \text{ ML}$ (left) and $0.19 \pm 0.02 \text{ ML}$ (right) of Pd ($T_{deposition} = 250 \text{ K}$). Pd in top of the first layer represents $0.009 \pm 0.005 \text{ ML}$ and $0.025 \pm 0.005 \text{ ML}$ for the left and right image, respectively.

4.4.1 Magnetism of Co islands decorated by Pd

Morphology The same experimental protocol that has been presented in the previous sections is used to grow monolayer high Co islands subsequently decorated by Pd atoms. The nominal Co coverage is $0.19 \pm 0.03 \text{ ML}$ in all cases. The deposition temperature for Pd was $T_{dep,Pd} = 250 \text{ K}$ to ensure a mean free diffusion path larger than the mean distance between Co cores. We have deposited between $0.085 \pm 0.03 \text{ ML}$ and $0.27 \pm 0.03 \text{ ML}$ of Pd. The pressure during deposition never exceeded $1.2 \times 10^{-10} \text{ mbar}$. The deposition was followed by a 5 minute annealing at 250 K and cooled down to 200 K during STM characterization. In Fig. 4.11, two $2000 \times 2000 \text{ \AA}^2$ STM topographs correspond to a Pd coverage of 0.085 ML (left) and 0.19 ML (right) decorating Co islands. On all the samples the island density was kept constant to $2.2 \times 10^{-4} \pm 0.4 \times 10^{-4} \text{ island/site}$. The addition of Pd over the surface

compactifies the island shape and tends to form trigonal islands. The presence of Pd in second layer was detected on all samples. It was observed that the coverage of Pd in second layer varied linearly with the total Pd coverage from 0.01 ML to 0.05 ML. We note that the measured coverage of the atoms in second layer is slightly smaller than the coverage estimated by a hit-stick model where the adatoms landing on the top of the Co islands cannot descend onto the Pt surface. Since Pd clusters are observed on the top of the Co islands, we deduce that "on island"-diffusion was activated in contrary to the step-down diffusion. In other words, the so-called Ehrlich-Schwobel barrier [305–307] of step-down diffusion is mainly not overcome at 250 K in the Pd/Co/Pt(111) system.

Fig. 4.12 (left) shows the blocking temperature as a function of the total Pd coverage Θ_{Pd} in two cases : pure Co island and Co islands decorated by 0.09 ML of Pd. This coverage corresponds to the coverage where clusters on top of Co islands could be detected. Furthermore, the abscise refers to the coverage of Pd in second layer $\Theta_{Pd,2^{nd}}$. The distinction between the two kinds of coverage was made to emphasize the different roles played by the lateral and vertical interfaces between Co and Pd in the variation of T_B (see Fig. 4.12 (right)). The blocking temperature in the case of pure Co island was measured to be 100 K. At the onset of the detection of Pd in second layer $\Theta_{Pd,2^{nd}} = 0.009 \pm 0.01$ ML the blocking temperature is 80 K. Therefore, the foremost effect on the magnetic hardness caused by Pd decoration is to lower it. We attribute this decrease to the creation of a sharp lateral interface between Co and Pd. Above this coverage, the blocking temperature increases linearly with $\Theta_{Pd,2^{nd}}$ until 136 K for $\Theta_{Pd,2^{nd}} = 0.052$ ML.

Discussion

We have developed a quantitative expression of the energy barrier for thermally activated magnetic reversal. This expression allows one to quantitatively determine the influence of the creation of lateral and vertical Co-Pd interfaces on the blocking temperature. Therefore, we distinguished E_{lat} , a contribution to the energy barrier due to the creation of a lateral Co-Pd interface, and E_{vert} corresponding to a vertical Co-Pd interface. We assume the lateral interface to be already complete after deposition of the 0.09 ML of Pd as sketched in Fig. 4.12. Therefore, we write the expression for the total energy barrier :

$$E_b = p_{Co,max}(E_{lat} - E_{Co,p}) + \frac{\Theta_{Pd,2^{nd}}}{\Theta_{Co}} s_{Co,max}(E_{vert} - E_{Co,s}) + E_{Co} \quad (4.1)$$

where E_{Co} refers to the total energy barrier for pure Co islands, $E_{lat} - E_{Co,p}$ and $E_{vert} - E_{Co,s}$ are the energy contribution per atom due to the creation of a lateral and vertical interface, respectively. $p_{Co,max}$ and $s_{Co,max}$ account for the Co island perimeter and surface (in atoms) giving the highest contribution to the imaginary part of the zero-field magnetic susceptibility of the sample. Therefore, to a first approximation, the measured value of the blocking temperature of the sample is equal to the blocking temperature of an island of size $s_{Co,max} \cdot p_{Co,max}$ and $s_{Co,max}$ were determined as

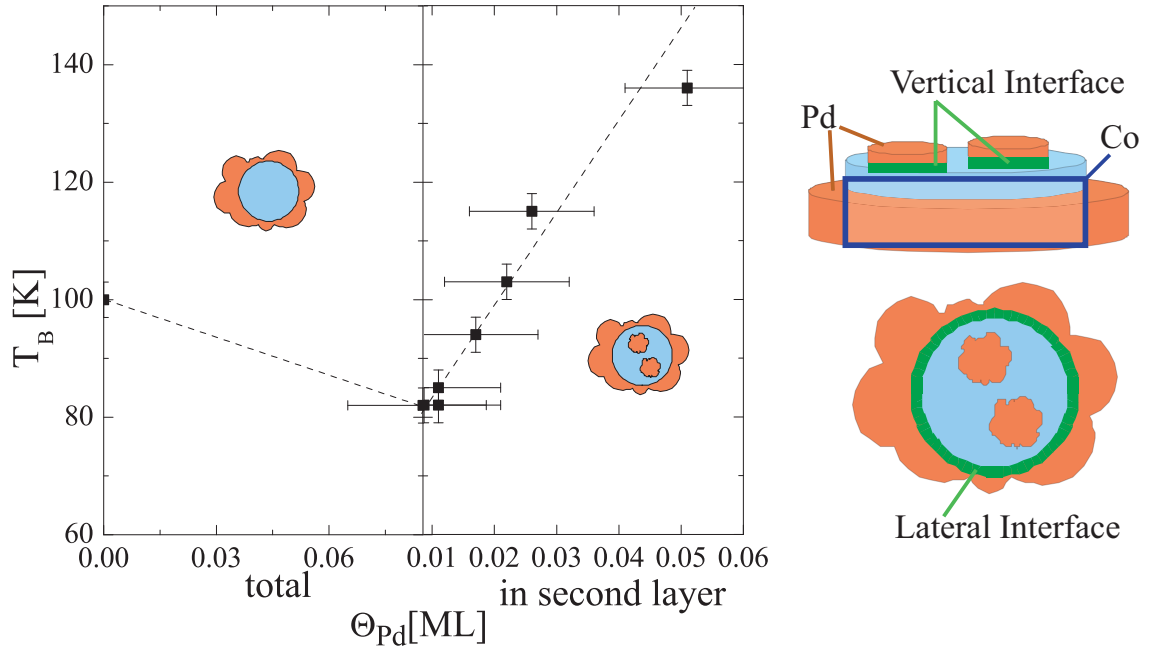


Fig. 4.12 – Blocking temperature T_B as a function of the total Pd coverage (left) and the coverage of Pd in second layer (right) in the case of Pd decorated Co cores on a Pt(111) surface. The dashed lines are guides to the eye. On the right is sketched a side and top view of an island showing the lateral and vertical interfaces between Co and Pd.

follow. From the size distribution $N(s)$ of pure Co island, we have inferred a relation between the maximum contribution to the $\chi(T)$ signal for each island as a function of its size s : $\chi_{max}(T) \propto N(s)M^2(s)/T_B(s, \Theta_{Pd})$. In this expression, we used $M(s) \propto s$. $T_B(s, \Theta_{Pd})$ was assumed constant for a given Pd coverage as suggested by the small FWHM of the energy barrier of the Co islands in Chapter 4. Therefore, we estimated $s_{Co,max} = (1.8 \pm 0.2)\langle s_{Co} \rangle$ where $\langle s_{Co} \rangle$ is the mean island size inferred from the relation $\langle s_{Co} \rangle = \Theta_{Co}/d$ with d being the island density. $p_{Co,max} = (1.7 \pm 0.2)\langle p_{Co} \rangle$ is deduced from the relation between perimeter and surface. The dashed lines in Fig. 4.12 yields $E_{lat} - E_{Co,p} = -0.18 \pm 0.03$ meV/atom and $E_{vert} - E_{Co,s} = 0.33 \pm 0.04$ meV/atom. The value found in the case of the vertical interface is in very good agreement with the value found on Co/Pd multilayers with perpendicular anisotropy (see Section 4.1.1 or [259]).

In this simple model, we assumed that the contribution of Pd atoms surrounding the Co islands is limited to the first rim. Under this assumption, the lateral contribution to the energy barrier is fully effective after completion of the first Pd rim. In case of uniform decoration, we estimated this to happen at a coverage of about $\Theta_{Pd} \approx 0.05$ ML. This assumption is supported by the island morphology after Pd deposition. In Fig. 4.11 (right) the compact triangular shapes of the islands give evidence that Pd adatoms have a high edge mobility and suggests that Pd diffusion do not present chemical preference between Co and Pd. Therefore, Pd decoration around a Co core is expected to be uniform.

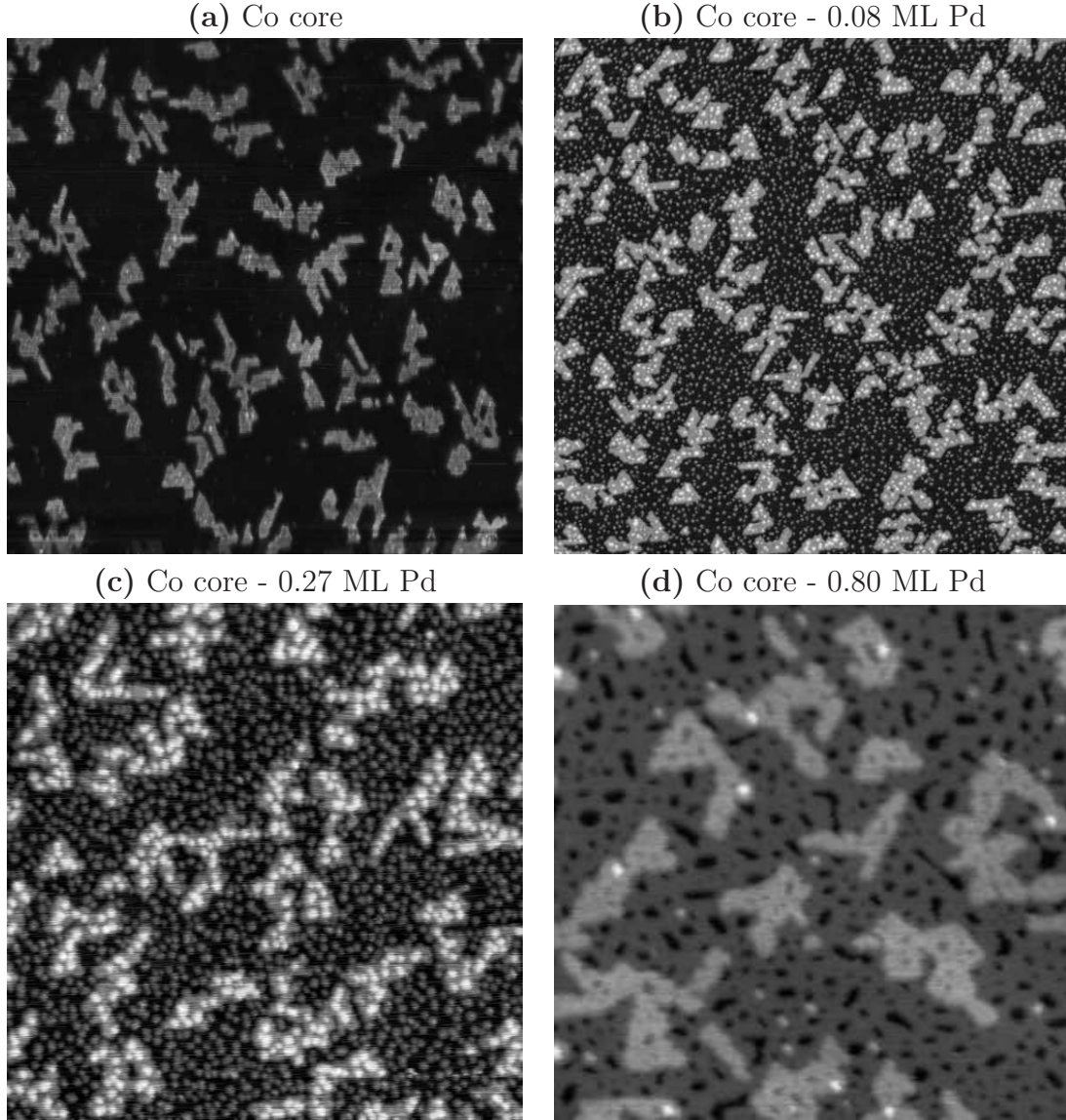


Fig. 4.13 – STM topographs of Co islands decorated by Pd deposited at 50 K then subsequently annealed to 180 K. (a) Co islands without Pd ($\Theta_{Co} = 0.31$ ML, $T_{dep} = 150$ K and 250 K), size : $2000 \times 2000 \text{ \AA}^2$. (b)(c)(d) Co islands decorated by Pd : (b) $\Theta_{Pd} = 0.08$ ML, size : $2000 \times 2000 \text{ \AA}^2$; (c) $\Theta_{Pd} = 0.27$ ML, size : $1200 \times 1200 \text{ \AA}^2$; (d) $\Theta_{Pd} = 0.80$ ML, size : $700 \times 700 \text{ \AA}^2$ (here, the temperature has reached 320 K during the magnetic characterization).

4.4.2 Pd statistical deposition on Co/Pt(111)

In the following, we discuss the effect of a low temperature deposition of Pd on a system composed of Co islands on Pt(111). Two different Co cores were grown using the two-steps deposition previously described. This growth protocol ensures a constant island density during all experiments and a relatively compact shape of the islands. We have deposited coverages of $\Theta_{Co} = 0.12 \pm 0.03$ ML and $0.31 \pm$

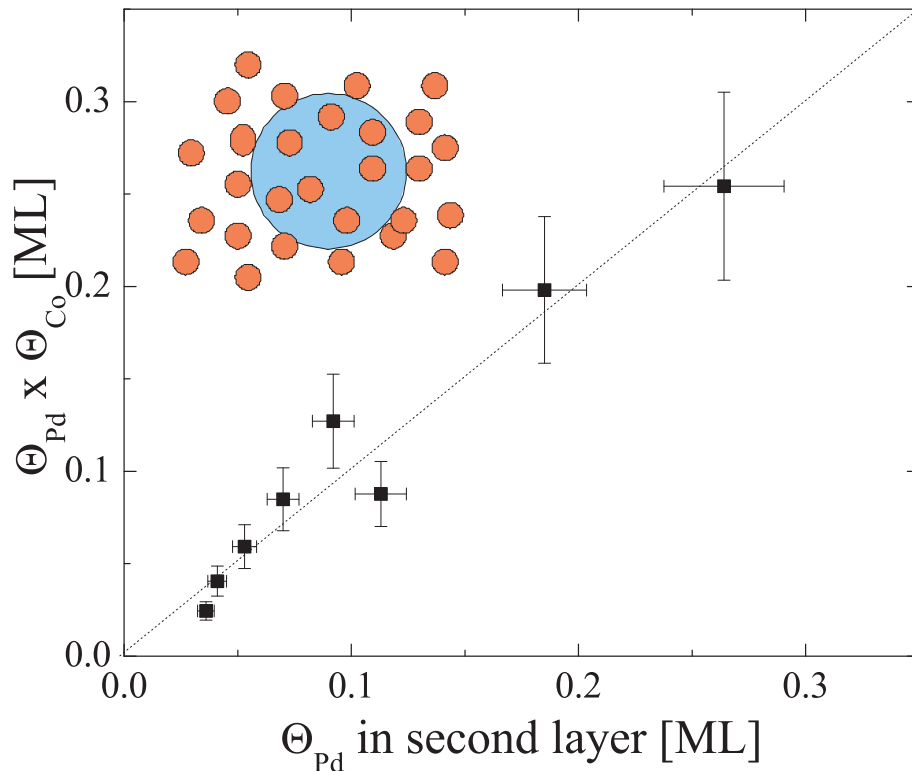


Fig. 4.14 – Pd coverage Θ_{Pd} on the Co islands estimated after a statistical deposition ($\Theta_{Pd} \times \Theta_{Co}$) as a function of the observed Θ_{Pd} in second layer.

0.03 ML in order to clearly make a distinction between the results associated with the two island sizes. Pd was deposited at 50 K, then annealed to 180 K during 5 minutes. The annealing temperature was chosen as an upper limit for the temperature during the magnetic measurements until $\Theta_{Pd} \geq 0.80$ ML. Pd coverage is estimated by $\Theta_{Pd} = \Theta_{total} - \Theta_{Co,nom.}$ where Θ_{total} is the total coverage estimated by STM and $\Theta_{Co,nom.}$ the nominal coverage of Co estimated from the flux calibration ^a. At 50 K, Pd diffusion processes are frozen [290] and, therefore, Pd adatoms are statistically deposited onto the surface. At 180 K, monomer diffusion is activated. On the contrary, at this temperature the high Ehrlich Schwoebel energy barrier is not overcome by the thermal energy of the Pd atoms. Therefore, Pd atoms which land on a Co island do not descend from the island. Because the mean free path of Pd adatoms is smaller than the distance between Co cores and even the Co core radius, small Pd clusters are formed on the whole surface. Fig. 4.13 illustrates this statistical repartition with three different Pd coverages on a Co/Pt(111) system. Fig. 4.13(a) represents the starting point of the experiments with a Co coverage of $\Theta_{Co} = 0.31 \pm 0.03$ ML and an island density of $1.7 \times 10^{-4} \pm 0.2 \times 10^{-4}$ island/site. In Figs. 4.4.1 (b) and (c), Θ_{Pd} is 0.08 ± 0.02 ML and 0.27 ± 0.03 ML, respectively.

^aSimilar experiments with Pt instead of Pd have been performed as well. The low signal and the high blocking temperature of some samples did not permit us to draw conclusions with this system.

Fig. 4.14 shows the product of the total Pd coverage by the Co coverage as a function of the coverage of the Pd in second layer. This product yields an estimation of the Pd coverage on top of the Co layer when all diffusion processes are inhibited, which characterizes the so-called statistical deposition. We remark that the estimated coverage of Pd in second layer agrees very well with the measured one. This result confirms that the Ehrlich Schwoebel energy barrier is not overcome at 180 K.

Magnetic properties The blocking temperature versus Θ_{Pd} is plotted in Fig. 4.15 for both Co coverages. The blocking temperature of the pure Co islands is 95 K and 125 K for the small and large islands, respectively. The blocking temperature reduces of 20 K for $\Theta_{Pd} = 0.08 \pm 0.02$ in the case of large islands. The reduction of T_B for the small islands is less pronounced. From this point until $\Theta_{Pd} \approx 0.60$ ML, the blocking temperatures increase linearly with the Pd coverage with a larger slope in the case of the large Co islands. A strong enhancement of T_B is observed above $\Theta_{Pd} = 0.60$ ML.

Discussion

The results have been interpreted with the same general model presented above. In this case, the number of Pd atoms on top of a Co island of size s_{Co} is $\Theta_{Pd} \cdot s_{Co}$. The number of Pd atoms in contact with a Co island of perimeter p_{Co} can be expressed likewise $\Theta_{Pd} \cdot p_{Co}$. Hence, the energy barrier E_b can be expressed :

$$E_b = \Theta_{Pd} [p_{Co,max}(E_{lat} - E_{Co,p}) + s_{Co,max}(E_{vert} - E_{Co,s})] + E_{Co} \quad (4.2)$$

where E_{Co} is the energy barrier of pure Co islands in meV estimated after the fitting procedure, $E_{Co,p}$ and $E_{Co,s}$ are the magnetic anisotropy energy contributions of surface and perimeter atoms, respectively, measured in meV/atom. $p_{Co,max}$ and $s_{Co,max}$ are the number of perimeter and surface atoms, respectively, for the Co islands which give the biggest contribution to the peak of the imaginary part of $\chi(T)$. In this expression, we have used the value for $\Delta E_{lat} = E_{lat} - E_{Co,p}$ that was estimated in the last section. The strong enhancement of the magnetic hardness above 0.60 ML is explained by an enhancement of $\Delta E_{vert}(\Theta_{Pd}) = E_{vert} - E_{Co,s}$ with Θ_{Pd} . The best fits are shown in Fig. 4.15 for the two Co coverage. This yields $\Delta E_{vert}(\Theta_{Pd}) = 0.05 + 0.18f(\Theta_{Pd})$ meV/atom where f is the test function represented in inset in Fig. 4.15. The curves obtained by fit can be divided into three parts . These parts are (1) the gap between the experimental data and the fit at $\Theta_{Pd} = 0$ ML ; (2) the linear T_B evolution at coverage $\Theta_{Pd} < 0.60$ ML ; (3) the strong T_B enhancement above 0.60 ML.

The gap between the experimental data and the fit at $\Theta_{Pd} = 0$ ML 20 K and 5 K was the observed gap between the experimental T_B for pure Co and the estimated T_B from the fitting procedure in the case of $\Theta_{Co} = 0.31$ ML and 0.12 ML, respectively. Due to a base pressure in the range of $10^{-11} - 10^{-10}$ mbar during all the time-controlled experimental procedure, we can exclude that the interactions between

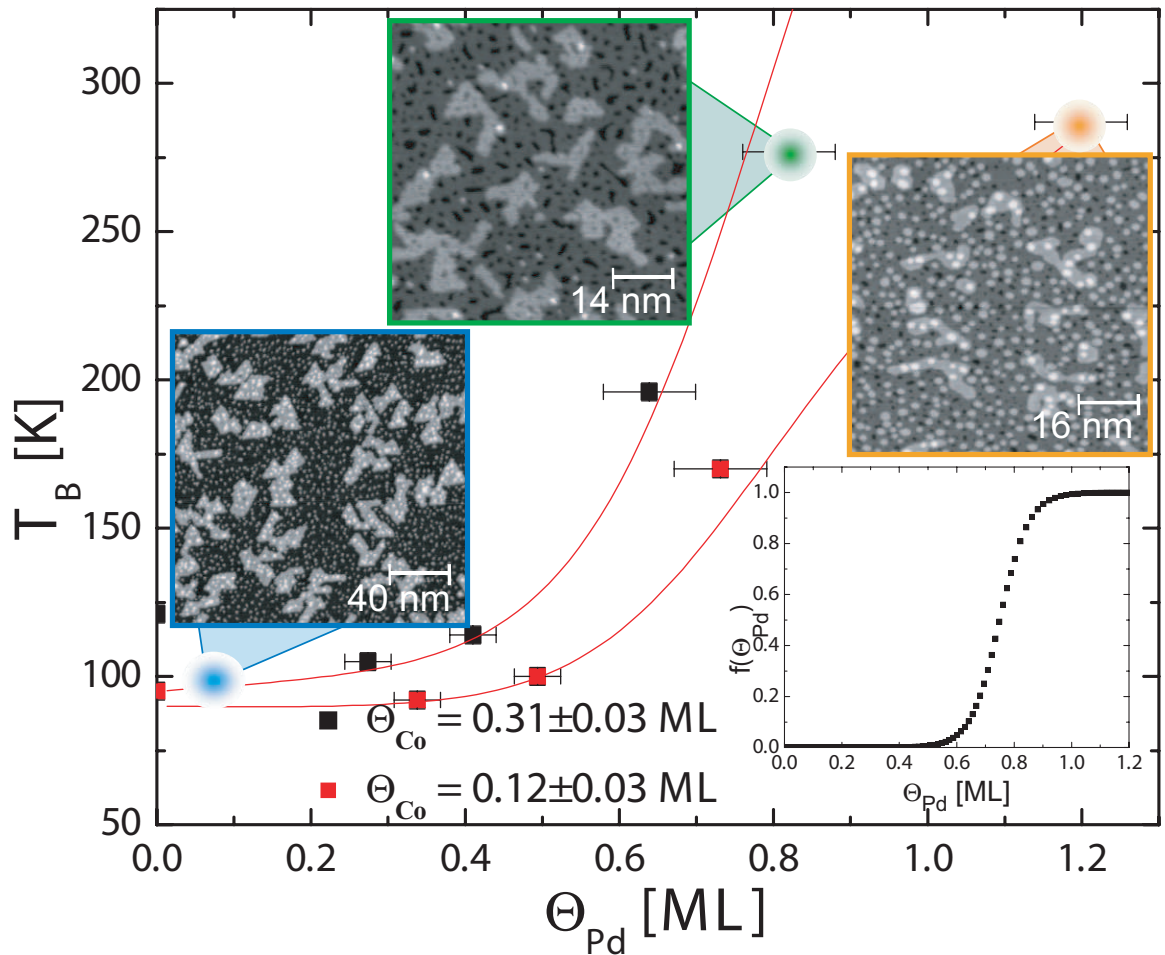


Fig. 4.15 – Blocking temperature T_B as a function of the total Pd coverage in the cases of $\Theta_{Co} = 0.12 \pm 0.03$ ML (red dots) and $\Theta_{Co} = 0.31 \pm 0.03$ ML (black dots) Co islands grown on a Pt(111) surface subsequently followed by a Pd deposition at 50 K then annealed to 180 K. The red solid lines are fits to the data using a model of coverage dependent contribution of the vertical interface to the energy barrier (see text for details). In insets are represented the resulting morphology. The test function used to model the energy variation with Pd coverage is also shown in inset.

the samples and the residual gas are responsible for such variation of T_B . We attribute the reduction of T_B after the deposition of a small amount of Pd to a complex interplay between Co and Pd. The theoretical calculations of Section.5.3 on Co cores decorated by Fe and Pt have predicted a variation of the magnetic anisotropy energy for the atoms of the two last rims of the islands. Hence, a similar behavior can be expected in the case of Pd where small Pd clusters decorate the Co cores. We notice besides that the phenomenon of easy attachment at the low deposition temperature, may provoke Pd atoms on Pt(111) to attach more easily to Co island edge. Therefore, at the onset of Pd deposition, the effect caused by the lateral interface on T_B should be more pronounced.

The linear T_B evolution at coverage $\Theta_{Pd} < 0.60$ ML Below $\Theta_{Pd} = 0.60$ ML, T_B varies linearly with Θ_{Pd} for both Co coverages. A linear fit gives a slope of 57 ± 7 K/ML and 20 ± 10 K/ML for large and small Co islands, respectively. This variation is expected for a statistical deposition where the number of Pd atoms in contact with the Co islands is proportional with Θ_{Pd} in the case of both lateral and vertical interface. The comparison between this kind of experiment and the Pd decoration of Co cores allows one to disentangle ΔE_{vert} and ΔE_{lat} . We note that the number of Pd atoms in contact with the Co island edge is slightly overestimated since Pd clusters have a limited contact surface with Co islands. From the relation (4.2), we deduce that the previous overestimation leads to an overestimation of ΔE_{vert} . Therefore, the strong difference between $\Delta E_{vert} = 0.05 \pm 0.02$ meV/atom estimated from this experiment and the previous one $\Delta E_{vert} = 0.33 \pm 0.04$ meV/atom is unexpected. The difference is attributed to a variation of ΔE_{vert} with the size and/or the shape of the Pd clusters on the top of the Co layer. Such a size and/or shape variation may cause stress relief in the Co island and could induce change of the magnetocrystalline constant of Co and/or Pd.

The strong T_B enhancement above 0.60 ML The strong enhancement of T_B above 0.60 ML has been explained with the variation of ΔE_{vert} with Θ_{Pd} . This variation is represented in inset in Fig. 4.15. The test function was chosen to reproduce the general evolution of coalescence between epitaxially grown islands (see [63] or Fig. 2.2 (left)) and yields $f(\Theta_{Pd}) = 1/1 + \exp -[(\Theta_{Pd} - 0.75)/0.05]$. The values 0.75 and 0.05 give the best fit within an error margin of 5% around these values. We remark that in our case the strong increase of the test function initiates at a characteristic coverage $\Theta_{Pd} = 0.6$ ML and not 0.3 ML as it is estimated for the coalescence between islands. This can be explained since for quasi-statistical deposition the limit for coalescence moves to higher coverages (for perfect statistical growth $\Theta_{limit} \approx 0.9$ ML) [308].

Others models have been proposed in order to explain the large enhancement of T_B :

- Percolation : We have observed that $\Theta_{Pd} = 0.6$ ML corresponds to the limit coverage before percolation occurs. Percolation is a phenomenon that links all the Co islands through a continuous Pd pattern. Fig. 4.13 (d) shows an example when percolation occurs in the case of 0.31 ± 0.03 ML of Co subsequently decorated by

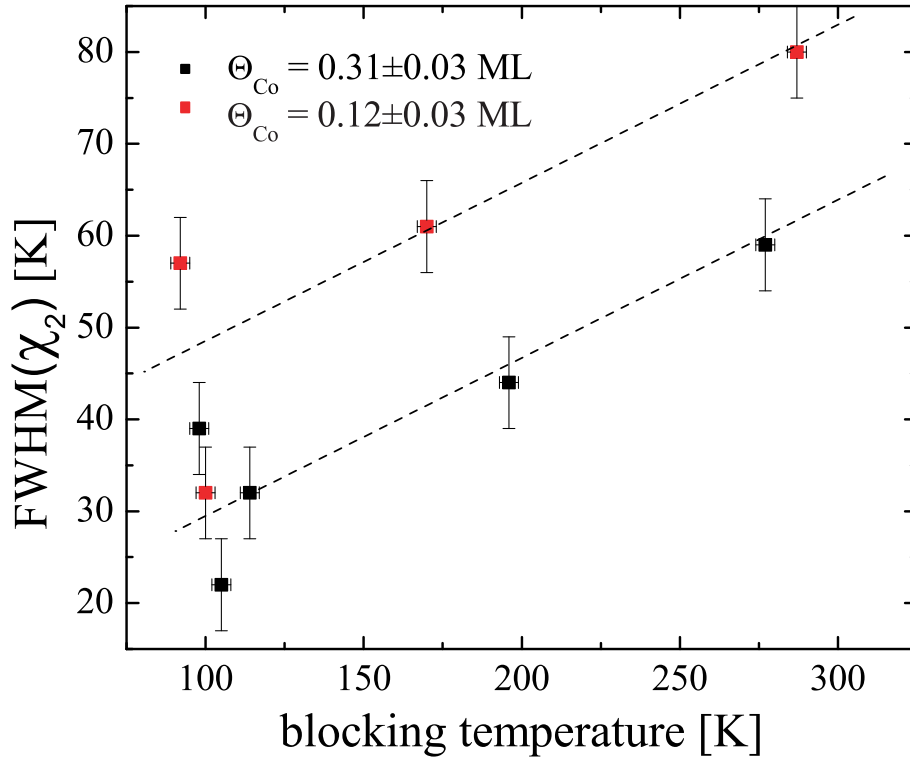


Fig. 4.16 – Full Width at Half Maximum (FWHM) of the peak of the imaginary part of $\chi(T)$ as a function of the blocking temperature for the two Co coverages investigated during the experiments with statistical Pd deposition. The dashed lines are guides to the eye.

0.80 ± 0.03 ML of Pd. As mentioned above, Pd might be polarisable by a Co atom until the fifth neighbor. From STM topographs, we can estimate that the mean distance between Co islands is around 100 \AA with a large distribution around $\pm 60 \text{ \AA}$. Therefore, we can expect that exchange interactions affect a large number of Co islands leading to a strong enhancement of the blocking temperature and eventually a double peak in the $\chi(T)$ curves or a large width of the distribution of anisotropy. Fig. 4.16 represents the Full Width at Half Maximum (FWHM) of the $\chi_2(T)$ peak. We observe that $\text{FWHM}(\chi_2(T))$ increases continuously with T_B for the two sizes of Co islands with a slope $\Delta \text{FWHM}(\chi_2(T))/\Delta T_B = 0.17$. For low T_B , the deviation to this linear increase is more important. In that kind of experiments, the shape of the distribution of anisotropy is generally well reproduced by the distribution of $\chi_2(T)$. We can simply understand this as follows : $\chi_2(T)$ represents the convolution of the theoretical $\chi_2(T)$ curve for an island of given anisotropy with the distribution of anisotropy within all the islands. Therefore, owing to a small width of the theoretical $\chi_2(T)$ peak, the shape of the overall $\chi_2(T)$ curve is, to a first approximation, directly proportional to the distribution of anisotropy. In this case, the continuous increase of $\text{FWHM}(\chi_2(T))$ with T_B suggests that percolation is not responsible for the strong T_B enhancement. A way to test the hypothesis of percolation would also be to observe the queue of the $\chi_1(T)$ curve. It was indeed proven that interaction between islands

would considerably flatten this curve [201].

- Evolution of the magnetic properties with the mean island size : one could argue that the T_B enhancement observed in all the experiments involving CoPd alloy may be the consequence of the polarization of Pd atoms decorating Co islands. This implies a variation of the characteristic size of which its T_B corresponds to the T_B of the overall sample. We can roughly estimate that Pd atoms in contact with Co acquires a magnetic moment of $\mu_{Pd} = 0.3 \mu_B$ [259, 282] that vanishes after the second neighbor. This way, the overall magnetization of an island increases of less than 10% after the deposition of 1 ML of Pd. Assuming the small distribution of anisotropy previously observed in Chapter 3, we can estimate an increase of T_B due to the increase of the characteristic island size around 10% after the deposition of 1 ML of Pd. Straightforwardly, we can rule out this hypothesis as the main reason for T_B enhancement.

4.5 Conclusion and update

Fe-Co In summary, combined in-situ STM and MOKE measurements on monolayer high core-shell islands of Co, Fe and Pt on Pt(111) were used to determine alloy and interface contributions to the blocking temperature. One-dimensional Fe-Co interfaces are found to have much higher energy barriers than random FeCo alloys. The formation of Pt-Co interface leads a negative contribution and reduces strongly the blocking temperature. The experimental features are accounted for by ab initio calculations of the magnetocrystalline anisotropy energy K_{mc} . This behavior reflects a strong variation of $\Delta_{\mu,orb}$ depending on the chemical composition of the outer shell.

Co-Pd Two kinds of Pd decoration of monolayer high Co islands on Pt(111) were used to determine lateral and vertical interface contributions to the blocking temperature. The lateral interface is found to give a negative energy barrier of 0.18 ± 0.04 meV/atom. The vertical interface gives a positive energy barrier which varies between 0.05 and 0.33 meV/atom depending on the kind of experiments and the Pd coverage. We attribute this variation to a strong relation between the size and/or shape of the Pd clusters on top of Co islands and the magnetic properties. Some questions remains opened. Our results did not allow us to determine the cause of the reduction of T_B for very low Pd coverage deposited at low temperature.

Update During the last weeks just before the completion of this manuscript, we had the occasion to perform KMC simulations (programme written by Ph. Bulushek and M. El Ouali based on a programme written by J. Jacobsen and further developed by H. Brune) on the system of Fe, Pt and Co decorated Co cores. Although the latest data still have to be analyzed, we anticipate here a significant result. The first KMC simulations presented in insets in Fig. 4.17 represent a Co island composed by 800 atoms decorated by Fe or Co and another Co island with 1260 atoms decorated by Pt. The diffusion parameters as well as the deposition temperature were chosen

coherently with the estimated value presented in this thesis. The resulting bimetallic island after a first "try" reproduces quite well the experimental morphology shown in Fig. 4.7. The blocking temperature was directly inferred from the simulated island and the MAE values given by *ab initio* calculations in Section 4.3 (see, Fig. 4.10). The general trends for the three different decorations is in excellent agreement with our experimental data. This encouraging result gives good perspectives toward the possibility to accurately tune the magnetic properties at the atomic scale.

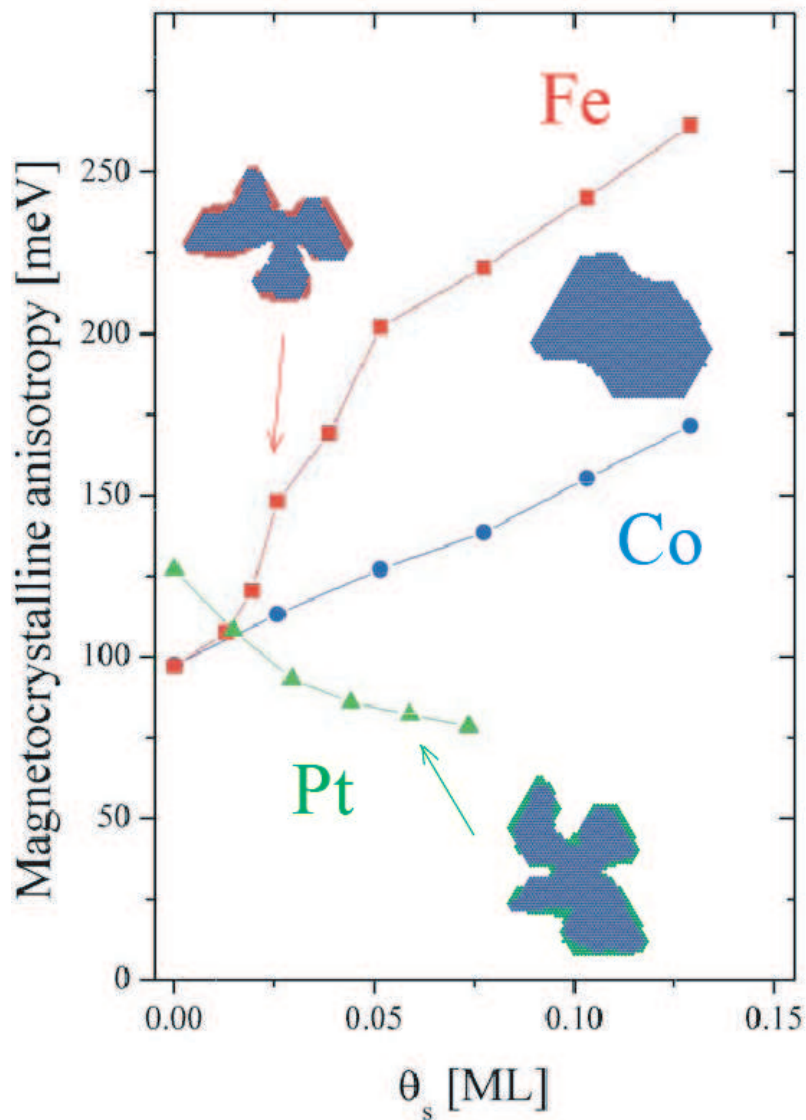


Fig. 4.17 – Estimated MAE as a function of the shell coverage for pure Co (blue), Co cores Fe shell (red), and Co cores Pt shell (green). The estimation takes into account the MAE per atom given in Fig. 4.10 and the morphology estimated with KMC simulations (insets).

Conclusions and perspectives

The initial goal of this manuscript was to give a comprehensive approach to the study of 2D bimetallic core-shell nanostructures. The combination of VT-STM with MOKE provided atomic-scale insight of the growth process together with macroscopic-scale information on the magnetic properties. We demonstrate the ability to grow epitaxial core-shell bimetallic 2D nanostructures with fine-tuning of the size and shape. Furthermore, the magnetic properties of such nanostructures have been investigated.

Nucleation and growth of Fe clusters on Pt(111) at low coverage has been studied by means of nucleation curves and VT-STM analysis. VT-STM is the adequate tool to disentangle thermally activated diffusion processes since it provides direct imaging of the grown clusters on a large range of temperature. Firstly, the step-wise increase of the mean island size with the annealing temperature is compared with rate equation models of ripening by cluster diffusion. The activation energies for monomer, dimer and trimer diffusion are inferred from this analysis. Secondly, the dissociation energy of Fe cluster is estimated. These results laid the cornerstones for a fine-tuning of core-shell 2D nanostructures.

Combined high resolution STM topographs together with a compelling analysis of cluster perimeter distribution permit us to establish explicitly the formation of monatomic Fe wires on a temperature scale of around 100 K. The fabrication and atomic-scale characterization of 1D structures is a priority in the study of low-dimensional condensed matter. In particular, the fast and simple wire formation with respect to the time consuming tip manipulation makes our method appealing so as to the study of electronic, magnetic and chemical properties on 1D systems. We note that Fe wires do not grow along the terrace step-edges as it is the case for most of the metal nanowires. The interplay of long-range interactions between adsorbates was proposed as the mechanism responsible for Fe migration toward the chain end.

Two-step deposition was used to build tailor-made 2D Fe and Co nanostructures. Size, shape and density were inferred from the diffusion parameters of the various elements. The island density imposed by the first deposition at lower temperature remains constant after the second deposition at higher temperature. The temperature and evaporation flux of the second deposition set the size and the shape from ramified

to compact islands. The realized Co nanostructures were used as model system to investigate the mechanism of magnetization reversal of nanostructures. A nontrivial task in the industry of data storage is to perfectly control the necessary time for the magnetization reversal of a bit. This characteristic time varies with the kind of mechanism. Hence, determining the mechanism of magnetization reversal becomes of particular relevance for magnetic data storage. The temperature dependence of the zero-field susceptibility was probed and compared to models of magnetization reversal by coherent rotation and domain-wall creation and motion. The results support that a transition mechanism occurs when the nanostructures are ramified with long arms of about 150 Å. In this case, the nanostructures present an unequivocal preference for magnetization reversal via nucleation and propagation of domains. On the contrary, the mechanism of magnetization reversal of large compact islands is well described by coherent rotation.

Tailoring magnetic properties of 2D nanostructures at the atomic scale requires independent tuning of magnetic anisotropy energy and magnetization. Bimetallic core-shell nanostructures with sharp interfaces or alloyed elements can address this issue. The analysis of the blocking temperature of various core-shell structures has allowed us to disentangle a number of contributions to the thermally activated barrier for magnetization reversal. Albeit random FeCo alloys have been found to exhibit high energy barriers, our results have evidenced that the creation of a one-dimensional lateral Fe-Co interface gives much higher contribution to the energy barrier around 0.9 ± 0.2 meV/atoms. Our models are consistent with *ab initio* calculations of the magnetocrystalline anisotropy performed by Bornemann and coworkers in Munich. The reduction of symmetry associated with the dimensionality of the systems as well as a strong hybridization of the *d* orbitals are the main factors characterizing an increase of the blocking temperature. The formation of Pt-Co and Pd-Co lateral interface leads a negative contribution to the energy barrier for thermally activated magnetization reversal. The well-defined statistical decoration of Co islands by Pd atoms was used so as to evaluate the magnetic properties issued from the creation of a sharp vertical interface between Co and Pd. An unexpected enhancement of the blocking temperature at coverage higher than 0.6 ML was associated with a continuous adaptation of the vertical energy while coalescence between Pd clusters occurs. Hence, the fine-tuning of the blocking temperature together with the overall magnetization of an island is proved to be perfectly conceivable and already achievable by molecular beam epitaxy.

The results presented in this manuscript open the way to several future investigations and developments. Some of them have already been mentioned throughout the manuscript. The formation by self-assembly of monatomic wires figures out many problems related to the creation of 1D structures and opens the door to a new realm of fascinating experiments. As an example, it was frequent to consider a nanowire along a step-edge as one-dimensional. By comparison, our Fe wires might now allow disentangling the contribution of the bond between atoms of the wires and the

step-edge with respect to the bond with the atoms from the surface plane. Circular structures are equally self-assembled. Direct observations of the electronic surface waves standing inside an Fe ring can give insights on the electronic properties of the metallic surface. Possible trapping of a metallic atom in the center of a chiral ring might be envisioned as a future medium for data storage.

From another aspect, the determination of the diffusion energy at the atomic scale and the realization of core-shell structures together with the magnetic characterization of the different origins of the enhancement of the blocking temperature give evidence that nano-engineering is becoming more than a wishful thinking. We have focused particularly in the case of applications in the technological area of magnetic data storage but a similar work could as well be used in the wide research field of heterogeneous catalysis where enhanced perimeter/surface ratio and fine-tuning of electronic properties are two major directions.

Bibliography

- [1] <http://www.zyvex.com/nanotech/feynman.html>.
- [2] H. Brune, M. Giovannini, K. Bromann, and K. Kern, *Nature* **394**, 451 (1998).
- [3] M. Corso, W. Auwarter, M. Muntwiler, A. Tamai, et al., *Science* **303**, 217 (2004).
- [4] F. Silly, M. Pivetta, M. Ternes, F. Patthey, et al., *New J. Phys.* **6**, 16 (2004).
- [5] S. Rousset, B. Croset, Y. Girard, G. Prévot, et al., *C.R. Phys.* **6**, 33 (2005).
- [6] N. Weiss, *Propriétés magnétiques de nanostructures de Cobalt adsorbées*, Ph.D. thesis, EPFL (2004).
- [7] G. Binnig, H. Rohrer, C. Gerber, and E. Weibel, *Phys. Rev. Lett.* **49**, 57 (1982).
- [8] G. Binnig, *Surf. Sci.* **126**, 236 (1985).
- [9] N. García, C. Ocal, and F. Flores, *Phys. Rev. Lett.* **50**, 2002 (1983).
- [10] E. Stoll, *Surf. Sci.* **143**, L411 (1984).
- [11] J. Tersoff and D. R. Hamann, *Phys. Rev. Lett.* **50**, 1998 (1983).
- [12] A. Baratoff, *Physica B+C* **127**, 143 (1984).
- [13] J. Bardeen, *Phys. Rev. Lett.* **6**, 57 (1961).
- [14] E. L. Wolf, *Principles of Electron Tunneling Spectroscopy* (Oxford University Press, New York, 1985).
- [15] N. D. Lang, *Phys. Rev. B* **34**, 5947 (1986).
- [16] H. Röder, *Microscopic processes in heteroepitaxial growth : nucleation, growth and alloying of silver on the (111) surface of platinum*, Ph.D. thesis, EPFL (1994).
- [17] K. Bromann, *Controlling epitaxial morphologies on the microscopic scale*, Ph.D. thesis, EPFL (1997).

-
- [18] M. Giovannini, *Metallic thin layers and nanostructures : fabrication and characterization*, Ph.D. thesis, EPFL (2000).
- [19] K. Besocke, Surf. Sci. **181**, 145 (1987).
- [20] E. R. Moog, C. Liu, S. D. Bader, and J. Zak, Phys. Rev. B **39**, 6949 (1989).
- [21] S. D. Bader, J. Magn. Magn. Mater. **100**, 440 (1991).
- [22] M. Faradays, Trans. Roy. Soc. (London) **5**, 592 (1846).
- [23] J. Kerr, Phil. Mag. **3**, 339 (1887).
- [24] H. R. Hulme, Proc. R. Soc. Lond. A **135**, 237 (1932).
- [25] P. N. Argyres, Phys. Rev. **97**, 334 (1955).
- [26] J. L. Erskine and E. A. Stern, Phys. Rev. B **8**, 1239 (1973).
- [27] Z. J. Yang and M. R. Scheinfein, J. Appl. Phys. **74**, 6810 (1993).
- [28] J.-W. Lee, J.-R. Jeong, D.-H. Kim, J. S. Ahn, et al., Rev. Sci. Instrum. **71**, 3801 (2000).
- [29] J. Zak, E. R. Moog, C. Liu, and S. D. Bader, J. Appl. Phys. **68**, 4203 (1990).
- [30] Z. Q. Qiu and S. D. Bader, J. Magn. Magn. Mater. **200**, 664 (1999).
- [31] Z. Q. Qiu and S. D. Bader, Rev. Sci. Instrum. **71**, 1243 (2000).
- [32] <http://www.msd.anl.gov/groups/mf/jmkerrcalc.php>.
- [33] G. Moulas, A. Lehnert, S. Rusponi, J. Zabloudil, et al., accepted by Phys. Rev. B.
- [34] P. Gambardella, S. Rusponi, M. Veronese, S. S. Dhesi, et al., Science **300**, 1130 (2003).
- [35] C. S. Arnold, M. Dunlavy, and D. Venus, Rev. Sci. Instrum. **68**, 4212 (1997).
- [36] Y.-L. He and G.-C. Wang, Phys. Rev. Lett. **70**, 2336 (1993).
- [37] T. Michely, Surf. Sci. **256**, 217 (1991).
- [38] T. Michely and C. Teichert, Phys. Rev. B **50**, 11156 (1994).
- [39] M. Kalff, Surf. Sci. **486**, 103 (2001).
- [40] J. Gland, Surf. Sci. **95**, 587 (1980).
- [41] C. Campbell, Surf. Sci. **107**, 220 (1981).
- [42] N. R. Avery, Chem. Phys. Lett. **96**, 371 (1983).

BIBLIOGRAPHY

- [43] A. Artsyukhovich, *Surf. Sci.* **347**, 303 (1996).
- [44] D. Repetto, T. Y. Lee, S. Rusponi, J. Honolka, et al., *Phys. Rev. B* **74**, 054408 (2006).
- [45] T.-Y. Lee, S. Sarbach, K. Kuhnke, and K. Kern, *Surf. Sci.* **600**, 3266 (2006).
- [46] M. Tsujikawa, A. Hosokawa, and T. Oda, *J. Phys. : Condens. Matter* **19**, J5208 (2007).
- [47] J.-U. Thiele, L. Folks, M. F. Toney, and D. K. Weller, *J. Appl. Phys.* **84**, 5686 (1998).
- [48] S. Sun, C. B. Murray, D. Weller, L. Folks, et al., *Science* **287**, 1989 (2000).
- [49] D. Weller, A. Moser, L. Folks, M. Best, et al., *IEEE Trans. Magn.* **36**, 10 (2000).
- [50] D. Sellmyer, C. Luo, M. Yan, and Y. Liu, *IEEE Trans. Magn.* **37**, 1286 (2001).
- [51] H. Zeng, M. L. Yan, N. Powers, and D. J. Sellmyer, *Appl. Phys. Lett.* **80**, 2350 (2002).
- [52] P. Beccat, *Surf. Sci.* **238**, 105 (1990).
- [53] T. Toda, H. Igarashi, and M. Watanabe, *J. Electroanal. Chem.* **460**, 258 (1999).
- [54] H. Igarashi, T. Fujino, Y. Zhu, H. Uchida, et al., *Phys. Chem. Chem. Phys.* **3**, 306 (2001).
- [55] D. Jerdev, *Surf. Sci.* **513**, L391 (2002).
- [56] Y. J. Chen, H. Y. Ho, C. C. Tseng, and C. S. Shern, *Surf. Sci.* **601**, 4334 (2007).
- [57] T. Wadayama, H. Osano, K. Murakami, T. Maeyama, et al., *J. Phys : Conf. Ser.* **100**, 012007 (2008).
- [58] U. Kürpick, A. Kara, and T. S. Rahman, *Phys. Rev. Lett.* **78**, 1086 (1997).
- [59] A. Kara and T. S. Rahman, *Phys. Rev. Lett.* **81**, 1453 (1998).
- [60] G. Ehrlich, *Surf. Sci.* **246**, 1 (1991).
- [61] K. Kyuno and G. Ehrlich, *Surf. Sci.* **437**, 29 (1999).
- [62] H. Brune, G. S. Bales, J. Jacobsen, C. Boragno, et al., *Phys. Rev. B* **60**, 5991 (1999).
- [63] H. Brune, *Surf. Sci. Rep.* **31**, 125 (1998).
- [64] C. Ratsch and J. A. Venables, *J. Vac. Sci. Technol.* **21**, 96 (2003).
- [65] G. Zinmeister, *Vacuum* **16**, 529 (1966).

-
- [66] G. Zinmeister, *Thin Solid Films* **7**, 51 (1971).
- [67] J. A. Venables, *Philosophical Magazine* **27**, 697 (1973).
- [68] A. F. Voter, *Phys. Rev. B* **34**, 6819 (1986).
- [69] J. C. Tully, G. H. Gilmer, and M. Shugard, *J. Chem. Phys.* **71**, 1630 (1979).
- [70] J. A. Venables, G. D. T. Spiller, and M. Hanbucken, *Rep. Prog. Phys.* **47**, 399 (1984).
- [71] A. Bogicevic, S. Ovesson, P. Hyldgaard, B. I. Lundqvist, et al., *Phys. Rev. Lett.* **85**, 1910 (2000).
- [72] K. A. Fichthorn, M. L. Merrick, and M. Scheffler, *Appl. Phys. A* **75**, 17 (2002).
- [73] V. S. Stepanyuk, A. N. Baranov, D. V. Tsvilin, W. Hergert, et al., *Phys. Rev. B* **68**, 205410 (2003).
- [74] C. Polop, H. Hansen, C. Busse, and T. Michely, *Phys. Rev. B* **67**, 193405 (2003).
- [75] R. Grima, J. Degraffenreid, and J. A. Venables, *Phys. Rev. B* **76**, 233405 (2007).
- [76] J. A. Venables and H. Brune, *Phys. Rev. B* **66**, 195404 (2002).
- [77] M. Bott, M. Hohage, M. Morgenstern, T. Michely, et al., *Phys. Rev. Lett.* **76**, 1304 (1996).
- [78] P. Bulushek, *Submonolayer growth of Cobalt on metallic and insulating surfaces studied by scanning tunneling microscopy and Kinetic Monte-Carlo simulations*, Ph.D. thesis, EPFL (2007).
- [79] S. C. Wang and G. Ehrlich, *Phys. Rev. Lett.* **70**, 41 (1993).
- [80] C. M. Chang, C. M. Wei, and S. P. Chen, *Phys. Rev. Lett.* **85**, 1044 (2000).
- [81] J. Yang, W. Hu, G. Yi, and J. Tang, *Applied Surf. Sci.* **253**, 8825 (2007).
- [82] S. C. Wang and E. G., *Surf. Sci.* **239**, 301 (1990).
- [83] H. Bulou and C. Massobrio, *Phys. Rev. B* **72**, 205427 (2005).
- [84] B. C. Stipe, M. A. Rezaei, and W. Ho, *J. Chem. Phys.* **107**, 6443 (1997).
- [85] P. Gambardella, *Surf. Sci.* **449**, 93 (2000), and references therein.
- [86] P. Gambardella and M. Blanc, *Phys. Rev. B* **61**, 2254 (2000).
- [87] C. Girardet, C. Ramseyer, and F. Picaud, *Phys. Scr.* **68**, 104 (2003).
- [88] X. Tan, G. Ouyang, and G. W. Yang, *Appl. Phys. Lett.* **88**, 263116 (pages 3) (2006).

BIBLIOGRAPHY

- [89] J. Guo, Y. Mo, E. Kaxiras, Z. Zhang, et al., Phys. Rev. B **73**, 193405 (2006).
- [90] T. R. Linderoth, S. Horch, E. Lægsgaard, I. Stensgaard, et al., Phys. Rev. Lett. **78**, 4978 (1997).
- [91] Y. Li, M. Bartelt, J. Evans, N. Waelchli, et al., Physical Review B **56**, 12539 (1997).
- [92] J.-P. Bucher, E. Hahn, P. Fernandez, C. Massobrio, et al., Europhys. Lett. **27**, 473 (1994).
- [93] N. Nilius, T. M. Wallis, and W. Ho, Science **297**, 1853 (2002).
- [94] C. F. Hirjibehedin, C. P. Lutz, and A. J. Heinrich, Science **312**, 1021 (2006).
- [95] A. Sperl, J. Kröger, N. Néel, H. Jensen, et al., Phys. Rev. B **77**, 085422 (2008).
- [96] H. Ohnishi, Y. Kondo, and K. Takayanagi, Nature **395**, 780 (1998).
- [97] A. I. Yanson, G. R. Bollinger, H. E. van den Brom, N. Agrait, et al., Nature **395**, 783 (1998).
- [98] D. Sánchez-Portal, E. Artacho, J. Junquera, P. Ordejón, et al., Phys. Rev. Lett. **83**, 3884 (1999).
- [99] S. B. Legoas, D. S. Galvão, V. Rodrigues, and D. Ugarte, Phys. Rev. Lett. **88**, 076105 (2002).
- [100] R. H. M. Smit, C. Untiedt, and J. M. van Ruitenbeek, Nanotechnology **15**, 472 (2004).
- [101] M. F. Crommie, C. P. Lutz, and D. M. Eigler, Phys. Rev. B **48**, 2851 (1993).
- [102] B. Hammer and J. K. Nørskov, Phys. Rev. Lett. **79**, 4441 (1997).
- [103] E. Lundgren, B. Stanka, W. Koprolin, M. Schmid, et al., Surf. Sci. **423**, 357 (1999).
- [104] N. Nilius, T. M. Wallis, and W. Ho, Appl. Phys. A **80**, 951 (2005).
- [105] T. R. Linderoth, S. Horch, L. Petersen, S. Helveg, et al., Phys. Rev. Lett. **82**, 1494 (1999).
- [106] F. Montalenti and R. Ferrando, J. Chem. Phys. **113**, 349 (2000).
- [107] W. Wulfhekel, T. Gutjahr-Löser, F. Zavaliche, D. Sander, et al., Phys. Rev. B **64**, 144422 (2001).
- [108] S. D., Curr. Opin. Solid State Mater. Sci **7**, 51 (2003).
- [109] P. J. Feibelman, Phys. Rev. B **56**, 2175 (1997).

- [110] H. Brune, K. Bromann, H. Röder, K. Kern, et al., Phys. Rev. B **52**, R14380 (1995).
- [111] P. Grütter and U. T. Dürig, Phys. Rev. B **49**, 2021 (1994).
- [112] D. Repetto, *Investigation and modification of the magnetism of epitaxial Fe structures*, Ph.D. thesis, EPFL (2005).
- [113] T.-Y. Lee, *Growth and magnetism of low-dimensional metallic nanostructures on the Pt(997) surface*, Ph.D. thesis, EPFL (2005).
- [114] D. Repetto, J. Honolka, S. Rusponi, H. Brune, et al., Appl. Phys. A **82**, 109 (2006).
- [115] R. Dingreville and J. Qu, Journal of Mechanics Physics of Solids **53**, 1827 (2005).
- [116] V. S. Stepanyuk, D. I. Bazhanov, A. N. Baranov, W. Hergert, et al., Phys. Rev. B **62**, 15398 (2000).
- [117] A. V. Ruban, H. L. Skriver, and J. K. Nørskov, Phys. Rev. B **59**, 15990 (1999).
- [118] P. Grütter, Surf. Sci. **337**, 147 (1995).
- [119] S. J. Koh and G. Ehrlich, Phys. Rev. Lett. **87**, 106103 (2001).
- [120] M. F. Crommie, C. P. Lutz, and D. M. Eigler, Science **262**, 218 (1993).
- [121] S. Chikazumi, *Physics of Magnetism* (Wiley, 1964).
- [122] S. Polesya, O. Sipr, S. Bornemann, J. Minár, et al., Europhys. Lett. **74**, 1074 (2006).
- [123] M. Etzkorn, P. S. Anil Kumar, W. Tang, Y. Zhang, et al., Phys. Rev. B **72**, 184420 (2005).
- [124] M. Bode, O. Pietzsch, A. Kubetzka, and R. Wiesendanger, Phys. Rev. Lett. **92**, 067201 (2004).
- [125] M. van Schilfgaarde and V. P. Antropov, J. Appl. Phys. **85**, 4827 (1999).
- [126] P. Bruno, Phys. Rev. B **39**, 865 (1989).
- [127] G. van der Laan, J. Phys. : Condens. Matter **10**, 3239 (1998).
- [128] S. Rusponi, T. Cren, N. Weiss, M. Epple, et al., Nat. Mater. **2**, 546 (2003).
- [129] D. Sander, S. Ouazi, A. Enders, T. Gutjahr-Löser, et al., J. Phys. : Condens. Matter **14**, 4165 (2002).
- [130] D. Sander, Rep. Prog. Phys. **62**, 809 (1999).

BIBLIOGRAPHY

- [131] K. Ha and R. C. O'Handley, *J. Appl. Phys.* **85**, 5282 (1999).
- [132] T. Gutjahr-Löser, D. Sander, and J. Kirschner, *J. Appl. Phys.* **87**, 5920 (2000).
- [133] M. Komelj and M. Fähnle, *J. Magn. Magn. Mater.* **222**, 245 (2000).
- [134] R. Skomski, *Spin Electronics* (Springer, Berlin, 2001), p 204.
- [135] A. Hubert and R. Schäfer, *Magnetic domains. The analysis of magnetic microstructures* (Springer, Berlin, 1999).
- [136] R. Skomski, H.-P. Oepen, and J. Kirschner, *Phys. Rev. B* **58**, 3223 (1998).
- [137] R. Skomski, *J. Phys. : Condens. Matter* **15**, R841 (2003).
- [138] F. Meier, K. von Bergmann, P. Ferriani, J. Wiebe, et al., *Phys. Rev. B* **74**, 195411 (2006).
- [139] H. Brune and S. Rusponi, *Magnetic properties of 2D islands on single crystal metal surfaces*, in *Atomic Clusters : From Gas Phase to Deposited* (Elsevier, Amsterdam, 2007), Vol. 12, 427-470.
- [140] W. Wernsdorfer, E. B. Orozco, K. Hasselbach, A. Benoit, et al., *Phys. Rev. Lett.* **78**, 1791 (1997).
- [141] R. W. Chantrell, N. Y. Ayoub, and J. Popplewell, *J. Magn. Magn. Mater.* **53**, 199 (1985).
- [142] O. Fruchart, P.-O. Jubert, C. Meyer, M. Klaua, et al., *J. Magn. Magn. Mater.* **239**, 224 (2002).
- [143] R. P. Cowburn and M. E. Welland, *Phys. Rev. B* **58**, 9217 (1998).
- [144] S. Rohart, V. Repain, A. Thiaville, and S. Rousset, *Phys. Rev. B* **76**, 104401 (2007).
- [145] R. Allenspach, M. Stampanoni, and A. Bischof, *Phys. Rev. Lett.* **65**, 3344 (1990).
- [146] L. Landau and E. Lifshitz, *Phys. Z. Sowjetunion* **8**, 153 (2002).
- [147] E. Fatuzzo, *Phys. Rev.* **127**, 1999 (1962).
- [148] D. C. Jiles and D. L. Atherton, *J. Magn. Magn. Mater.* **61**, 48 (1986).
- [149] F. Preisach, *Z. Phys.* **94**, 277 (1935).
- [150] A. Globus, *Proc. Europ. Physical Society, Conference on Soft Magnetic Material* **2**, 233 (1975).
- [151] A. Gaunt, *Philos. Mag. B* **48**, 261 (1983).

- [152] J. Pommier, P. Meyer, G. Pénissard, J. Ferré, et al., Phys. Rev. Lett. **65**, 2054 (1990).
- [153] W. Wernsdorfer, Adv. Chem. Phys. **118**, 99 (2001).
- [154] U. Schlickum, W. Wulfhekel, and J. Kirschner, Appl. Phys. Lett. **83**, 2016 (2003).
- [155] S. Anders, H. A. Padmore, R. M. Duarte, T. Renner, et al., Rev. of Sci. Instr. **70**, 3973 (1999).
- [156] C. Kittel, Rev. Mod. Phys. **21**, 541 (1949).
- [157] A. Aharoni, *Introduction to the theory of ferromagnetism* (Oxford University Press, New York, 2000).
- [158] H.-B. Braun, Phys. Rev. Lett. **71**, 3557 (1993).
- [159] N. L. Schryer and L. R. Walker, J. Appl. Phys. **45**, 5406 (1974).
- [160] H. Forster, T. Schrefl, W. Scholz, D. Suess, et al., J. Magn. Magn. Mater. **249**, 181 (2002).
- [161] A. Thiaville and Y. Nakatani, *Spin Dynamics in Confined Magnetic Structures III* (Springer, Berlin, 2006).
- [162] A. Globus, P. Duplex, and M. Guyot, IEEE Trans. Magn. **7**, 617 (1971).
- [163] M. Le Floch, J. Appl. Phys. **67**, 405 (1990).
- [164] S. Lemerle, J. Ferré, C. Chappert, V. Mathet, et al., Phys. Rev. Lett. **80**, 849 (1998).
- [165] T. Nattermann, V. Pokrovsky, and V. M. Vinokur, Phys. Rev. Lett. **87**, 197005 (2001).
- [166] D. Jiles and D. Atherton, IEEE Trans. Magn. **19**, 2183 (1983).
- [167] X. Chen, O. Sichelshmidt, W. Kleemann, O. Petravic, et al., Phys. Rev. Lett. **89**, 137203 (2002).
- [168] O. Petravic, A. Glatz, and W. Kleemann, Phys. Rev. B **70**, 214432 (2004).
- [169] A. Thiaville, J. Magn. Magn. Mater. **182**, 5 (1998).
- [170] D. Braun, J. Magn. Magn. Mater. **283**, 1 (2004).
- [171] P. Bruno, Phys. Rev. Lett. **83**, 2425 (1999).
- [172] O. Pietzsch, A. Kubetzka, M. Bode, and R. Wiesendanger, Phys. Rev. Lett. **84**, 5212 (2000).

BIBLIOGRAPHY

- [173] H. B. Braun, Phys. Rev. B **50**, 16485 (1994).
- [174] H. B. Braun, Phys. Rev. B **50**, 16501 (1994).
- [175] H. B. Braun, J. Appl. Phys. **50**, 6172 (1999).
- [176] G. Brown, M. A. Novotny, and P. A. Rikvold, Phys. Rev. B **64**, 134422 (2001).
- [177] H. Forster, N. Bertram, X. Wang, R. Dittrich, et al., J. Magn. Magn. Mater. **267**, 69 (2003).
- [178] A. F. Khapikov, J. Appl. Phys. **89**, 7454 (2001).
- [179] S. Rusponi, N. Weiss, T. Cren, M. Epple, et al., Appl. Phys. Lett. **87**, 2514 (2005).
- [180] F. Meier, L. Zhou, J. Wiebe, and R. Wiesendanger, Science **320**, 82 (2008).
- [181] G. M. Bell and D. A. Lavis, *Statistical Mechanics of Lattice Models*, vol. 1 (Ellis Horwood Limited, 1989).
- [182] T. Koide, H. Miyauchi, J. Okamoto, T. Shidara, et al., Phys. Rev. Lett. **87**, 257201 (2001).
- [183] J. P. Bucher, I. Chado, H. Bulou, and P. Ohresser, Phys. Rev. Lett. **90**, 149703 (2003).
- [184] N. Weiss, T. Cren, M. Epple, S. Rusponi, et al., Phys. Rev. Lett. **95**, 157204 (2005).
- [185] S. Pick, V. S. Stepanyuk, A. N. Baranov, W. Hergert, et al., Phys. Rev. B **68**, 104410 (2003).
- [186] H. A. Dürr, S. S. Dhesi, E. Dudzik, D. Knabben, et al., Phys. Rev. B **59**, R701 (1999).
- [187] D.-X. Chen, J. Brug, and R. Goldfarb, IEEE Trans. Magn. **27**, 3601 (1991).
- [188] T. Cren, S. Rusponi, N. Weiss, M. Epple, et al., J. Phys. Chem. B **108**, 14685 (2004).
- [189] S. I. Woods, J. R. Kirtley, S. Sun, and R. H. Koch, Phys. Rev. Lett. **87**, 137205 (2001).
- [190] S. Rohart, V. Repain, A. Tejada, P. Ohresser, et al., Phys. Rev. B **73**, 165412 (2006).
- [191] O. Robach, C. Quiros, P. Steadman, K. F. Peters, et al., Phys. Rev. B **65**, 054423 (2002).
- [192] R. Zhang and R. F. Willis, Phys. Rev. Lett. **86**, 2665 (2001).

- [193] R. Skomski, D. Sander, J. Shen, and J. Kirschner, *J. Appl. Phys.* **81**, 4710 (1997).
- [194] M. Bander and D. L. Mills, *Phys. Rev. B* **38**, 12015 (1988).
- [195] N. Akulov, *Z. Phys.* **100** (1936).
- [196] E. R. Callen and H. B. Callen, *Phys. Rev.* **129**, 578 (1963).
- [197] R. Skomski, O. N. Mryasov, J. Zhou, and D. J. Sellmyer, *J. Appl. Phys.* **99**, 916 (2006).
- [198] R. Skomski, A. Kashyap, and D. J. Sellmyer, *IEEE Trans. Magn.* **39**, 2917 (2003).
- [199] O. N. Mryasov, U. Nowak, K. Y. Guslienko, and R. W. Chantrell, *Europhys. Lett.* **69**, 805 (2005).
- [200] J. B. Staunton, L. Szunyogh, A. Buruzs, B. L. Gyorffy, et al., *Phys. Rev. B* **74**, 144411 (2006).
- [201] R. W. Chantrell, N. Walmsley, J. Gore, and M. Maylin, *Phys. Rev. B* **63**, 024410 (2000).
- [202] J.-O. Andersson, C. Djurberg, T. Jonsson, P. Svedlindh, et al., *Phys. Rev. B* **56**, 13983 (1997).
- [203] C. Haginoya, S. Heike, M. Ishibashi, K. Nakamura, et al., *J. Appl. Phys.* **85**, 8327 (1999).
- [204] M. Sharrock, *IEEE Trans. Magn.* **26**, 193 (1990).
- [205] S. Ferrer, J. Alvarez, E. Lundgren, X. Torrelles, et al., *Phys. Rev. B* **56**, 9848 (1997).
- [206] M. Suzuki, H. Miyagawa, N. Kawamura, H. Muraoka, et al., *Phys. Scr.* **T115**, 580 (2005).
- [207] J. Alvarez, E. Lundgren, X. Torrelles, H. Isern, et al., *Phys. Rev. B* **60**, 10193 (1999).
- [208] F. Wilhelm, P. Poulopoulos, H. Wende, A. Scherz, et al., *Phys. Rev. Lett.* **87**, 207202 (2001).
- [209] W. Grange, I. Galanakis, M. Alouani, M. Maret, et al., *Phys. Rev. B* **62**, 1157 (2000).
- [210] W. Grange, M. Maret, J.-P. Kappler, J. Vogel, et al., *Phys. Rev. B* **58**, 6298 (1998).
- [211] I. V. Solovyev, P. H. Dederichs, and I. Mertig, *Phys. Rev. B* **52**, 13419 (1995).

BIBLIOGRAPHY

- [212] A. Globus and P. Duplex, *IEEE Trans. Magn.* **2**, 441 (1966).
- [213] F. Liorzou, B. Phelps, and D. Atherton, *IEEE Trans. Magn.* **36**, 418 (2000).
- [214] J.-E. Wegrowe, D. Kelly, A. Franck, S. E. Gilbert, et al., *Phys. Rev. Lett.* **82**, 3681 (1999).
- [215] D. Hrabovsky, E. Vanelle, A. R. Fert, D. S. Yee, et al., *Appl. Phys. Lett.* **81**, 2806 (2002).
- [216] D. L. Atherton and J. R. Beattie, *IEEE Trans. Magn.* **26**, 3059 (2000).
- [217] J. Füzi, *Physica B* **372**, 396 (2006).
- [218] L. M. Alvarez-Prado, G. T. Pérez, R. Morales, F. H. Salas, et al., *Phys. Rev. B* **56**, 3306 (1997).
- [219] D. Jiles, J. Thoelke, and M. Devine, *IEEE Trans. Magn.* **28**, 27 (1992).
- [220] P. Pouloupoulos, M. Farle, U. Bovensiepen, and K. Baberschke, *Phys. Rev. B* **55**, R11961 (1997).
- [221] L. Pauling, *Phys. Rev.* **54**, 899 (1938).
- [222] C. Takahashi, M. Ogura, and H. Akai, *J. Phys. : Condens. Matter* **19**, 365233 (2007).
- [223] M. Lezaic, P. Mavropoulos, and S. Bluegel, *Appl. Phys. Lett.* **90**, 082504 (2007).
- [224] N. Hamada, *J. Phys. Soc. Jpn.* **46**, 1759 (1979).
- [225] R. Victora, L. Falicov, and S. Ishida, *Phys. Rev. B* **30**, 3896 (1984).
- [226] Y. Kakehashi and O. Hosohata, *Phys. Rev. B* **40**, 9080 (1989).
- [227] Y. Kakehashi, *Prog. Theor. Phys. Suppl.* **101**, 105 (1990).
- [228] J. M. MacLaren, T. C. Schulthess, W. H. Butler, R. Sutton, et al., *J. Appl. Phys.* **85**, 4833 (1999).
- [229] T. Burkert, L. Nordstrom, O. Eriksson, and O. Heinonen, *Phys. Rev. Lett.* **93**, 27203 (2004).
- [230] J. Friedel, *Il nuovo cimento* **7**, 287 (1958).
- [231] J. Bansmann, S. H. Baker, C. Binns, J. A. Blackman, et al., *Surf. Sci. Rep.* **56**, 189 (2005).
- [232] F. Yildiz, F. Luo, C. Tieg, R. Abrudan, et al., *Phys. Rev. Lett.* **100**, 37205 (2008).

-
- [233] S. Pizzini, A. Fontaine, E. Dartyge, C. Giorgetti, et al., Phys. Rev. B **50**, 3779 (1994).
- [234] H. Brune, private communication (2008).
- [235] S. Denmler, *Structure et magnétisme de systèmes mixtes 3d/4d et 3d/5d : une étude ab initio des alliages macroscopiques aux nanoparticules*, Ph.D. thesis, Université Paul Sabatier (Toulouse) (2004).
- [236] R. Hall, Journal of Applied Physics **30**, 816 (1959).
- [237] G. Andersson, T. Burkert, P. Warnicke, M. Björck, et al., Phys. Rev. Lett. **96**, 37205 (2006).
- [238] A. Winkelmann, M. Przybylski, F. Luo, Y. Shi, et al., Phys. Rev. Lett. **96**, 257205 (2006).
- [239] A. Dittschar, M. Zharnikov, W. Kuch, M.-T. Lin, et al., Phys. Rev. B **57**, R3209 (1998).
- [240] O. Kazakova, M. Hanson, P. Blomqvist, and R. Wäppling, Phys. Rev. B **69**, 94408 (2004).
- [241] Y. Lamy and B. Viala, J. Appl. Phys. **97**, 10F910 (2005).
- [242] V. A. Vas'ko, M. Kim, O. Mryasov, V. Sapozhnikov, et al., Appl. Phys. Lett. **89**, 092502 (2006).
- [243] J. Childress, J. Duvail, S. Jasmin, A. Barthélémy, et al., J. Appl. Phys. **75**, 6412 (1994).
- [244] P. F. Carcia, A. D. Meinhaldt, and A. Suna, Appl. Phys. Lett. **47**, 178 (1985).
- [245] P. Carcia, J. Appl. Phys. **63**, 5066 (1988).
- [246] S.-C. Shin and A. C. Palumbo, J. Appl. Phys. **67**, 317 (1990).
- [247] S. Hashimoto, Y. Ochiai, and K. Aso, J. Appl. Phys. **67**, 2136 (1990).
- [248] B. N. Engel, C. D. England, R. A. Van Leeuwen, M. H. Wiedmann, et al., Phys. Rev. Lett. **67**, 1910 (1991).
- [249] C. J. Lin, G. L. Gorman, C. H. Lee, R. F. C. Farrow, et al., J. Magn. Magn. Mater. **93**, 194 (1991).
- [250] B. Engel, M. Wiedmann, R. Van Leeuwen, and C. Falco, Physical Review B **48**, 9894 (1993).
- [251] R. Victora and J. MacLaren, Physical Review B **47**, 11583 (1993).
- [252] J. R. Barnes, S. J. O'Shea, M. E. Welland, J.-Y. Kim, et al., J. Appl. Phys. **76**, 2974 (1994).

BIBLIOGRAPHY

- [253] P. Beauvillain, A. Bounouh, C. Chappert, R. Mégy, et al., *Journal of Applied Physics* **76**, 6078 (1994).
- [254] D. Weller, Y. Wu, J. Stöhr, M. Samant, et al., *Phys. Rev. B* **49**, 12888 (1994).
- [255] S.-B. Choe and S.-C. Shin, *Phys. Rev. B* **57**, 1085 (1998).
- [256] G.-L. Chen, *J. Appl. Phys.* **87**, 6887 (2000).
- [257] S. Kim and J. Kortright, *Phys. Rev. Lett.* **86**, 1347 (2001).
- [258] S.-K. Kim and S.-C. Shin, *J. Appl. Phys.* **89**, 3055 (2001).
- [259] J. Dorantes-Dávila, H. Dreyssé, and G. M. Pastor, *Phys. Rev. Lett.* **91**, 197206 (2003).
- [260] G. Hu, T. Thomson, M. Albrecht, M. E. Best, et al., *J. Appl. Phys.* **95**, 7013 (2004).
- [261] W. Zeper, F. Greidanus, and P. Carcia, *IEEE Trans. Magn.* **25**, 3764 (1989).
- [262] C. H. Lee, R. F. C. Farrow, C. J. Lin, E. E. Marinero, et al., *J. Magn. Magn. Mater.* **93**, 592 (1991).
- [263] N. Nakajima, T. Koide, T. Shidara, H. Miyauchi, et al., *Physical Review Letters* **81**, 5229 (1998).
- [264] P. Ravindran, A. Kjekshus, H. Fjellvåg, P. James, et al., *Phys. Rev. B* **63**, 144409 (2001).
- [265] A. Barman, S. Wang, O. Hellwig, A. Berger, et al., *J. Appl. Phys.* **101**, 09D102 (pages 3) (2007).
- [266] S. Tsunashima, K. Nagase, K. Nakamura, and S. Uchiyama, *IEEE Trans. Magn.* **25**, 3761 (1989).
- [267] S.-K. Kim, V. A. Chernov, J. B. Kortright, and Y. M. Koo, *Appl. Phys. Lett.* **71**, 66 (1997).
- [268] E. Gan'shina, V. Guschin, I. Romanov, and A. Tselev, *J. Magn. Magn. Mater.* **185**, 258 (1998).
- [269] E. Gan'shina, V. Guschin, I. Romanov, A. Skobelev, et al., *J. Magn. Magn. Mater.* **193**, 174 (1999).
- [270] J.-R. Jeong, J. Kim, J.-W. Lee, S.-K. Kim, et al., *Appl. Phys. Lett.* **79**, 3296 (2001).
- [271] M. Przybylski, L. Yan, J. Ukrowski, M. Nyvlt, et al., *Phys. Rev. B* **73**, 085413 (2006).

- [272] M.-T. Lin, C. C. Kuo, H. Y. Her, Y. E. Wu, et al., *J. Vac. Sci. Technol., A* **17**, 3045 (1999).
- [273] C. Shern, *Surf. Sci.* **429**, L497 (1999).
- [274] U. Pustogowa, J. Zabloudil, C. Uiberacker, C. Blaas, et al., *Phys. Rev. B* **60**, 414 (1999).
- [275] J. Kim, J.-W. Lee, J.-R. Jeong, S.-C. Shin, et al., *Phys. Rev. B* **65**, 104428 (2002).
- [276] O. Robach, C. Quiros, P. Steadman, K. F. Peters, et al., *Phys. Rev. B* **71**, 099903(E) (2005).
- [277] F. Aguilera-Granja, A. Vega, J. Rogan, X. Andrade, et al., *Phys. Rev. B* **74**, 224405 (2006).
- [278] L. Favre, V. Dupuis, E. Bernstein, P. Mélinon, et al., *Phys. Rev. B* **74**, 14439 (2006).
- [279] R. Félix-Medina, J. Dorantes-Dávila, and G. Pastor, *Phys. Rev. B* **67**, 94430 (2003).
- [280] S. Baud, C. Ramseyer, G. Bihlmayer, and S. Blügel, *Phys. Rev. B* **73**, 104427 (2006).
- [281] C. Etz, J. Zabloudil, P. Weinberger, and E. Vedmedenko, *Phys. Rev. B* **77**, 184425 (2008).
- [282] R. Robles, J. Izquierdo, and A. Vega, *Phys. Rev. B* **61**, 6848 (2000).
- [283] P. Gambardella, S. Dhesi, S. Gardonio, C. Grazioli, et al., *Phys. Rev. Lett.* **88**, 47202 (2002).
- [284] H. Brune, *Creating Metal Nanostructures at Metal Surfaces Using Growth Kinetics*, in *Handbook of Surf. Sci.*, edited by E. Hasselbrink (Elsevier, Amsterdam, 2008), vol. 3 Dynamics, 761.
- [285] K. Kyuno, *Surf. Sci.* **397**, 191 (1998).
- [286] T. Michely, M. Hohage, M. Bott, and G. Comsa, *Phys. Rev. Lett.* **70**, 3943 (1993).
- [287] K. Bromann, H. Brune, H. Röder, and K. Kern, *Phys. Rev. Lett.* **75**, 677 (1995).
- [288] J. Rottler and P. Maass, *Phys. Rev. Lett.* **83**, 3490 (1999).
- [289] S. Heinrichs, J. Rottler, and P. Maass, *Phys. Rev. B* **62**, 8338 (2000).
- [290] L. Claude, *Construction d'un microscope à effet tunnel à basse température et études d'impuretés magnétiques en surfaces*, Ph.D. thesis, EPFL (2005).

BIBLIOGRAPHY

- [291] K. Kyuno and G. Ehrlich, Phys. Rev. Lett. **81**, 5592 (1998).
- [292] M. Hohage, M. Bott, M. Morgenstern, Z. Zhang, et al., Phys. Rev. Lett. **76**, 2366 (1996).
- [293] C. Antoniak, J. Lindner, M. Spasova, D. Sudfeld, et al., Phys. Rev. Lett. **97**, 117201 (2006).
- [294] A. Cebollada, D. Weller, J. Sticht, G. R. Harp, et al., Phys. Rev. B **50**, 3419 (1994).
- [295] H. J. Elmers, J. Hauschild, and U. Gradmann, J. Magn. Magn. Mater. **198-199**, 222 (1999).
- [296] W. Qi and M. Wang, J. Mater. Sci. Lett. **21**, 1743 (2002).
- [297] W. Qi, Solid State Commun. **137**, 536 (2006).
- [298] H. Ebert and R. Zeller, *The SPR-TB-KKR package*, <http://olymp.cup.uni-muenchen.de/ak/ebert/SPR-TB-KKR> (2005).
- [299] S. Bornemann, J. Minár, J. B. Staunton, J. Honolka, et al., Eur. Phys. J. D **45**, 529 (2007).
- [300] K. Bromann, H. Brune, M. Giovannini, and K. Kern, Surf. Sci. **388**, L1107 (1997).
- [301] M. Bode, O. Pietzsch, A. Kubetzka, and R. Wiesendanger, Phys. Rev. Lett. **92**, 067201 (2004).
- [302] W. Wernsdorfer, E. B. Orozco, K. Hasselbach, A. Benoit, et al., Phys. Rev. Lett. **78**, 1791 (1997).
- [303] H. B. Braun, Phys. Rev. B **50**, 16485 (1994).
- [304] W. Wernsdorfer, B. Doudin, D. Mailly, K. Hasselbach, et al., Phys. Rev. Lett. **77**, 1873 (1996).
- [305] G. Ehrlich and F. G. Hudda, J. Chem. Phys. **44**, 1039 (1966).
- [306] R. L. Schwoebel and E. J. Shipsey, J. Appl. Phys. **37**, 3682 (1966).
- [307] I. Markov, Phys. Rev. B **54**, 17930 (1996).
- [308] J. Amar, F. Family, and P. Lam, Physical Review B **50**, 8781 (1994).

Acknowledgments/Remerciements

La douce vie estudiantine prend fin avec ce manuscrit. C'est également quatre années d'effort de recherche qui s'achèvent avec lui. Tout ce travail n'aurait sans doute pas été réalisable sans la présence de nombreuses personnes à mes côtés. Je tiens maintenant à les remercier.

En tout premier lieu, mon directeur de thèse Prof. Harald Brune. Pour m'avoir accepté dans son groupe, pour les grandes compétences scientifiques dont il m'a fait profité et pour son écoute. Je suis particulièrement reconnaissant envers lui pour le temps qu'il a pu me consacrer personnellement durant la fin de ma thèse.

Je remercie très sincèrement les membres de mon jury pour le temps et l'énergie qu'ils ont consacré à la lecture de ce manuscrit ainsi que pour m'avoir jugé durant ma défense privée.

Je suis reconnaissant envers mes collaborateurs proches Stefano Rusponi et Safia Ouazi pour l'aide qu'ils m'ont apporté durant ma thèse, ainsi que pour m'avoir fait partagé leur méthode de travail.

La collaboration avec plusieurs groupes a été un élément déterminant pour la compréhension des phénomènes mis en jeu. Pour cela, je tiens à exprimer toute ma gratitude envers Sven Bornemann et toute son équipe de la Ludwig-Maximilians-University à Munich, ainsi que Julie Staunton de l'université de Warwick pour leur calculs ab-initio sur les propriétés magnétiques de nanostructures d'alliages bimétalliques. Je remercie également le groupe de théoriciens de l'Université de Vienne avec en tête Jan Zabloudil et Peter Weinberger pour leur calcul des propriétés magnétiques d'une surface d'alliage FeCo/Pt(111) dont je fais allusion dans le chapitre 4. J'en profite pour remercier Peter Bencok de l'ESRF pour ses conseils techniques et son calme olympien face aux problèmes durant la semaine d'expérience passée à Grenoble sur ce même sujet.

Pour leur énergie, leur efficacité, leur disponibilité et leur gentillesse, je remercie toute l'équipe technique et administrative de l'institut. Les parties de pétanque ou les soirées karting sont autant de souvenirs inoubliables de l'ambiance familiale qui régnait à l'institut.

Cette ambiance familiale n'aurait sans doute pas été la même sans la présence de nombreux couples formés ou venus pendant ma thèse. Je félicite au passage Uta Schlickum et Markus Etzkorn pour leur récent mariage et pour leur travail qui me

rappelle étrangement Pierre et Marie Curie dans le film "les palmes de monsieur Schultz", ainsi que Manuela Kobas pour son proche mariage et pour la qualité des relectures de mon manuscrit qui lui doit énormément.

J'ai passé également d'agréables moments sur la manip, au café, dans les couloirs ou au bureau avec les post-doc, doctorants et étudiants qui se sont succédés tout au long de ces quatre années. Pour en citer quelques uns, il y a par exemple les premiers, Sylvain Clair, Nicolas Weiss, Eric Delvigne, Pietro Gambardella... mais également les derniers, Marie Dufour, Fabian Natterer... et ceux que j'aurai toujours vu, Anne Lehnert, Régis Decker, Stéphane Pons...

Je ne voudrais pas oublier Stefan Fedrigo, qui partageait mon bureau. Nos discussions scientifiques comme politiques ou musicales auront toujours été une grande source de plaisir pour moi. Merci également pour tous tes conseils qui m'ont toujours été très utiles.

Ce passage sur les bords du Léman m'aura permis de rencontrer une multitude de personnes. Qu'ils soient italiens, allemands, espagnols, croates, bulgares, iraniens, portugais, français ou parfois même suisses, j'ai partagé avec eux d'excellents moments. Je garde des souvenirs de fêtes, de voyages, de discussions sur le vélo, de séances de squash, basket, badminton, escalade, course à pied, piscine.. Grâce à eux et à cette vie extra-institut, Lausanne gardera dans mon coeur une place toute particulière.

En particulier, il y a ceux qui sont devenus des amis proches Marta, Florian, Giulia, Pascal, Irene, Manuela. Vous allez encore entendre parler de moi un bon moment...

Il y a les amis de toujours ou en tous cas, ceux que je connais depuis l'école d'ingénieur à Paris. On a vécu pas mal de choses ensemble, on est presque tous docteurs, on suit la même histoire dans des pays différents. C'est vous plus que quiconque qui avait pu me comprendre pendant ces quatre années. Merci les gars, merci Julien, Yann, Cécile, Pierre-Yves, Thibault, Benoît, ... Au fait, j'espère que vous apprécierez que la dernière page avant la bibliographie soit le numéro de notre promotion.

Merci à ma famille également. Pour leur présence. Pour leur écoute. Pour leurs encouragements et pour réussir si bien à me changer les idées. Un grand merci. Promis, je ferai de mon mieux pour que vous compreniez mon sujet de thèse lors de la soutenance publique.

Et enfin, *obrigado Fátima, minha socióloga preferida por sempre ter me ouvido.*

Curriculum Vitae

Name : Géraud Moulas
Date of Birth : September 1, 1978
Nationality : French

Education :

December 2008 Ph.D. Thesis, EPFL, Lausanne

2004 - 2008 Research and teaching assistant at the Institute of Physics of Nanostructures of the Swiss Federal Institute of Technology in Lausanne, Switzerland

2002 - 2004 Master Degree in Solid States Physics and Condensed Matter at the Paris VI/XI University, France

1999 - 2004 Engineer Degree at the Ecole Supérieure de Physique et Chimie Industrielle, Paris, France

1996 - 1999 Preparation for competitive entrance examinations to scientific and engineering Grandes Ecoles at Lycée Saliège, Toulouse, France

1996 Scientific Baccalauréat

Schools :

July 2005 *"Self-Organized Nanostructures"*, Cargèse, France

February 2005 *36th Spring School, "Magnetism goes Nano"*, Jülich, Germany

Presentations/Conferences/Seminar :

- June 2007 *LNS Group Meeting*, Lausanne, Switzerland (oral)
- March 2007 *Colloque Louis Néel*, Lyon, France (poster)
- January 2007 *Surface Nanostructures SAOG-GSSI meeting*, Fribourg, Switzerland (oral)
- September 2006 *European Conference On Surface Science*, Paris, France (oral)
- November 2005 *Journée de la Recherche*, EPFL, Lausanne, Switzerland (poster)
- January 2005 *Surface Nanostructures SAOG-GSSI meeting*, Fribourg, Switzerland (poster)

Publications :**• High Magnetic Moments and Anisotropies for $\text{Fe}_x\text{Co}_{1-x}$ Monolayers on Pt(111)**

G. Moulas, A. Lehnert, S. Rusponi, J. Zabloudil, C. Etz, S. Ouazi, M. Etzkorn, P. Bencok, P. Gambardella, P. Weinberger, and H. Brune
accepted by Phys. Rev. B

• Interface and Alloy Contribution to the Magnetic Anisotropy in Bimetallic Nanoislands on Pt(111)

S. Ouazi, G. Moulas, S. Bornemann, J. Minár, H. Ebert, J. B. Staunton, K. Halleux, S. Rusponi, and H. Brune
to be submitted

• Opposite Magnetization Axis for Fe and Co Overlayers on Rh(111)

A. Lehnert, S. Rusponi, G. Moulas, M. Etzkorn, P. Gambardella, P. Bencok, and H. Brune
to be submitted